

**Consolidation during laser assisted fiber placement
Heating, compaction and cooling phases**

Çelik, O.

DOI

[10.4233/uuid:375598ed-f138-471c-9a1e-e28ee3820855](https://doi.org/10.4233/uuid:375598ed-f138-471c-9a1e-e28ee3820855)

Publication date

2021

Document Version

Final published version

Citation (APA)

Çelik, O. (2021). *Consolidation during laser assisted fiber placement: Heating, compaction and cooling phases*. [Dissertation (TU Delft), Delft University of Technology]. <https://doi.org/10.4233/uuid:375598ed-f138-471c-9a1e-e28ee3820855>

Important note

To cite this publication, please use the final published version (if applicable).
Please check the document version above.

Copyright

Other than for strictly personal use, it is not permitted to download, forward or distribute the text or part of it, without the consent of the author(s) and/or copyright holder(s), unless the work is under an open content license such as Creative Commons.

Takedown policy

Please contact us and provide details if you believe this document breaches copyrights.
We will remove access to the work immediately and investigate your claim.



CONSOLIDATION DURING LASER ASSISTED FIBER PLACEMENT

HEATING, COMPACTION AND COOLING PHASES

INVITATION

Consolidation During
Laser Assisted
Fiber Placement
*Heating, Compaction
and Cooling Phases*

Public presentation
6th December 2021
17:00

Public Ph.D. defence
6th December 2021
17:30

Address: Senate Hall,
TU Delft Aula
Conference Center,
Mekelweg 5, Delft

Propositions

accompanying the dissertation

CONSOLIDATION DURING LASER ASSISTED FIBER PLACEMENT HEATING, COMPACTION AND COOLING PHASES

by

Ozan Çelik

1. The correlation between the surface temperature and surface profile can be exploited to determine the degree of deconsolidation during the heating phase of laser-assisted fiber placement with a thermal camera. (This proposition pertains to Chapter 3 of this dissertation.)
2. The through-thickness temperature gradient in the incoming tape plays a significant role in effective intimate contact development since percolation flow is required to bring the resin material to the surface at locations with dry fibers. (This proposition pertains to Chapter 4 of this dissertation.)
3. The incoming tape can deform between the glass transition and melting temperature; however, this deformation is not sufficient to eliminate the effects of laser-induced deconsolidation. (This proposition pertains to Chapter 5 of this dissertation.)
4. During LAFP, compaction force is one of the factors that affect the temperature history. (This proposition pertains to Chapter 6 of this dissertation.)
5. When multiple supervisors with different opinions are involved in a PhD project, the ultimate key to success is efficient communication.
6. Living in a city outside of the Randstad area ensures that your friends visiting the Netherlands will skip spending time with you since it is far away from main tourist attractions.
7. People mostly focus on the start and end points in the life (also in a PhD project) but it is the journey in between which leads to actual understanding and growth.
8. Performing experiments in three different laboratories which are at least 100 km away from each other improves one's flexibility and planning skills significantly.
9. The coronavirus pandemic will cause deep cultural changes in the world.
10. During research, having an open mind set for collaboration opens the door to opportunities that would otherwise be inaccessible.

These propositions are regarded as opposable and defensible, and have been approved as such by the promoters Prof. C.A. Dransfeld and Dr. J.J.E. Teuwen.

Stellingen

behorende bij het proefschrift

CONSOLIDATION DURING LASER ASSISTED FIBER PLACEMENT HEATING, COMPACTION AND COOLING PHASES

door

Ozan Çelik

1. De correlatie tussen de oppervlaktetemperatuur en het oppervlakteprofiel kan worden benut om de mate van deconsolidatie te bepalen tijdens de verwarmingsfase van laser-ondersteunde vezelplaatsing door middel van een thermische camera. (Deze stelling heeft betrekking op hoofdstuk 3 van dit proefschrift.)
2. De temperatuurgradiënt door de dikte van de inkomende tape speelt een belangrijke rol bij de ontwikkeling van effectieve contactoppervlakte, aangezien percolatie vereist is om de hars naar de oppervlakte te brengen op locaties met droge vezels. (Deze stelling heeft betrekking op hoofdstuk 4 van dit proefschrift.)
3. De inkomende tape kan vervormen tussen de glas transitie temperatuur en de smelttemperatuur; deze vervorming is echter niet voldoende om de effecten van laser-geïnduceerde deconsolidatie te elimineren. (Deze stelling heeft betrekking op hoofdstuk 5 van dit proefschrift.)
4. Tijdens LAFP is de compactiekracht één van de factoren die de temperatuurgeschiedenis beïnvloeden. (Deze stelling heeft betrekking op hoofdstuk 6 van dit proefschrift.)
5. Wanneer meerdere begeleiders met verschillende meningen betrokken zijn bij een promotietraject, is efficiënte communicatie de ultieme sleutel tot succes.
6. Als men in een stad buiten de Randstad woont, zorgt dat ervoor dat vrienden die in Nederland op bezoek komen, geen tijd met u doorbrengen omdat het ver weg is van de belangrijkste toeristische attracties.
7. Mensen richten zich vooral op het begin- en eindpunt in het leven (ook in een PhD-project) maar het is de reis ertussen die leidt tot echte inzichten en groei.
8. Het uitvoeren van experimenteren in drie verschillende laboratoria die minstens 100 km van elkaar verwijderd zijn, verbetert iemands flexibiliteit en planningsvaardigheden aanzienlijk.
9. De pandemie van het coronavirus zal zware culturele veranderingen in de wereld veroorzaken.
10. Een open mindset voor samenwerking hebben tijdens onderzoek, opent de deur naar kansen die anders buiten bereik zouden zijn.

Deze stellingen worden oponeerbaar en verdedigbaar geacht en zijn als zodanig goedgekeurd door de promotoren Prof. C.A. Dransfeld en Dr. J.J.E. Teuwen.

CONSOLIDATION DURING LASER ASSISTED FIBER PLACEMENT

HEATING, COMPACTION AND COOLING PHASES

CONSOLIDATION DURING LASER ASSISTED FIBER PLACEMENT

HEATING, COMPACTION AND COOLING PHASES

DISSERTATION

for the purpose of obtaining the degree of doctor
at Delft University of Technology,
by the authority of the Rector Magnificus Prof.dr.ir. T.H.J.J. van der Hagen,
chair of the Board for Doctorates,
to be defended publicly on
Monday, 6 December 2021 at 17:30 hours

by

Ozan ÇELİK

Master of Science in Mechanical Engineering,
Middle East Technical University, Turkey
born in Ankara, Turkey.

This dissertation has been approved by the promotor.

Composition of the doctoral committee:

Rector Magnificus,
Prof. C.A. Dransfeld ,
Dr.ir. J.J.E. Teuwen,

Chairperson
Delft University of Technology, promotor
Delft University of Technology, copromotor

Independent members:

Prof.dr.ir. R. Akkerman,
Prof.dr. C. Binetruy,
Prof.dr.ir. L.J. Sluys,
Dipl.ing.dr.techn. R.M. Hinterhölzl,
Prof.dr.ir. R. Benedictus,

University of Twente
Centrale Nantes
Delft University of Technology
University of Applied Sciences Upper Austria
Delft University of Technology, reserve member

Other members:

Dr.ir. D.M.J. Peeters,

Delft University of Technology

This work is partially funded by European Regional Development Fund (ERDF) within the Smart Industry Fieldlab: ACM project under Grant No. KVV-00043.



Keywords: automated fiber placement, thermoplastic composites, consolidation, intimate contact development, laser deconsolidation

Printed by: Ipskamp Printing, the Netherlands

Front & Back: Cartoonized illustration of a laser-assisted fiber placement machine

Copyright © 2021 by O. Çelik

ISBN 978-94-6421-578-6

An electronic version of this dissertation is available at
<http://repository.tudelft.nl/>.

Contents

Summary	ix
Samenvatting	xi
Nomenclature	xv
1 Introduction	1
1.1 Background and Motivation	1
1.2 Objective, Approach and Outline	3
References	4
2 A Three-Dimensional Thermal Model for LAFP Process	7
2.1 Introduction	8
2.2 Thermal model for LAFP process	10
2.3 Optical model for LAFP process	12
2.4 Validation of the thermal model for LAFP	13
2.4.1 Materials and experimental setup	13
2.4.2 Specimen preparation and temperature measurement	13
2.4.3 Numerical model parameters	15
2.5 Results and discussion	16
2.6 Conclusion	20
2.A Appendix: Mesh and time step convergence of the thermal model	20
References	25
3 Deconsolidation of Thermoplastic Prepreg Tapes During Rapid Laser Heating	29
3.1 Introduction	30
3.2 Materials and Methods	32
3.2.1 Experimental Setup	32
3.2.2 Tape Deconsolidation Experiments	33
3.2.3 In-situ Measurements	34
3.2.4 Ex-situ Measurements	37
3.2.5 Analysis of Variance (ANOVA)	38

3.3	Results	39
3.3.1	Waviness at the nip point	39
3.3.2	Temperature history and out-of-plane deformation	39
3.3.3	Arc-length width at the nip point	43
3.3.4	Ex-situ measurements	43
3.4	Discussion	44
3.4.1	Deconsolidation mechanisms during rapid laser heating	44
3.4.2	Relevance to LAFP process.	49
3.5	Conclusion	51
	References	52
4	Intimate Contact Development During Laser Assisted Fiber Placement: Microstructure and Effect of Process Parameters	57
4.1	Introduction	58
4.2	Materials and Methods	61
4.2.1	Fiber Placement System	61
4.2.2	Specimens for Intimate Contact Investigation	61
4.2.3	Process Temperature Measurement	62
4.2.4	Pressure Measurement.	62
4.3	Effective Intimate Contact	63
4.3.1	Characterization	63
4.3.2	Analysis of Variance	64
4.3.3	Intimate Contact Calculation Based on Squeeze Flow Models	65
4.4	Results	68
4.4.1	Pressure Measurement.	68
4.4.2	Surface and Cross-Sectional Micrographs	68
4.4.3	Effects of Process Parameters on Intimate Contact Development	72
4.4.4	Temperature History and Intimate Contact Predictions	74
4.5	Discussion	75
4.6	Conclusion	78
	References	79
5	The Effect of Laser-Induced Deconsolidation on the Compaction Behavior of Thermoplastic Composite Tapes	85
5.1	Introduction	86
5.2	Materials and Experimental Methods	87
5.2.1	Materials.	87
5.2.2	Deconsolidation of As-received Tapes	88
5.2.3	Compaction of As-received and Deconsolidated Tapes	88
5.2.4	Degree of Effective Intimate Contact.	92
5.2.5	Cross-sectional Microscopy	92
5.2.6	Roughness and Waviness	92
5.3	Results	93
5.3.1	Effects of Laser-Deconsolidation on the Structure of the Tape before Compaction.	93
5.3.2	Compaction Behavior of the As-received and Deconsolidated Tapes.	95

5.4	Discussion	105
5.5	Conclusion	108
	References	108
6	The Influence of Inter-laminar Thermal Contact Resistance on the Cooling of Material during Laser Assisted Fiber Placement	111
6.1	Introduction	112
6.2	Materials and Experimental Methods	115
6.2.1	Fiber Placement System and Specimen Manufacturing	115
6.2.2	Process Temperature Measurement	116
6.2.3	Intimate Contact Measurement	117
6.2.4	Analysis of Variance (ANOVA)	118
6.3	Numerical Methods	118
6.3.1	Thermal Contact Resistance Calculation	119
6.3.2	Heat Transfer Model	120
6.4	Results	125
6.4.1	Experimental Process Temperature	125
6.4.2	Intimate Contact	126
6.4.3	Calculated Temperature History	128
6.5	Discussion	130
6.5.1	Effect of compaction force on cooling behavior	130
6.5.2	The role of TCR on temperature calculations.	131
6.5.3	Origins of TCR development during LAFP	133
6.5.4	Potential use of TCR for process inspection	134
6.6	Conclusion	134
	References	135
7	Concluding Remarks and Future Outlook	141
7.1	Summary and Conclusions	142
7.2	Recommendations for future research	144
	References	145
	Acknowledgments	147
	Curriculum Vitæ	151
	List of Publications	153

Summary

Thermoplastic composites (TPCs) are emerging in the aerospace industry owing to their advantages over thermoset counterparts such as infinite shelf life, high fracture toughness, chemical and solvent resistance, and recyclability. Also, they are suitable for fast, automated manufacturing since chemical reactions are not required to obtain the final mechanical properties and shape of the TPC structures. Laser-assisted fiber placement (LAFP) has become a promising manufacturing solution with a potential in reducing the material scrap rates and labor time per component, and increasing the repeatability. Moreover, thanks to the re-melting capability of TPCs, in-situ consolidated (without a post-consolidation step in an oven, press or autoclave) structures can be produced using the LAFP process, which can reduce the capital and energy costs associated with post-consolidation.

For the aerospace industry to widely accept and use LAFP with in-situ consolidation, sufficient part quality with a feasible processing speed must be achieved. One of the primary quality indicators is the consolidation quality, which can be quantified by the remaining voids within the composite laminate after manufacturing. Proper consolidation quality can only be obtained once the underlying mechanisms and the relation with the process parameters are understood. The main goal of this thesis is therefore to improve the understanding on the consolidation process during LAFP with in-situ consolidation.

LAFP with in-situ consolidation differs from conventional composite manufacturing methods such as autoclave processing or press molding in a number of ways such as localized rapid laser heating without pressure application, very short compaction times and cooling at ambient pressure. Due to these differences, compaction during LAFP cannot be completely described by existing theories, which were originally developed for conventional manufacturing techniques. Experimental and numerical studies were conducted to reveal the mechanisms of the consolidation process in all three phases of the LAFP (heating, compaction and cooling).

Firstly, a high-fidelity thermal model was developed for predicting the temperature history during LAFP. This was deemed valuable since consolidation mechanisms are strongly linked to the temperature history during the process. The thermal model was combined with an optical model from literature and fiber placement experiments were performed for validation. It was shown that the complete temperature history can be successfully predicted.

Then, the effect of rapid laser heating on the micro- and meso- structure of the ther-

moplastic tape was investigated. Thermoplastic tapes were heated above the melting temperature with different heated lengths and heating times in a dedicated experimental setup. The experiments resulted in significant changes in the tape structure, namely increased out-of-plane deformation, waviness, arc-length width, roughness, thickness and volumetric void content. This study showed for the first time that a unique deconsolidation behavior takes place during the heating phase of LAFP: the deconsolidation mechanisms are exacerbated by the non-uniform temperature at the tape surface, which is caused by roughness increase and waviness formation.

Next, intimate contact development under LAFP-specific thermal and mechanical boundary conditions/interactions and the effect of process parameters was studied. One-layer, unidirectional strips of CF/PEKK material were placed with different process parameters on a flat tool surface to create different intimate contact conditions. The concept of *effective intimate contact*, which is based on the resin content at the surface, was introduced and a methodology to measure it from surface micrographs was provided. Degree of effective intimate contact measured from the samples was compared with the existing intimate contact models using the temperature estimations from the thermal model and pressure measurements using a pressure sensitive film. It was shown that in addition to the squeeze flow mechanism, which is the base for the current intimate contact models, resin flow through the thickness of the tape and along the fiber direction at the surface need to be considered to explain effective intimate contact development.

Following the studies on the effects of laser-heating on the tape structure and intimate contact development during LAFP, the focus was placed on the effects of laser-induced deconsolidation on the compaction process of CF/PEEK tapes. First, tapes with different degrees of deconsolidation were manufactured with different laser settings. Then, as-received and laser-deconsolidated tapes were compacted under the same temperature histories and pressure levels. Waviness induced by laser-deconsolidation vanished when the material was heated up to the glass transition temperature even at a very low compaction pressure. However, all effects of laser-deconsolidation vanished only above the melting temperature and under sufficient pressure levels.

Finally, the effect of thermal contact resistance (TCR) correlated to the degree of intimate contact (DIC) between the incoming tape and the substrate on the temperature history was investigated experimentally and numerically. Experimental results indicated that, for the same tape temperature near the nip point, an increase in the compaction force resulted in a decrease in the temperature at the roller exit and the following cooling phase, in correlation with an increase in the final DIC. Also, the effect of the laser power on the final DIC was less pronounced than the compaction force. In the thermal model, when TCR at the tape-substrate interface was not considered, the temperature predictions underestimated the experimental measurements.

In conclusion, the thesis in hand pictures the consolidation mechanisms considering the unique aspects of LAFP. The findings can be used as a basis for creating more accurate process models and parameter optimization.

Samenvatting

Het gebruik van thermoplastische composieten (TPCs) is in opkomst in de luchtvaart- en ruimtevaartindustrie omwille van hun voordelen ten opzichte van de thermohardende tegenhangers, zoals oneindige houdbaarheid, hoge breuktaaiheid, goede chemische en oplosmiddel resistentie en recycleerbaarheid. Ook zijn ze geschikt voor snelle, geautomatiseerde productieprocessen omdat er geen chemische reacties nodig zijn tijdens het productieproces om de uiteindelijke mechanische eigenschappen en vorm van de TPC-structuren te verkrijgen. Een veelbelovend productieproces met TPCs is laser-ondersteunde vezelplaatsing (LAFP), dat de potentie heeft om de materiaalsnijresten en de werktijd per component te verminderen en de herhaalbaarheid van het proces/product te verbeteren. Door de hersmeltbaarheid van TPC kunnen daarboven, in-situ geconsolideerde constructies, i.e. zonder post-consolidatie stap in de oven, pers of autoclaaf, gemaakt worden door middel van LAFP. Dit kan de kapitaal- en energiekosten die geassocieerd worden met post-consolidatie sterk verminderen.

Om LAFP in combinatie met in-situ consolidatie op grote schaal te accepteren en te gebruiken, is er voor de luchtvaartindustrie, voldoende productkwaliteit in combinatie met realistische productiesnelheid nodig. Eén van de cruciale kwaliteitsindicatoren is de kwaliteit van consolidatie, die kan worden gekwantificeerd door het meten van de overgebleven leegtes in het composietlaminaat na het productieproces. Goede consolidatiekwaliteit kan alleen maar bereikt worden wanneer de onderliggende mechanismes en hun relatie met de verschillende procesparameters worden begrepen. Het hoofddoel van deze thesis is daarom om het inzicht in het consolidatieproces tijdens LAFP met in-situ consolidatie te verbeteren.

LAFP met in-situ consolidatie verschilt op een aantal manieren van de conventionele composiet productiemethodes zoals productie met de autoclaaf of vorming met de pers, zoals onder andere: gelokaliseerde snelle verwarming met een laser zonder toepassing van druk, zeer korte compacteertijden, en koeling bij omgevingsdruk. Door deze verschillen, is compactie tijdens LAFP niet volledig te beschrijven door de bestaande theorieën, die werden ontwikkeld voor de conventionele productiemethodes. Zowel experimentele als numerieke studies zijn uitgevoerd om de mechanismes van het consolidatieproces in alle drie de fases van het LAFP proces te onthullen (i.e. verwarmen, compacteren en koelen).

Ten eerste werd een hoog betrouwbaar thermisch model ontwikkeld voor het voorstellen van de temperatuurgeschiedenis tijdens LAFP. Dit werd als waardevol geacht omdat de consolidatiemechanismen sterk verbonden zijn met de temperatuurgeschie-

denis gedurende het proces. Dit thermische model werd gecombineerd met een optisch model uit de literatuur en vezelplaatsingsexperimenten werden uitgevoerd voor validatie. Er werd aangetoond dat de volledige temperatuurgeschiedenis met succes kan worden voorspeld.

Vervolgens werd het effect van snelle laserverwarming op de micro- en meso-structuur van de thermoplastische tape onderzocht. Thermoplastische tapes werden verwarmd boven hun smelttemperatuur waarin verschillende verwarmde lengtes en verwarmings tijden werden onderzocht in een speciaal hiervoor opgezet experiment. De experimenten toonden significante veranderingen in de structuur van de tape, namelijk grotere uit-het-vlak vervorming, meer golfing van de tape, toename in dikte en breedte (booglength) van de tape, meer ruwheid, en meer leegtes in de tape (op basis van volume). Voor het eerst werd aangetoond dat er uniek deconsolidatiegedrag plaats vindt tijdens de verwarmingsfase van LAFP: de mechanismen van deconsolidatie worden verergerd door de niet-uniforme temperatuur op het oppervlak van de tape, die wordt veroorzaakt door de toename van ruwheid en de vorming van golfingen.

Hierna werd de ontwikkeling van contactoppervlaktes onder LAFP-specifieke warmte en mechanische condities/interactie en het effect van relevante procesparameters onderzocht. Stroken van 1 unidirectionele laag koolstofvezel (CF)/PEKK materiaal werden geplaatst met verschillende procesparameters op een vlak oppervlak om verschillende omstandigheden voor vorming van contactoppervlakte te creëren. Het concept van effectieve contactoppervlakte werd geïntroduceerd, en is gebaseerd op de hoeveelheid hars aan de oppervlakte van de tape. Om dit te meten, werd een methode op basis van micrografie foto's van de oppervlakte van de tape bepaald. De gemeten mate van effectieve contactoppervlakte werd vergeleken met de bestaande contactoppervlakte modellen met behulp van temperatuurschattingen aan de hand van het thermische model en drukmetingen met drukgevoelige film. Er werd aangetoond dat naast het knijp-stromingsmechanisme, dat de basis vormt van de huidige contactoppervlaktemodellen, ook harsstroom door de dikte van de tape en in vezelrichting aan de oppervlakte moet worden meegenomen om effectieve contactoppervlakte ontwikkeling te verklaren.

Volgend op de onderzoeken naar de effecten van laser verwarming op de tape structuur en contactoppervlakte ontwikkeling tijdens LAFP, werd de focus geplaatst op het onderzoeken van de effecten van laser geïnduceerde deconsolidatie op het compactieproces van CF/PEEK tapes. Eerst werden tapes met verschillende gradaties van deconsolidatie gemaakt door het gebruik van verschillende laserinstellingen. Daarna werden gewone tapes (zoals ontvangen) en laser gedeconsolideerde tapes gecompacteerd onder dezelfde temperatuurs- en drukprofielen. De golfing veroorzaakt door laser deconsolidatie verdween wanneer het materiaal werd opgewarmd tot de glas transitie temperatuur, zelfs op lage compactiedrukken. Alle effecten van laser deconsolidatie verdwenen echter alleen boven de smelttemperatuur en onder voldoende compactiedruk.

Ten slotte, werd het effect van thermische contactweerstand (TCR), op de temperatuur geschiedenis zowel experimenteel als numeriek onderzocht. Deze TCR is gecorrigeerd aan de mate van contactoppervlakte (DIC) tussen de inkomende tape en het substraat. De experimentele resultaten gaven aan dat, voor dezelfde tape temperatuur nabij het raakvlak tussen de tape en de substraatlagen, een toename van de compactiekracht

resulteerde in een afname in de temperatuur op het punt nadat de compactierol voorbij gegaan is en de daaropvolgende afkoelfase. Dit hing ook samen met een toename in de mate van contactoppervlakte. Het effect van het laservermogen op de uiteindelijke mate van contactoppervlakte was minder uitgesproken dan het effect van de compactiekracht. In het thermische model onderschatten de temperatuur voorspellingen de experimentele metingen, wanneer TCR op het raakvlak van tape en substraat niet werd meegenomen.

Dit proefschrift geeft een beeld van de mechanismes van het consolidatieproces rekening houdend met de unieke aspecten van LAFP. De bevindingen kunnen worden gebruikt als basis voor het creëren van nauwkeurigere procesmodellen en parameteroptimalisatie.

Nomenclature

Abbreviations

AFP	Automated fiber placement
ANOVA	Analysis of variance
ASR	As-received
ATW	Automated tape winding
CAD	Computer aided design
CF/PEEK	Carbon fiber reinforced polyetheretherketone
CF/PEKK	Carbon fiber reinforced polyetherketoneketone
CF/PPS	Carbon fiber reinforced polyphenylene sulfide
CFRP	Carbon fiber reinforced polymer
CTE	Coefficient of thermal expansion
CTIC	Calculated temperature with imperfect contact
CTPC	Calculated temperature with perfect contact
DEIC	Degree of effective intimate contact
DIC	Degree of intimate contact
FD	Finite difference
FEM	Finite element method
HLD	Highly laser-deconsolidated
LAFP	Laser-assisted fiber placement
LLS	Laser line scanner
LWIR	Long-wave infrared
OP	Out of plane
PE	Polyethylene
PGD	Proper generalized decomposition
PEEK	Polyetheretherketone
PEKK	Polyetherketoneketone
POM	Polyoxymethylene
PP	Polypropylene
PVF	Poly(vinylidene fluoride)
RMS	Root mean square
PTFE	Polytetrafluoroethylene
SLD	Slightly laser-deconsolidated

TCR	Thermal contact resistance
TPC	Thermoplastic composite
VCSEL	Vertical cavity surface emitting laser

Roman symbols

A	Amplitude
a_0	Initial surface asperity height
b_0	Initial surface asperity width
C	Thermal contact conductance
C_p	Specific heat
D_{ic}	Degree of intimate contact
F	Compaction force
h	Convection coefficient
h_a	Convection coefficient between the composite and the air
h_l	Laser spot height
h_r	Convection coefficient between the composite and the roller
I	Roller indentation
k	Thermal conductivity
L	Length
p	Pressure
p_0	Initial pressure
p_g	Void pressure
q	Heat flux
R	Thermal contact resistance
R_r	Roller radius
t	Time
t	Thickness
T	Temperature
T_0	Initial temperature
T_a	Air temperature
T_{amb}	Ambient temperature
T_c	Reversible crystallization temperature
T_g	Glass transition temperature
T_m	Melting temperature
T_{np}	Nip point temperature
$T_{substrate}$	Substrate temperature
T_{tape}	Tape temperature
T_{tool}	Tool temperature
V	Volume
V, v	Placement speed
V_g	Void volume
w_0	Initial width of the gap between two surface asperities
w_l	Laser spot width
w_r	Roller width
w_s	Substrate width

w_t	Tape width
x_{nip}	x-coordinate of the moving nip point
$\mathbf{x}, \mathbf{y}, \mathbf{z}$	Cartesian coordinates

Greek symbols

α_l	Laser angle
α_t	Tape feed angle
λ	Wavelength
$\lambda_c, \lambda_f, \lambda_s$	Cut-off wavelengths to filter surface profiles
λ_{CFRP}	Through-thickness thermal conductivity of the composite
λ_{air}	Thermal conductivity of the air
ρ	Density

Chapter 1

Introduction

1.1 Background and Motivation

Climate action failure and infectious diseases are amongst the risks which will have the most severe global impact in the next ten years [1], with some consequences for the aerospace industry. To avoid the destructive consequences of the climate change, global carbon dioxide (CO₂) emissions need to decline rapidly, by 7.6 % each year, between 2020 and 2030 [2]. This requirement is translated to the aerospace industry in the form of a carbon-neutral growth starting 2020 and a 50 % overall CO₂ emission reduction by 2050 [3]. Manufacturing lighter aircraft is one of the primary goals to reduce the CO₂ footprint. New design concepts, innovative materials and accompanying manufacturing methods need to be developed to achieve this goal. Additionally, the Coronavirus disease 2019 (COVID-19) outbreak impacted the aerospace industry significantly. Because of the restrictions imposed by the governments in an attempt to restrict the spread of the virus, labor intensive jobs almost came to a halt. Aerospace industry still relies on many manually manufactured components due to comparatively low volume production and high customization. This makes the aerospace industry heavily vulnerable to the impacts caused by such restrictions.

Besides the consequences of environmental risks, current production rates of lightweight composite structures are far from meeting the demands of the commercial aerospace industry. For example, the delivery capacity of Airbus was 863 aircraft for the year 2019 [4] whereas the forecasts show that around 1900 aircraft per year will be demanded from the company over the next twenty years [5]. Even though COVID-19 affects the international transportation drastically for now, the previous experience with the SARS outbreak in 2003 shows that such effects are short-termed and followed by a rebound which brings the air traffic back to its long-term increasing trend [5]. Increasing global population and urbanization indicate that the demand for accessible and environment-friendly transportation systems will continue to grow [6].

The aforementioned reasons justify using automated composite manufacturing methods for aerospace structures. Composite materials provide a solution to the weight reduction problem owing to their high specific strength. In fact, thermoset composites

are in significant use in commercial aircraft such as Airbus A350 and Boeing 787. Thermoplastic composites (TPC) have recently drawn significant interest in the aerospace industry for their infinite shelf life, high fracture toughness, chemical and solvent resistance, weldability and recyclability. Also, chemical reactions are not needed to obtain the final mechanical properties and shape of the TPCs. This enables the development of fast and robust automated manufacturing methods which would aid in mass adoption of TPCs in the industry.

One of the promising production methods for typical aerospace components in an automated fashion is laser-assisted fiber placement (LAFP). With LAFP, in-situ consolidation (without a post-consolidation step in an autoclave, oven or press) is achievable when thermoplastic prepregs are used. This provides potential reduction in cycle time, energy consumption and cost. In addition to these benefits, optimized structures can be manufactured by steering fibers and material waste can be reduced by producing near net shape components. In modern LAFP systems, a laminate is built by heating the surface of the tape and substrate with a laser heat source pointed towards the nip point and compacting with a roller as shown in Figure 1.1.

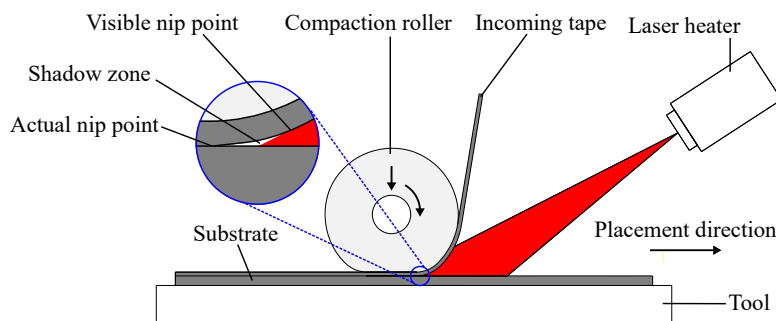


Figure 1.1. Working principle of a typical LAFP system.

For LAFP with in-situ consolidation to be widely accepted and used by the industry, sufficient part quality with a feasible processing speed must be achieved. One of the primary quality indicators is the consolidation quality, which can be quantified as the remaining voids within the composite laminate after manufacturing. The importance of the consolidation quality comes from the fact that it impacts the mechanical properties significantly [7]. A laminate with proper consolidation quality can only be manufactured once the underlying mechanisms and the relation with the process parameters are understood. To reach this goal, many researchers have used approaches which were originally developed for conventional composite manufacturing methods such as press molding or autoclave consolidation.

Due to the fast nature of the process and complex, interconnected phenomena taking place simultaneously, LAFP requires specific attention in terms of explaining how consolidation is achieved throughout the process. The process has three distinctive phases with different characteristics, namely the heating, compaction and cooling phases. All of these phases have a link to (either affect or is affected by) the consolidation quality of the part. In the heating phase, the material is heated to high processing tem-

peratures (400-500 °C) without pressure application. Following the rapid heating, a very short compaction time (usually between 0.01 and 0.3 s depending on the deformation of the compaction roller and the placement speed) is available to consolidate the tape and substrate during the compaction phase. Finally, in the cooling phase, the laminate temperature decreases due to the ambient conditions, again without applied pressure. Such features are not commonly observed in other type of manufacturing methods. Our knowledge about which consolidation mechanisms play a role during all of these phases is limited because it requires innovative experimental methods which provide sufficient accuracy under such extreme conditions. Once the consolidation mechanisms are revealed, predictive models can be established to optimize the process and use its full capabilities.

1.2 Objective, Approach and Outline

The thesis in hand deals with understanding the consolidation mechanisms under LAFP-specific thermal/mechanical boundary conditions/interactions. Experiments and numerical methods were employed to understand the physics of all three phases of the process: heating, compaction and cooling. The outline of the thesis is planned as a series of investigations following the sequential order in the actual LAFP process, which is schematically described in Figure 1.2. In this figure, the phases of the process which are relevant to each chapter are demonstrated.

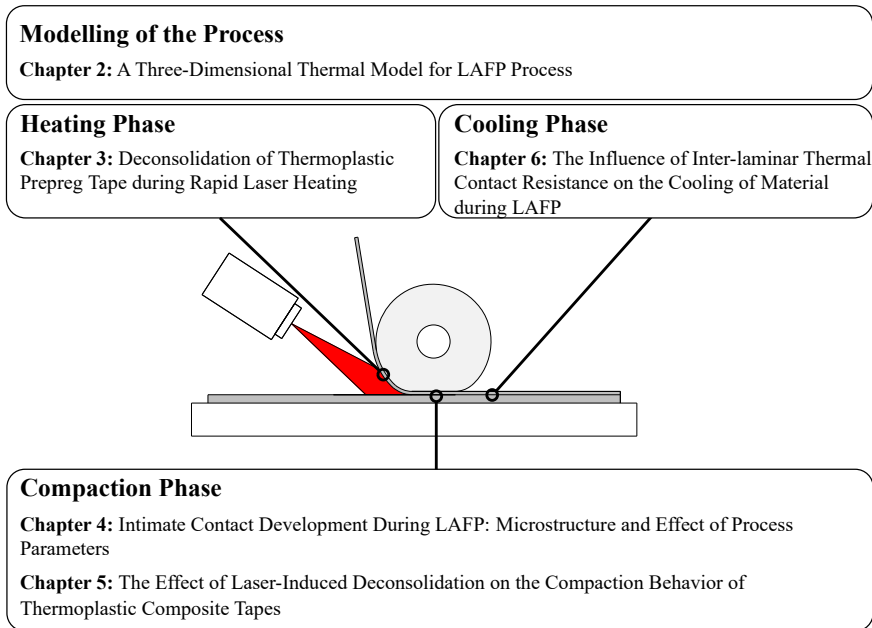


Figure 1.2. Schematic description of the outline of this thesis.

In Chapter 2, a three-dimensional thermal model of the LAFP process was developed. Such a model is a prerequisite for numerical analysis of the consolidation mechanisms.

In Chapter 3, the effect of rapid heating without pressure application on the deconsolidation behavior of thermoplastic prepreg tape was experimentally studied. A novel experimental setup was developed to replicate the heating phase of the LAFP process that allows to monitor the process conditions and measure the material response in-situ. The effects of heated spot length and heating time, controlled using a vertical cavity surface emitting laser (VCSEL) heater, on different deconsolidation mechanisms were discussed.

In Chapter 4, intimate contact development during LAFP and the effect of process parameters were investigated. A novel concept, effective intimate contact, was introduced to quantify the intimate contact in non-homogeneous surfaces and a methodology to measure it from surface micrographs is provided. Measurements made with this new concept were compared with existing intimate contact models. The shortages of the current models were highlighted and a new approach to describe intimate contact development during LAFP was proposed.

Following the previous chapters, Chapter 5 presents a deeper investigation on the effect of deconsolidation on intimate contact development. As-received prepreg tapes and tapes deconsolidated with the laser heater presented in Chapter 3 were compacted under the same temperature and pressure history. The comparison of the compaction behavior of each prepreg type revealed the influence of deconsolidation.

In Chapter 6, the influence of the consolidation quality on the thermal history during the LAFP process was investigated. Laminates with different degrees of intimate contact were manufactured by changing only the compaction force and keeping all other parameters, such as the laser power/angle and placement speed constant. During placement, the temperature at the outlet of the compaction roller was measured with an infrared camera which was mounted to the rear side of the placement head. The degree of intimate contact was determined by using cross-sectional microscopic images. The temperature distribution at the roller exit and the measured degree of intimate contact were compared to demonstrate the effect of consolidation quality on the temperature history.

In Chapter 7, the results in the previous chapters were summarized and combined to provide the reader a broader perspective. Potential implications for the state-of-the-art LAFP systems were explained. Future directions for research were recommended.

The chapters of this dissertation were reproduced from research articles with minimal change in the content. The author believes that such a format would increase the self-integrity of the chapters and allow the reader to study them separately.

References

- [1] World Economic Forum, . The Global Risks Report. Tech. Rep.; 2020.
- [2] United Nations Environment Programme, . Emissions Gap Report 2019. Tech. Rep.; 2019.
- [3] European Commission, . Flightpath 2050 Europe's Vision for Aviation. Tech. Rep.; 2011.

- [4] Airbus, . Press Release. 2020.
- [5] Airbus, . Global Market Forecast: Cities, Airports & Aircraft 2019-2038. 2019.
- [6] World Economic Forum, . The Global Risks Report 2017 12th Edition Summary for Policymakers. 2017. ISBN 978-1-944835-07-1. arXiv:arXiv:1011.1669v3.
- [7] Mehdikhani, M., Gorbatikh, L., Verpoest, I., Lomov, S.V.. Voids in fiber-reinforced polymer composites: A review on their formation, characteristics, and effects on mechanical performance. *Journal of Composite Materials* 2019;53(12):1579–1669.

Chapter 2

A Three-Dimensional Thermal Model for LAFP Process

Consolidation mechanisms are strongly linked to the temperature history during laser-assisted fiber placement (LAFP) process. Because of that, analysis of the temperature history is helpful for understanding these mechanisms. In this chapter, a high-fidelity thermal model was developed for predicting the temperature history during LAFP. For validation, fiber placement experiments were performed. The temperature history was measured using thermocouples and a thermal camera. The thermal model was combined with an optical model from literature and it was shown that the complete temperature history can be successfully predicted.

Dr. S.M.A. Hosseini contributed significantly to the optical model and validation experiments presented in this chapter.

2.1 Introduction

Temperature history affects a number of phenomena during LAFP, including intimate contact development, healing, crystallization, void compaction/growth and residual stress development. As a result, it has a direct impact on the mechanical properties of the final structure. This makes the analysis of the temperature history instrumental for understanding the physical mechanisms during the process, predicting the resulting part quality and optimizing the LAFP process.

Modelling of thermal phenomena during automated fiber placement (AFP) and automated tape winding (ATW) has been a focal point for research since the late 1980s. The works of Beyeler and Guceri [1] and Grove [2] can be mentioned among the earliest research in this field. These two models set an example for many succeeding researchers on how to conceptualize the problem domain (e.g. the bodies of tape and substrate before and after the nip point) and link the process parameters to temperature history via showing the effects of the laser power and placement speed. In the following years, many models with different dimensionality (one-, two- or three- dimensional (1D, 2D, 3D)), frames of reference (Eulerian or Lagrangian) and solution methods (finite difference (FD), finite element method (FEM), etc.) were proposed. For an extensive bibliography on thermal modelling, the reader can refer to the review articles of Orth et al. [3], Yassin and Hojjati [4] and Martin et al. [5].

In Table 2.1, a summary of the existing models is shown with an emphasis on recent publications, some of which were not covered by the aforementioned review articles. Three main trends have driven the development of different types of models: increasing the accuracy of the temperature predictions, the ability to calculate the temperature on-line during the process and analyze the temperature history for fiber placement on more complex, curved surfaces. As a result of the first trend, 3D models, which are more demanding due to the increased degrees of freedom, were developed by several researchers to describe the tape and substrate [6–10] whereas early models used various simplifying assumptions to reduce the representation of the tape and substrate to a 1D or 2D domain. The second trend led to analytical [11], surrogate [12] or semi-analytical models [13]. Also, solving procedures such as proper generalized decomposition (PGD) [8] or collocation [14] techniques were implemented. Following the third trend, researchers adapted the thermal models to curved molds or helical winding by incorporating the substrate geometry [15–17]. These studies focused on the effect of optical interactions between the laser and the composite at the nip point for curved substrates.

Since the main aim of this thesis is to understand the consolidation mechanisms and use the temperature history to obtain a deeper understanding of the process, the focus was not placed on the requirement of fast calculations or the complexities of curved substrates. Instead, a high-fidelity thermal model for the analysis of LAFP on flat surfaces was developed. To increase the accuracy of the model, both the tape and the substrate were modelled in 3D. The capability of simulating sequential placement of tapes was added to show that the model can predict not only the temperatures at the surface, but also within the substrate. For validation, the model was combined with an optical model from the literature [25] and compared with temperature measurements from LAFP experiments.

Table 2.1. Overview of the thermal models for automated fiber placement (AFP) and automated tape winding (ATW) in literature. (N/A: Not specified)

Source	Year	Process	Frame of reference	Dimensions	Method	Experimental Validation
Beyeler and Guceri [1]	1988	Flat AFP	Eulerian	2D	FD	No
Grove [2]	1988	Flat AFP	Eulerian	2D	FEM	No
Agarwal et al. [18]	1992	Hoop ATW	Eulerian	2D	FD	Thermocouple
Mantell and Springer [19]	1992	Flat AFP/ATW	Lagrangian	2D	FEM	Thermocouple [20]
Toso et al. [6]	2004	Hoop ATW	Lagrangian	3D	FEM	Pyrometer
Hassan et al.[7]	2005	Hoop ATW	Lagrangian	3D	FEM	Thermocouple
Grouve [14]	2012	Flat AFP	Lagrangian	1D	Collocation	Infrared camera
Chinesta et al. [8]	2014	Flat AFP	Eulerian	3D	PGD	No
Stokes-Griffin et al. [21]	2015	Flat AFP	Eulerian	2D	FEM	Thermocouple
Lichtinger et al. [9]	2015	Flat AFP	Lagrangian	1D, 3D	FD, FEM	Infrared camera/Thermocouple
Jeyakodi [10]	2016	Flat AFP	Lagrangian	3D	FEM	No
Schaefer et al. [12]	2017	Flat AFP	N/A	2D	FVM	Infrared camera/Thermocouple
Di Francesco et al. [13]	2017	Flat AFP	N/A	1D	Semi-analytical	Infrared camera
Weiler et al. [11]	2018	Hoop ATW	N/A	1D	Analytical	No
Kok [22]	2018	Flat AFP	Eulerian	1D	FD	Thermocouple
Aghababaei et al. [23]	2019	Flat AFP	Lagrangian	2D	FD	Thermocouple
Kollmannsberger [15]	2019	Curved AFP	N/A	2D	FD	Infrared camera
Zaami et al. [16]	2020	Helical ATW	N/A	3D (substrate)/2D (tape)	FD	Infrared camera [24]
Hosseini et al. [17]	2020	Helical ATW	Lagrangian (substrate)/Eulerian (tape)	1D (substrate)/2D (tape)	FD	Infrared camera

2.2 Thermal model for LAFP process

A three dimensional Lagrangian finite element (FE) model of the tape and substrate with a moving placement head configuration was used to estimate the transient temperature distribution during the LAFP process. Abaqus 2017 finite element package was used to create and solve the model. The incoming tape and substrate were modeled as two stationary bodies in a Lagrangian reference frame. A moving placement head configuration was implemented, i.e. the laser illuminated area and the area where the convection coefficient was applied due to the compaction roller moved according to the placement speed.

The energy equation was solved to find the transient temperature distribution $T(t)$ within the incoming tape and substrate:

$$\rho C_p \frac{\partial T}{\partial t} = \nabla(k \nabla T) \quad (2.1)$$

where ρ is the density, C_p is the specific heat and k is the anisotropic thermal conductivity of the material. Radiative heat transfer, the latent heat of fusion of the polymer and heat generation due to crystallization were neglected as their effects are weaker than the other methods of heat transfer [11].

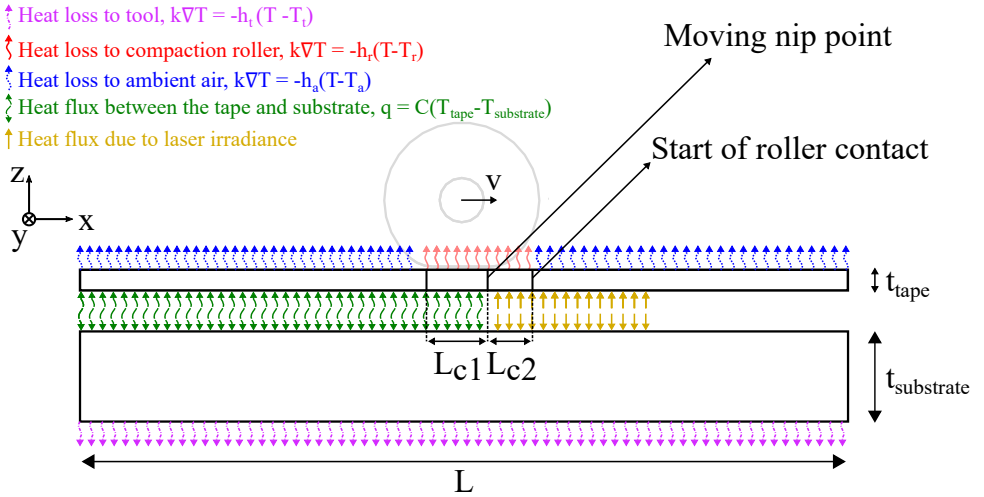


Figure 2.1. Modeling space and moving boundary conditions of the finite element model. The description is shown in 2-D for simplicity; however, the model domain expands in y-direction and the boundary conditions are applied along the whole tape width.

Referring to Figure 2.1, the following boundary conditions were applied to the model: The laser irradiance, compaction roller and the nip point moved in the placement direction with the placement speed v and the x-coordinate of the moving nip point is described with $x_{\text{nip}} = vt$, where t is the time. The nodes at the bottom surface of the tape

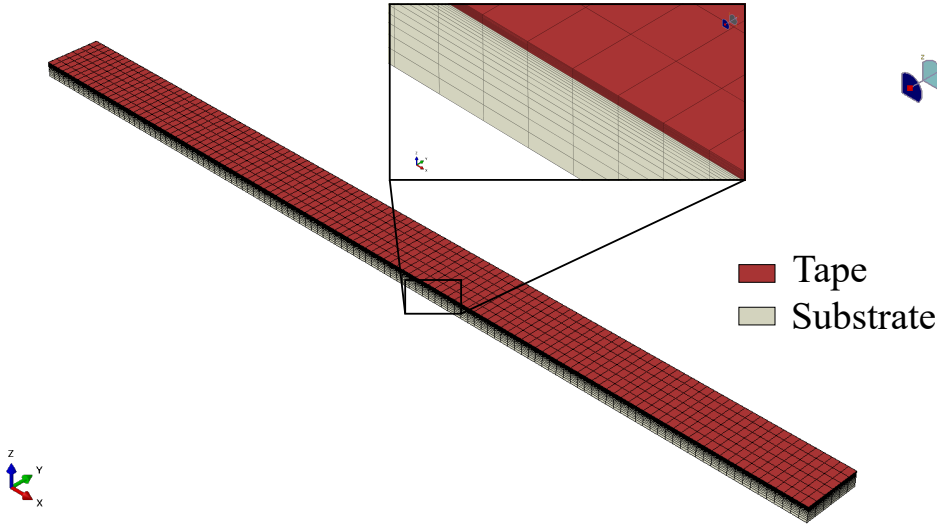


Figure 2.2. The model with the converged mesh for the tape and substrate.

and the top surface of the substrate with an x -coordinate larger than x_{nip} were heated with the laser irradiance distribution obtained from the optical model (yellow arrows), which will be further detailed in Section 2.3. Just prior to the nip point and during the compaction process ($x > x_{nip} - L_{c1}$ and $x < x_{nip} + L_{c2}$ in Figure 2.1, respectively), the top surface of the tape cooled down due to the contact with the compaction roller (red arrows). Before and after the contact with the roller ($x > x_{nip} + L_{c2}$ and $x < x_{nip} - L_{c1}$), the ambient air cooled down the top surface of the tape (blue arrows). The heat loss to the compaction roller and the ambient air were formulated as a moving convection boundary condition:

$$k\nabla T = -h(T - T_{amb}) \quad (2.2)$$

where h is the convection coefficient (h_r , h_a and h_t for the roller, air and tool convection coefficients, respectively), T is the temperature at the composite node and T_{amb} is the ambient temperature at the corresponding boundary (T_r , T_a and T_t for the roller, air and tool temperatures, respectively). Equation (2.2) was also used to express the heat loss at the bottom surface of the substrate due to the contact (magenta arrows) with the tool in a static manner.

At the tape-substrate interface, the heat transfer was modeled with a thermal contact [26]:

$$q = C(T_{tape} - T_{substrate}) \quad (2.3)$$

where q is the heat flux between the tape and the substrate and C is the thermal contact conductance. The value of C was updated based on the location of the moving nip point. At the regions in front of the nip point, no heat transfer was possible between the tape and the substrate. To impose this condition without creating numerical problems, the thermal contact conductance was set to a very low value, namely $10^{-5} \text{ W/m}^2\text{K}$. Past the

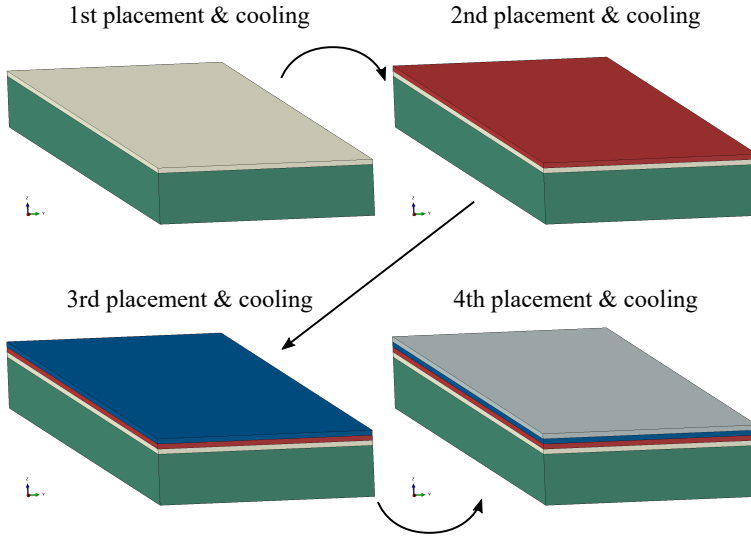


Figure 2.3. Demonstration of the model update for the placement of four tapes on the substrate.

nip point, the thermal contact conductance was set to $10^6 \text{ W/m}^2\text{K}$ representing a perfect thermal contact at the interface between the tape and substrate.

The model is capable of simulating sequential placement of tapes. To do that, first, a placement and a cooling step was defined for each new layer. After a specific layer is placed and cooled for the defined cooling time, a new layer is activated on top of the previous one using the "Model change" interaction. This procedure is demonstrated for the placement of four layers on a substrate in Figure 2.3.

DC3D8 linear hexahedral heat transfer elements were used to mesh the tape and the substrate. The mesh and time step convergence of the model was studied as explained in Section 2.A. The resulting model with the converged mesh configuration is shown in Figure 2.2. The coordinates of the laser irradiation, area with heat loss to the compaction roller and thermal contact conductance at each time step were updated with the user subroutines DFLUX, FILM and GAPCON, respectively.

2.3 Optical model for LAFP process

During LAFP, the complex interaction between the laser beams and the composite material necessitates the implementation of an optical model to calculate a realistic heat input for the thermal model. It has previously been shown that CFRP tapes show a non-specular optical behavior when illuminated with a laser heater [14, 27]. To account for this behavior, the ray-tracing model proposed in [25] was used to determine the laser intensity on the tape and substrate surfaces.

The model employs two optical models at different scales, namely the macro- and micro- models. The macro- model initiates collimated laser beams from the laser source

towards the nip point and calculates which surfaces are hit by the initial and reflected laser beams. The reflection of the laser beams at the anisotropic tape and substrate surfaces is calculated by the micro-model and communicated with the macro-model. Both models work iteratively to calculate the heat flux on the tape and substrate surfaces after three reflections. For the details of the optical model, the reader is referred to [28].

The optical model requires several geometric parameters for the laser source, incoming tape, substrate and compaction roller as an input, which are shown in Figure 2.4 and explained in Table 2.2. These parameters were determined from on-site measurements and Computer Aided Design (CAD) drawings of the placement head.

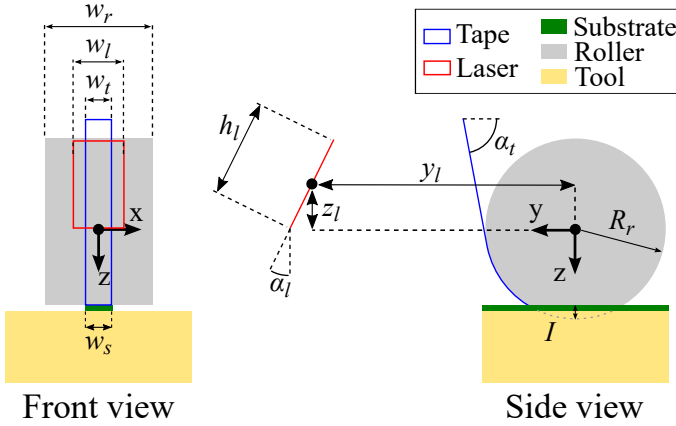


Figure 2.4. Geometrical representation of the LAFP system.

2.4 Validation of the thermal model for LAFP

2.4.1 Materials and experimental setup

Validation experiments were performed at the LAFP facility in Thermoplastic Research Center (TPRC), the Netherlands. The facility comprised a Coriolis Composites AFP robot with six degrees of freedom. The robot was equipped with a 1 kW diode laser operating at a wavelength of 980 nm. A polytetrafluoroethylene (PTFE) compaction roller with a 35 mm radius, 50 mm width and 40-shore hardness was installed. The system is demonstrated in Figure 2.5. Toray Cetex TC1200 carbon fiber reinforced polyetheretherketone (CF/PEEK) tapes with a fiber volume fraction of 59 % were used. The width and thickness of the tapes were 6.35 mm and 0.15 mm, respectively.

2.4.2 Specimen preparation and temperature measurement

The objective of the experimental campaign was to validate the full temperature history obtained by the combined optical-thermal model. The experimental procedure for temperature measurement is visually summarized in Figure 2.6. First, a 300 mm-long,

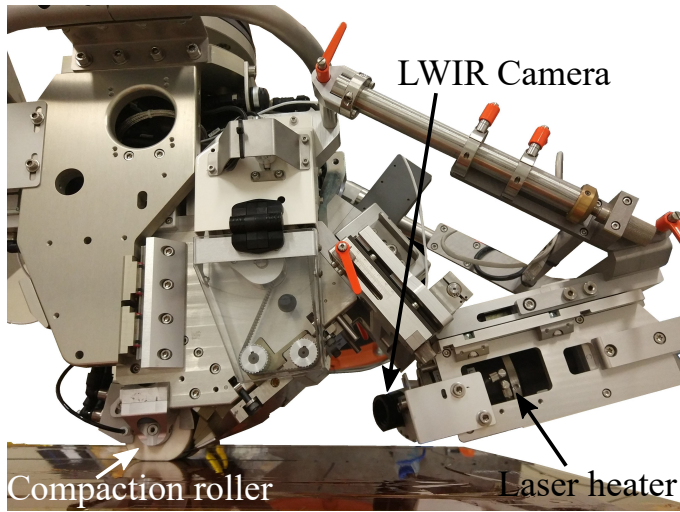


Figure 2.5. The LAFP system used for the validation of the thermal model.

6.35 mm-wide $[0]_{10}$ substrate was placed on a steel tool covered with polyimide film. The laser power was set to 400 W for the first layer, and 450 W for the subsequent layers. The compaction force and the placement speed were set to 500 N and 100 mm/s, respectively. These parameters were determined based on previous experience so that the substrates have low inter-laminar void content. Then, a 100 μm -thick K-type thermocouple was spot-welded on the top surface of the substrate and connected to a data acquisition system to record the temperature with 600 Hz. The thermocouple was positioned roughly at 150 mm from the beginning edge of the substrate in the fiber direction so that the transient effect of the start of the placement was minimized. Finally, five more $[0]$ layers were placed while the thermocouples were recording the temperature. Before each subsequent layer was placed, the laminate was let to cool down to room temperature based on thermocouple readings. Seven different samples were made with this procedure, which resulted in seven measurements of the complete temperature history on the top surface of the 10th layer during the placement of the top 5 layers of a 15-layer laminate.

In addition to the thermocouple measurements, the temperature of the region surrounding the nip point was recorded with a Micro-Epsilon thermalIMAGER TIM 400 long-wave infrared (LWIR) camera, which operates at a spectral range of 7.5–13 μm . The camera provided continuous images at 80 Hz with a resolution of 382×288 pixels. Multiple measurement boxes were placed in the thermal images to determine the temperature on the tape, substrate and nip point as demonstrated in Figure 2.7. Since it is very difficult to determine the actual relative position between the nip point and the measurement boxes on the tape due to the complex geometry of the deformed roller, only the substrate temperature was measured. The distance between the nip point and the measurement boxes on the substrate were determined using the appearance of the thermocouple in the thermal images. First, the frames at which the thermocouple passed

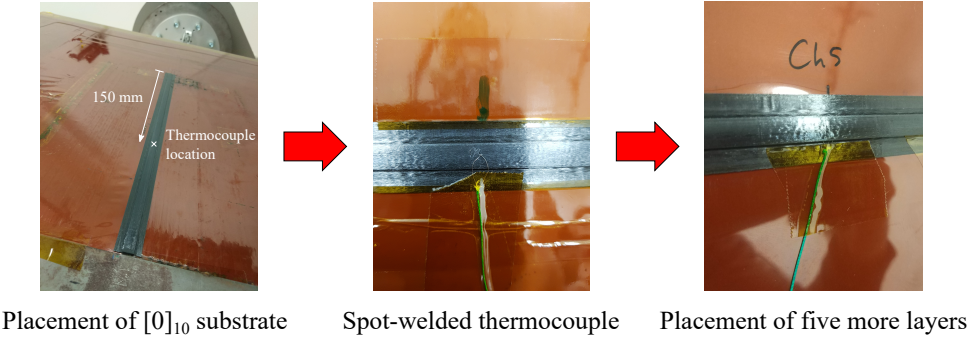


Figure 2.6. Temperature measurement procedure with thermocouples.

each measurement box on the substrate and the nip point were determined. Then, using the frame rate of the camera, the time required for the thermocouple to pass from one measurement box to the other was calculated. Finally, the duration was multiplied with the placement speed to find the distance between each box. Temperature at six different locations on the substrate including the nip point were reported. Thermal images from four placement experiments were available.

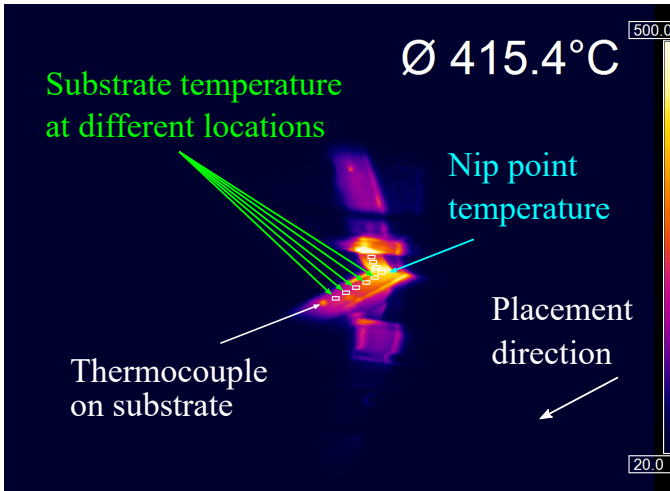


Figure 2.7. A snapshot of the continuous thermal images obtained with the infrared camera demonstrating the temperature measurement boxes at different locations of the substrate and the nip point.

2.4.3 Numerical model parameters

As an input to the optical model, the position and orientation of the laser with respect to the center of the compaction roller are schematically described in Figure 2.4 and the

geometrical values are given in Table 2.2. The values for the thermal model parameters, whose descriptions are shown in Figure 2.1, are summarized in Table 2.3. The thermal material properties provided in Table 2.4 were used for the composite material.

Table 2.2. Geometrical parameters for the optical model.

Parameter	Description	Value
w_r	Roller width	50 mm
R_r	Roller radius	35 mm
I	Roller indentation	1.5 mm
w_l	Laser spot width	11 mm
h_l	Laser spot height	16 mm
y_l	Laser y-position relative to the roller center	507 mm
z_l	Laser z-position relative to the roller center	91 mm
α_l	Laser angle	14.7°
w_t	Tape width	6.35 mm
α_t	Tape feed angle	45°
w_s	Substrate width	6.35 mm

Table 2.3. The parameters used in the heat transfer model

Parameter	Symbol	Value	Unit
Placement speed	v	100	mm/s
Roller contact length in the compaction zone	L_{c1}	20	mm
Roller contact length prior to the nip point	L_{c2}	17	mm
Domain length	L	100	mm
Tape thickness	t_{tape}	0.15	mm
Tape width		6.35	mm
Substrate thickness	$t_{\text{substrate}}$	1.5	mm
Substrate width		6.35	mm
Convection coefficient for the ambient air	h_a	10	W/m ² K
Temperature of the ambient air	T_a	20	°C
Convection coefficient for the roller	h_r	1000 [25]	W/m ² K
Temperature of the roller	T_r	100	°C
Convection coefficient for the tool	h_t	2000 [29]	W/m ² K
Temperature of the tool	T_t	20	°C

2.5 Results and discussion

The moving boundary conditions representing the motion of the placement head results in the progression of temperature as shown in Figure 2.8. The temperature distributions became steady after the nip point reached approximately 50 mm in the x-direction.

Table 2.4. Temperature dependent material properties of unidirectional CF/PEEK [30]

Temperature (°C)	Density (kg/m ³)	Specific Heat (J/kg°C)	Thermal conductivity (W/m°C)	
			Fiber direction	Transverse
0	1601	800	3.5	0.42
50	1598	930	4.6	0.52
100	1593	1040	5.1	0.6
150	1586	1260	5.9	0.7
200	1575	1300	5.9	0.7
250	1563	1400	6.1	0.7
300	1551	1550	6.7	0.75
350	1537	1650	6.8	0.68
400	1524	1700	7	0.65

Because of that, the temperatures of the tape and substrate were obtained from the node at the center of the tape in the y-direction at 75 mm in the x-direction from the beginning of the tape.

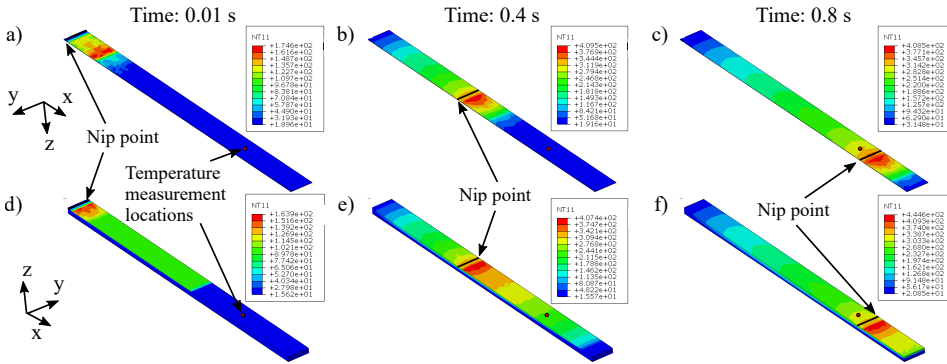


Figure 2.8. Temperature distribution on the bottom surface of the tape (a, b) and c) and the top surface of the substrate (d, e) and f) at different moments of the simulation as a result of the moving boundary conditions. Please note that the coordinate system of the tape is rotated 180 ° around the x-axis to have a clear view of the bottom surface.

Figure 2.9a shows the experimental and numerical temperatures during the placement of the 11th layer. This part of the temperature history shows the substrate temperature during the heating, compaction and cooling phases of LAFP, which are demonstrated in Figure 1.2. Following the heating phase, the nip point passes over the thermocouple at approximately 1.35 s, which was determined based on the peak of the thermocouple measurements. Given that the compaction length was 20 mm and the placement speed was 100 mm/s (Table 2.3), the compaction phase lasts until 1.55 s.

During the heating phase, the thermocouple measurements were very high (700–1300 °C) compared to the target nip point temperature (~ 400 °C as measured from the thermal camera). It was previously shown that a nip point temperature above 550 °C at a placement speed of 100 mm/s leads to significant degradation of the composite material [31]. However, no sign of degradation (smoke, flashes, etc.) was observed during the placement experiments. This means that the thermocouple measurements under direct laser illumination are not representative for the actual temperature of the composite.

The unexpectedly high temperature readings are thought to be a result of the distorted composite material around the thermocouple after the spot welding process. Due to the change in the incident angle, the residues created hot spots near the thermocouples, which can also be seen in Figure 2.7. Also, the amount of contact between the thermocouple and substrate may have varied between experiments. The lack of contact between the thermocouples and composite surface has been shown to be a source of excessive heating of the thermocouple [21]. This led to the high standard deviation during the heating phase. During the compaction phase, the standard deviation reduced significantly. The contact between the thermocouple and the surrounding composite material was established under the compaction roller.

As shown in Figure 2.9a, the thermal model deviated from the thermocouple measurements significantly until the thermocouple was fully compacted between the 10th and 11th layers. However, during the cooling period in Figure 2.9a and the placement of the subsequent layers (shown in Figure 2.9b–e), the results of the model were in close agreement with the thermocouple measurements. The results demonstrate the capability of the model to predict the temperature history within the fiber placed laminate.

The comparison of the model predictions with the substrate temperature obtained from the thermal camera can be found in Figure 2.10. The correlation between the model predictions and thermal camera measurements was much closer than the substrate temperature obtained by thermocouples, shown by the heating part of Figure 2.9a. The difference between the numerical and experimental temperatures at the nip point and at 20–40 mm from the nip point can be attributed to two factors inherent to thermal camera measurements during LAFP: the difficulty in capturing the exact nip point location from the thermal camera due to the inclined viewing angle and the reflections of the tape and the fiber placement head on the substrate in the thermal image.

In addition to its aid in studying the consolidation mechanisms, the thermal model can be used for additional goals owing to its design. For example, the capability of sequential modelling can be used to study the effect of cooling time between the placement of each layer. This can be useful for the analysis of very high placement speeds or small specimens, where a new layer is added before the previous layer cools down to the ambient temperature. Also, the heat input on the tape and substrate surfaces is designed modular so any surface heating model can be applied. This means that fiber placement processes with other types of heat sources such as a VCSEL heater, flashlight lamp, infrared heater or hot gas torch can potentially be modelled using the same thermal model, provided that the heat source model is available.

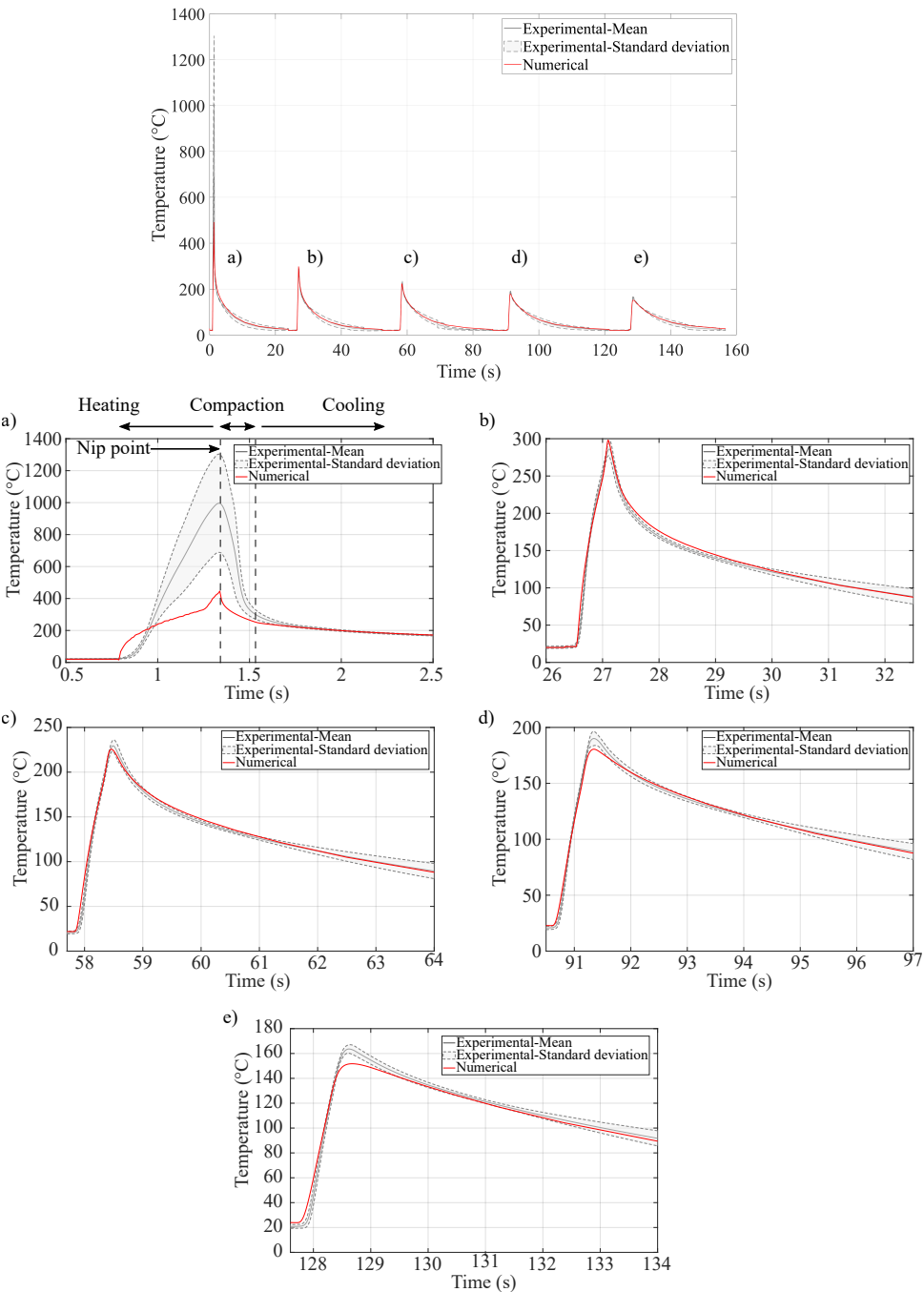


Figure 2.9. Experimental and numerical temperatures on the top surface of the 10th layer during the placement of the 11th to 15th layers (whose close-ups are shown in a) to e), respectively) of a 15-layer laminate.

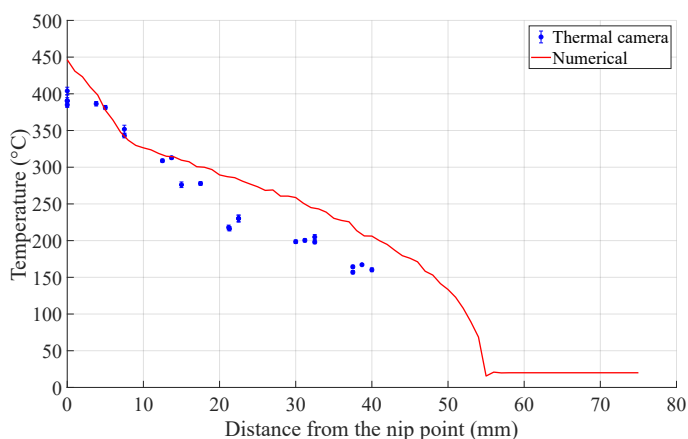


Figure 2.10. Substrate temperature measured with the thermal camera and predicted with the thermal model.

2.6 Conclusion

A 3-dimensional, Lagrangian, transient thermal model of the LAFP process with the capability of simulating sequential placement of tapes was developed. The model was coupled with an optical model from the literature and successfully validated with thermocouple and thermal camera measurements from fiber placement experiments. In the subsequent chapters, the temperature history obtained from the model will be used to understand the consolidation mechanisms during LAFP.

2.A Appendix: Mesh and time step convergence of the thermal model

A mesh convergence study was conducted to determine the number of elements along the longitudinal and transverse directions of the tape and substrate. The number of elements in the width direction was fixed to 6 to comply with the output of the optical model. The output that was assessed to find the converged mesh configuration was the temperature of the top surface of the substrate and the temperature on the bottom surface of the tape. These two temperatures are the most significant factors to determine the nip point temperature.

The effect of the number of elements in the thickness direction of the substrate on the temperature history at the top surface of the substrate is shown in Figure 2.11a. A mesh with 5 elements resulted in a significant difference in the temperature history. Models with more than 10 elements resulted in similar overall temperature histories. Then, the final number of elements was determined based on the maximum temperature as demonstrated in Figure 2.11b. This figure shows that 50 uniform elements in the thickness is sufficient to obtain a converged maximum temperature on the top sur-

face of the substrate. However, using a biased element configuration (reduced element thickness near the top surface of the tape), the same accuracy could be achieved with 15 elements. Therefore, the substrate was meshed with 15 biased elements (thickness ranging between 0.025 mm and 0.25 mm, thinner near the top surface) in the converged model.

Figure 2.12a demonstrates the effect of the number of elements in the thickness direction of the tape on the temperature history at the bottom surface of the tape. The number of elements did not affect the temperature history significantly. Figure 2.12b shows that a converged maximum temperature can be obtained with 8 elements in the thickness direction.

Figures 2.13 and 2.14 show the influence of the number of elements in the longitudinal direction on the temperature on the top surface of the substrate and the bottom surface of the tape, respectively. As demonstrated in Figure 2.13a and Figure 2.14a, not much difference was observed at the temperature histories for the number of elements in the range of 80–160. Therefore, the maximum temperatures presented in Figure 2.13b and Figure 2.14b were used to determine the number of elements. For both the tape and the substrate, 120 elements in the longitudinal direction resulted in a converged maximum temperature.

The time step used to make calculations affected the temperature history as well. Figure 2.15a and Figure 2.16a demonstrate the effect of the time step on the temperature histories at the top surface of the substrate and the bottom surface of the tape, respectively. Time steps smaller than 0.01 s had similar temperature histories. This was also confirmed with the maximum temperatures reported at Figure 2.15b and Figure 2.16b. For time steps larger than 0.01 s, the maximum temperature varied significantly. During transient forced convection analyses, too large time steps might lead to instabilities in the temperature calculations [26]. As a result, the time step for the final model was chosen as 0.01 s.

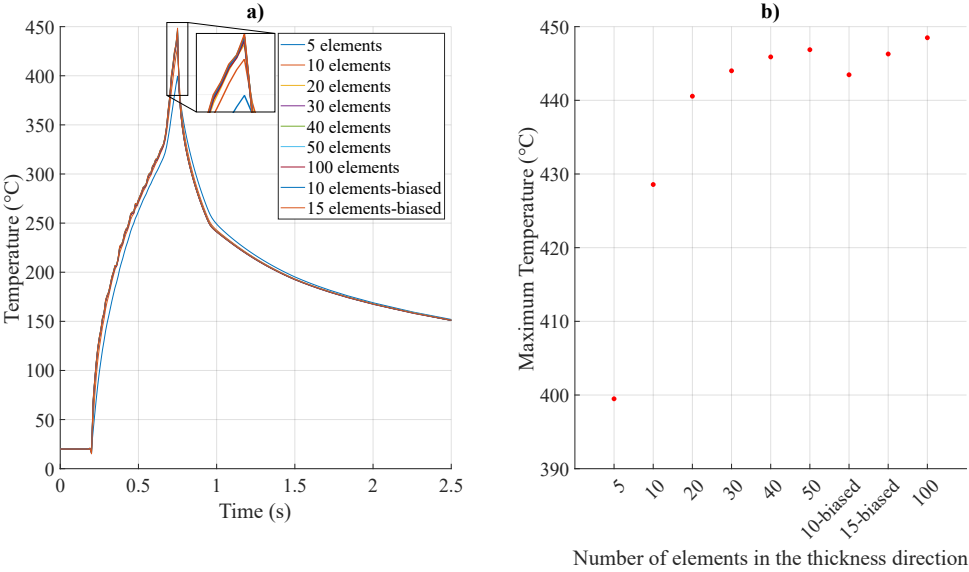


Figure 2.11. The effect of the element count in the thickness direction of the substrate on a) the temperature history, b) the maximum temperature on the top surface of the substrate.

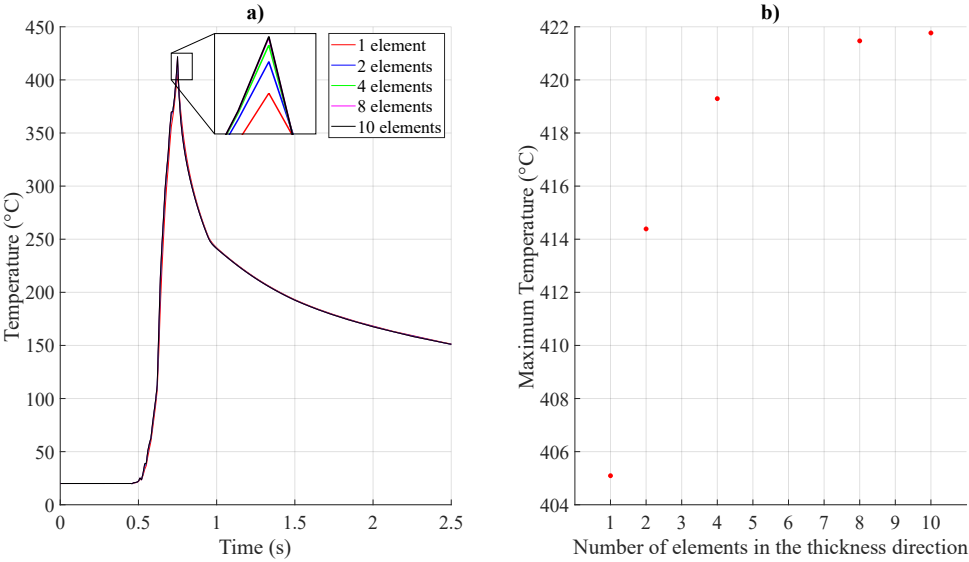


Figure 2.12. The effect of the element count in the thickness direction of the tape on a) the temperature history, b) the maximum temperature on the bottom surface of the tape.

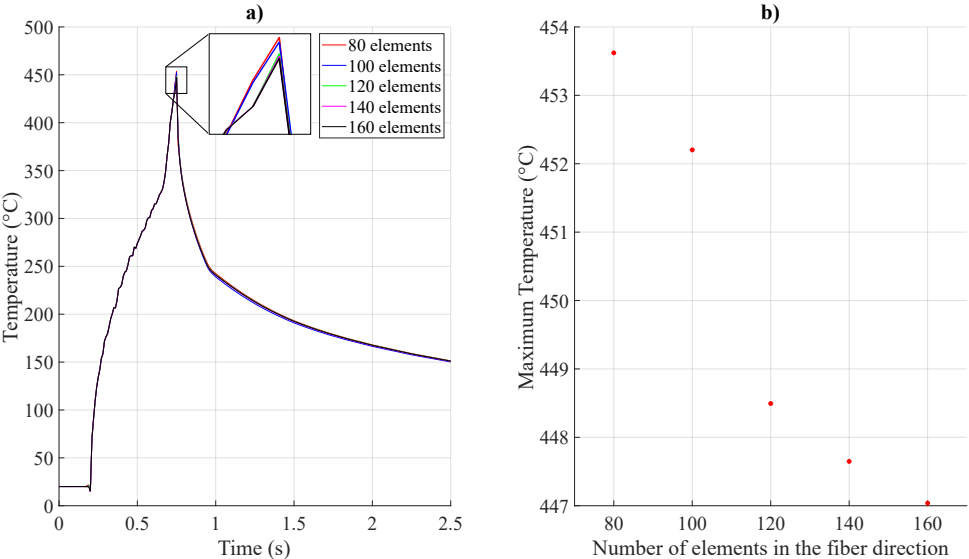


Figure 2.13. The effect of the element count in the fiber direction on a) the temperature history, b) the maximum temperature on the top surface of the substrate.

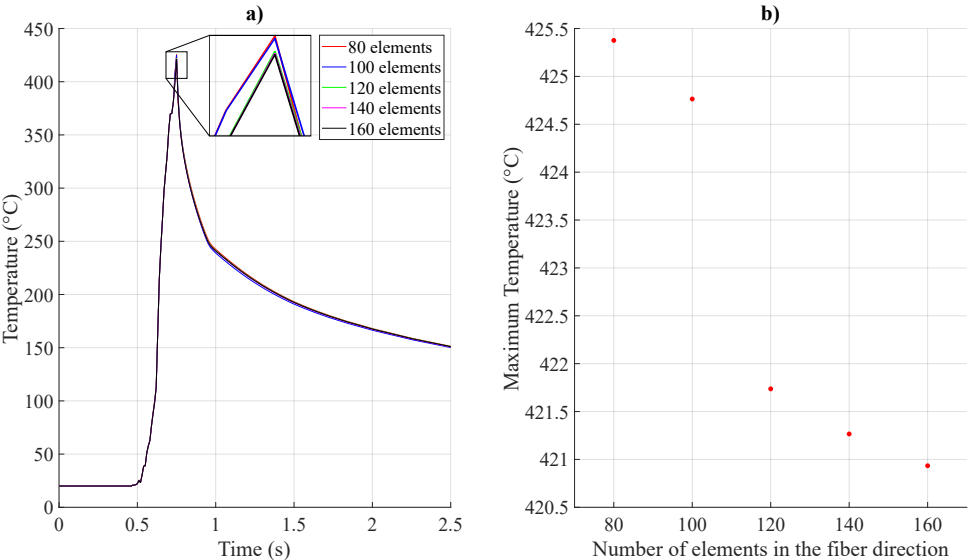


Figure 2.14. The effect of the element count in the fiber direction on a) the temperature history, b) the maximum temperature on the bottom surface of the tape.

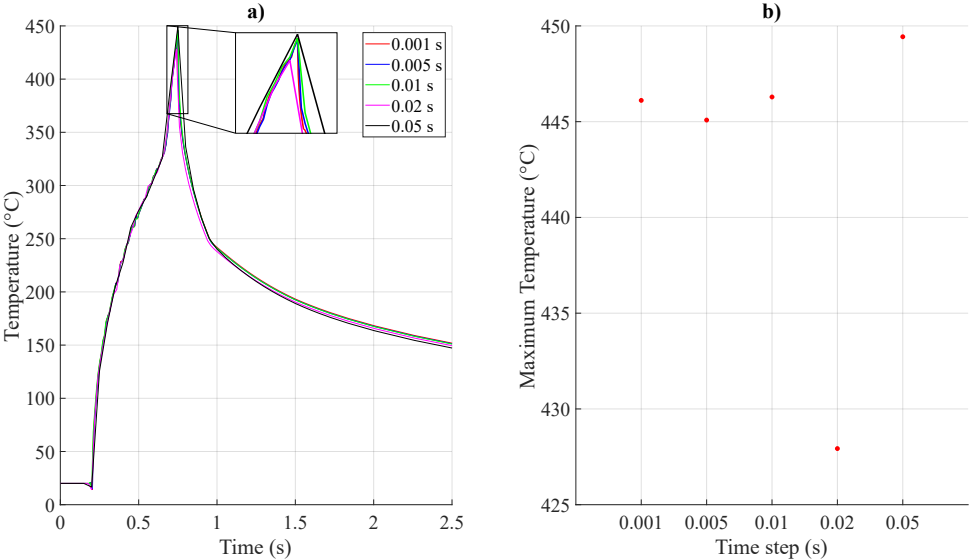


Figure 2.15. The effect of time step on a) the temperature history, b) the maximum temperature on the top surface of the substrate.

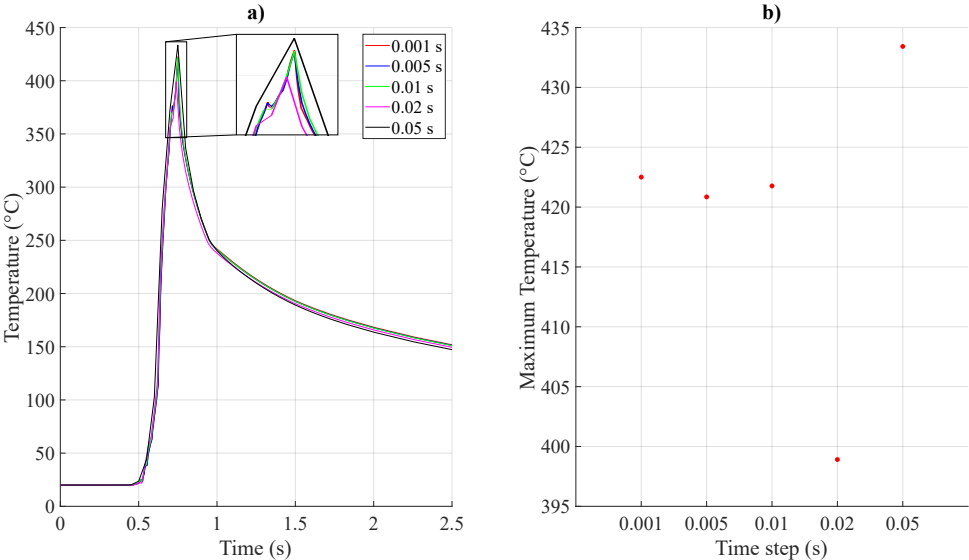


Figure 2.16. The effect of time step on a) the temperature history, b) the maximum temperature on the bottom surface of the tape.

References

- [1] Beyeler, E.P., Güçeri, S.I.. Thermal analysis of laser-assisted thermoplastic-matrix composite tape consolidation. *Journal of Heat Transfer* 1988;110(2):424–430.
- [2] Grove, S.M.. Thermal modelling of tape laying with continuous carbon fibre-reinforced thermoplastic. *Composites* 1988;19(5):367–375.
- [3] Orth, T., Weimer, C., Krah, M., Modler, N.. A review of radiative heating in automated layup and its modelling. *Journal of Plastics Technology* 2015;11.
- [4] Yassin, K., Hojjati, M.. Processing of thermoplastic matrix composites through automated fiber placement and tape laying methods: A review. 2018.
- [5] Martin, I., Saenz del Castillo, D., Fernandez, A., Güemes, A.. Advanced Thermoplastic Composite Manufacturing by In-Situ Consolidation: A Review. *Journal of Composites Science* 2020;4(4):149.
- [6] Toso, Y.M.P., Ermanni, P., Poulikakos, D.. Thermal phenomena in fiber-reinforced thermoplastic tape winding process: Computational simulations and experimental validations. *Journal of Composite Materials* 2004;38(2):107–135.
- [7] Hassan, N.. A Heat Transfer Analysis of the Fiber Placement Composite Manufacturing Process. *Journal of Reinforced Plastics and Composites* 2005;24(8):869–888.
- [8] Chinesta, F., Leygue, A., Bogner, B., Ghatat, C., Poulhaon, F., Bordeu, F., et al. First Steps Towards an Advanced Simulation of Composites Manufacturing by Automated Tape Placement. *International Journal of Material Forming* 2014;7(1):81–92.
- [9] Lichtinger, R., Hörmann, P., Stelzl, D., Hinterhölzl, R.. The effects of heat input on adjacent paths during Automated Fibre Placement. *Composites Part A: Applied Science and Manufacturing* 2015;68:387–397.
- [10] Jeyakodi, G.K.. Finite Element Simulation of the In - Situ AFP process for Thermoplastic Composites using Abaqus. 2016.
- [11] Weiler, T., Emonts, M., Wollenburg, L., Janssen, H.. Transient thermal analysis of laser-assisted thermoplastic tape placement at high process speeds by use of analytical solutions. *Journal of Thermoplastic Composite Materials* 2018;31(3):311–338.
- [12] Schaefer, P.M., Gierszewski, D., Kollmannsberger, A., Zaremba, S., Drechsler, K.. Analysis and improved process response prediction of laser-assisted automated tape placement with PA-6/carbon tapes using Design of Experiments and numerical simulations. *Composites Part A: Applied Science and Manufacturing* 2017;96:137–146.
- [13] Di Francesco, M., Veldenz, L., Dell'Anno, G., Potter, K.. Heater power control for multi-material, variable speed Automated Fibre Placement. *Composites Part A: Applied Science and Manufacturing* 2017;101:408–421.

- [14] Grouve, W.J.B.. Weld Strength of Laser-Assisted Tape-Placed Thermoplastic Composites. Ph.D. thesis; University of Twente; 2012.
- [15] Kollmannsberger, A.. Heating characteristics of fixed focus laser assisted Thermoplastic-Automated Fiber Placement of 2D and 3D parts. Ph.D. thesis; Technical University of Munich; 2019.
- [16] Zaami, A., Schäkel, M., Baran, I., Bor, T.C., Janssen, H., Akkerman, R.. A fully coupled local and global optical-thermal model for continuous adjacent laser-assisted tape winding process of type-IV pressure vessels. *Journal of Composite Materials* 2020;(August).
- [17] Hosseini, S.M.A., Schäkel, M., Baran, I., Janssen, H., van Drongelen, M., Akkerman, R.. A new global kinematic-optical-thermal process model for laser-assisted tape winding with an application to helical-wound pressure vessel. *Materials & Design* 2020;193:108854.
- [18] Agarwal, V., Guceri, S.I., McCullough R. L., , Schultz, J.. Thermal Characterization of the Laser-Assisted Consolidation Process. *Journal of Thermoplastic Composite Materials* 1992;5(2):115–135.
- [19] Mantell, S.C., Springer, G.S.. Manufacturing Process Models for Thermoplastic Composites. *Journal of Composite Materials* 1992;26(16):2348–2377.
- [20] Mantell, S.C., Wang, Q., Springer, G.S.. Processing Thermoplastic Composites in a Press and by Tape Laying–Experimental Results. *Journal of Composite Materials* 1992;26:2378–2401.
- [21] Stokes-Griffin, C.M., Compston, P.. A combined optical-thermal model for near-infrared laser heating of thermoplastic composites in an automated tape placement process. *Composites Part A: Applied Science and Manufacturing* 2015;75:104–115.
- [22] Kok, T.. On the consolidation quality in laser assisted fiber placement: the role of the heating phase. Phd thesis; University of Twente; 2018.
- [23] Tafreshi, O.A., Hoa, S.V., Shadmehri, F., Hoang, D.M., Rosca, D.. Heat transfer analysis of automated fiber placement of thermoplastic composites using a hot gas torch. *Advanced Manufacturing: Polymer and Composites Science* 2019;5(4):206–223.
- [24] Zaami, A., Schäkel, M., Baran, I., Bor, T.C., Janssen, H., Akkerman, R.. Temperature variation during continuous laser-assisted adjacent hoop winding of type-IV pressure vessels: An experimental analysis. *Journal of Composite Materials* 2019;.
- [25] Hosseini, S.M.A., Baran, I., van Drongelen, M., Akkerman, R.. On the temperature evolution during continuous laser-assisted tape winding of multiple C/PEEK layers: The effect of roller deformation. *International Journal of Material Forming* 2020;;1–19.
- [26] Dassault Systèmes, . ABAQUS 2017 Documentation. 2017.

- [27] Stokes-Griffin, C.M., Compston, P. Optical characterisation and modelling for oblique near-infrared laser heating of carbon fibre reinforced thermoplastic composites. *Optics and Lasers in Engineering* 2015;72:1–11.
- [28] Reichardt, J., Baran, I., Akkerman, R.. New analytical and numerical optical model for the laser assisted tape winding process. *Composites Part A: Applied Science and Manufacturing* 2018;107:647–656.
- [29] Leon, A., Argerich, C., Barasinski, A., Soccard, E., Chinesta, F. Effects of material and process parameters on in-situ consolidation. *International Journal of Material Forming* 2019;12(4):491–503.
- [30] Cogswell, F.N.. *Thermoplastic aromatic polymer composites: a study of the structure, processing, and properties of carbon fibre reinforced polyetheretherketone and related materials*. Butterworth-Heinemann; 1992.
- [31] Stokes-Griffin, C.M., Compston, P. The effect of processing temperature and placement rate on the short beam strength of carbon fibre-PEEK manufactured using a laser tape placement process. *Composites Part A: Applied Science and Manufacturing* 2015;78:274–283.

Chapter 3

Deconsolidation of Thermoplastic Prepreg Tapes During Rapid Laser Heating

In this study, the effect of rapid laser heating, which is typical during laser-assisted fiber placement (LAFP), on the micro- and meso- structure of the thermoplastic tape was investigated. Thermoplastic tapes were heated above the melting temperature with different heated lengths (30 and 80 mm) and heating times (0.2 and 0.8 s) in a dedicated experimental setup. In-situ and ex-situ characterization techniques were used to observe the differences between the micro- and meso- structure of the tape before and after heating. The experiments resulted in significant changes in the tape structure, namely increased out-of-plane deformation, waviness, arc-length width, roughness, thickness and volumetric void content. This study shows for the first time that a unique deconsolidation behavior takes place during the heating phase of LAFP: the deconsolidation mechanisms are exacerbated by the non-uniform temperature at the tape surface, which is caused by roughness increase and waviness formation.

This chapter is based on: Çelik, O., Choudhary, A., Peeters, D., Teuwen, J., Dransfeld, C., Deconsolidation of thermoplastic prepreg tapes during rapid laser heating. Composites Part A: Applied Science and Manufacturing, 106575, Volume 149, 2021.

3.1 Introduction

Strict limitations on CO₂ emissions pushes the aerospace and automotive industry to produce more efficient vehicles with alternative energy sources. This makes weight reduction one of the primary goals for these industries. High performance composite materials provide a solution to the weight reduction problem owing to their high specific strength compared to conventional structural materials. Recently, the interest in thermoplastic composites have emerged since they can be recycled [1] and are suitable for automation due to their short processing cycles.

Laser-assisted fiber placement (LAFP) with in-situ consolidation is an automated manufacturing method for thermoplastic composite structures. During the process, thermoplastic composite tape and substrate are locally melted with a laser heater aimed at the nip point and joined with a compaction roller as shown in Figure 3.1. No post-consolidation step is applied in an autoclave, press or oven to give the part its final structure. The process has the potential to reduce material scrap by producing near net-shape parts and decrease energy consumption by eliminating the post-consolidation step.

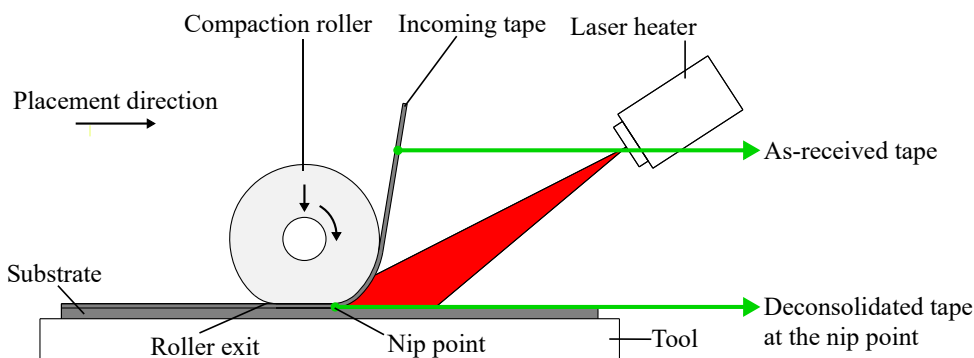


Figure 3.1. Typical LAFP process. The as-received and deconsolidated forms of the incoming tape are highlighted.

Achieving in-situ consolidation is not straightforward and requires rigorous understanding about the link between the process parameters and the resulting part quality. Several models including tape consolidation [2], intimate contact development [3–5] and void reduction [6] have been used to predict the final geometry and porosity of the laminate. These models require information about the initial state of the tape such as the dimensions, surface profile or void content and then, using the temperature and pressure history of a given process, calculate the micro- and meso-scale changes during manufacturing. This information is usually obtained from the as-received tape.

For conventional composite manufacturing techniques such as autoclave consolidation or press molding, obtaining such parameters from the as-received tapes may not influence the accuracy of the predictions due to comparably slow heating rates ($< 20^\circ\text{C/s}$) and long dwell times (on the order of minutes). However, during LAFP, heating rates are much higher (up to 2000°C/s) and no compaction pressure is applied on the tape during heating. Besides, laser heating relies on radiation, whereas the material is

heated by conduction/convection during conventional manufacturing techniques. This might lead to a different heat flux and temperature distribution during heating. Moreover, following the heating phase, compaction of the tape and the substrate can only occur during the limited time spent under the compaction roller (< 1 s). This means that any change in the micro-structure during the heating phase can be expected to have a more pronounced effect on an in-situ consolidated part compared to a conventionally manufactured part. Albeit originally developed for conventional methods, the above-mentioned models have been used to predict the quality of the parts manufactured with LAFP [7–10]. It has been assumed that the properties of the as-received tape does not change during the heating phase of the LAFP process.

The negative changes in the micro- and meso-structure of a thermoplastic composite material at high temperature in the absence of pressure are termed as *deconsolidation* [11]. It has been studied mostly for reheating/cooling of pre-consolidated composite laminates, which is typically encountered in applications such as resistance welding [12], induction welding [11] and stamp forming [13]. Four different mechanisms have been identified as the source of deconsolidation of pre-consolidated laminates so far:

- Void growth, motion and coalescence [14–16],
- Decompression of the fiber-matrix network due to release of residual stresses in the preform [17],
- Thermal expansion and viscoelastic behavior of the resin [18],
- Thermal expansion of dissolved moisture in the resin [13].

Deconsolidation of an individual layer of CF/PEEK prepreg material was investigated in the recent works of Slange et al. [13] and Krämer et al. [19]. In the work of Slange et al. [13], three different initial conditions were studied: as-received prepreg plies, plies which were annealed below the melting temperature for 3 h and plies that were press-consolidated above the melting temperature for 20 min. The same deconsolidation treatment was applied on these specimens by reheating them in an oven at 390 °C for 1 h. The as-received and annealed plies were significantly affected by the deconsolidation treatment as an increase in surface roughness due to loose dry fibers at the surface and local out-of-plane waviness were observed. On the contrary, press consolidated plies remained intact after the deconsolidation treatment. They hypothesized that the plies deconsolidated due to the residual stresses introduced during the prepreg manufacturing process. Krämer et al. investigated in-plane waviness formation for single-ply 300×300 mm² CF/PEEK sheets during heating on a hot plate under vacuum [19]. It was shown that in-plane waviness formed during cooling between the melting and crystallization temperatures of the polymer. It was discussed that the main contributor to in-plane waviness formation is the compressive stress on the fibers caused by tool-ply interaction. They observed the waviness formation using an optical camera, which does not provide the height information of the tape surface. Therefore, out-of-plane waviness, which is more relevant to inter-ply porosity in the final laminate than in-plane waviness, was not quantified and its formation was not discussed. Moreover, these studies were performed under conditions similar to hot press or oven processing, leading to low heating rates as previously mentioned.

While a substantial amount of work has been done on characterizing the deconsolidation behavior of pre-consolidated laminates under slow heating rates, there is very little research performed on individual layers of tape under rapid laser heating. Kok et al. attempted to capture the deconsolidated state of the tape by reducing the compaction pressure applied by a LAFP machine using shims and placing the tape on a cold tool to freeze the microstructure as soon as possible [20]. Cross-sectional micrographs of the tapes placed with reduced pressure suggested that the heated surface of the CF/PEEK prepreg tape is rougher and has more dry fibers compared to the pristine tape. In a follow-up study, they quantified the through-thickness fiber, resin and void content in the cross-sections and concluded that the effects of deconsolidation can be observed up to 20 μm from the heated tape surface, which corresponds to 15 % of the initial tape thickness [21]. Their work highlights the importance of the heating phase of LAFP; however, the measurements were made after the tape was placed on the tool and cooled down. Therefore, there is still a knowledge gap about the state of the tape at the nip point and the evolution of deconsolidation from the beginning of heating until the nip point (denoted in Figure 3.1).

Moreover, the experiments in the literature were conducted for a specific set of laser settings and placement speed. Therefore, the effects of different heating conditions remain unresolved. There are studies which claim that increasing the heated length of the tape is beneficial for bonding because the heat soak in the tape prevents rapid cooling under the compaction roller [22, 23]. Recent advances in laser heating technology such as Vertical-Cavity Surface-Emitting Lasers (VCSEL) or zoom homogenizers make it possible to adjust the heated length during processing [24]. Also, the response of the material under different placement speeds (leading to different heating times) is of interest since a wide range of placement speeds (100-400 mm/s [25]) have been reported in the literature. To use the full potential of tailoring the heating phase of the LAFP process for different placement speeds, one must discover the extent of deconsolidation and underlying mechanisms for different heated lengths and heating times.

The objective of this paper is therefore to understand how the micro- and meso-structure of the thermoplastic tape is influenced during rapid laser heating, considering different heated lengths and heating times. To do that, a novel experimental setup was designed to measure the temperature and surface profile of the thermoplastic tape *in-situ* during heating with a laser heater. Geometric tape properties such as waviness, out-of-plane deformation and arc length width were calculated from in-situ profile measurements. Additionally, the surface roughness, void content and thickness were measured ex-situ for additional insight on the deconsolidation mechanisms.

3.2 Materials and Methods

3.2.1 Experimental Setup

The experimental setup designed for creating varying heated lengths and heating times and measuring the temperature and surface deformation in-situ during laser heating is shown in Figure 3.2. The setup comprises an aluminum tool which was designed to hold a piece of composite tape in place. A VCSEL laser heat source was pointed towards

the tape with an angle of 45° from the table surface. A thermal camera and a laser line scanner were used to capture the temperature and surface deformation, respectively.

The laser heat source is a TRUMPF PPM411-12-980-24 laser module, with a total output capacity of 2.4 kW. The device contains 12 heating zones which may be independently activated to get a tailored heating profile. The emitted infrared radiation has a wavelength of 980 nm [26]. The independent heating zones of the VCSEL heater were selectively activated and the laser power was adjusted to obtain different heated lengths and heating times.

Temperature on the tape surface during heating was measured in-situ with a FLIR A655sc long-wave infrared (LWIR) camera. The detector of the camera has a resolution of 640×480 pixels which corresponds to ~ 0.25 mm/pixel in this setup. The thermal images were captured at a sampling rate of 25 Hz. The accuracy of the temperature measurement is $\pm 2^\circ\text{C}$ or $\pm 2\%$ (whichever is greater). The camera was calibrated in the range of 100 – 650°C .

For in-situ surface profile measurements, a Micro-Epsilon scanCONTROL 2950-25 laser line scanner (LLS) was used. The sensor operates according to the principle of optical triangulation. First, a laser line is projected onto the target surface via a linear optical system. Then, the diffusely reflected light from the laser line is replicated on a sensor array and evaluated in two dimensions [27]. The tape profile was sampled with 100 Hz during heating. The resolution in the tape thickness direction was $2\mu\text{m}$. The maximum resolution in the tape width direction was $\sim 20\mu\text{m}$. The resolution values were reported for ideal conditions. They might be influenced by the reflectivity of the prepreg in melt conditions.

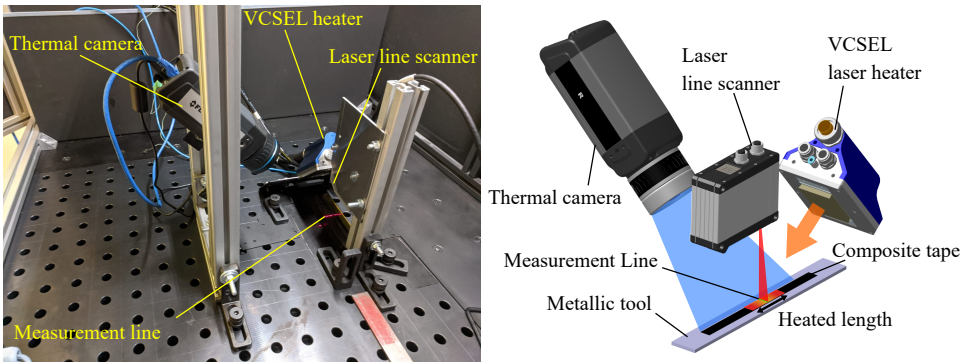


Figure 3.2. The experimental setup to measure temperature and surface profile in-situ during rapid heating of the composite tape and its schematic description.

3.2.2 Tape Deconsolidation Experiments

The experiments were conducted using TC1200 carbon-fiber reinforced polyether-ether-ketone (CF/PEEK) prepreg tapes produced by Toray Advanced Composites with a fiber volume fraction of 59 %. The tapes were in a 12.7 mm ($\frac{1}{2}$ in.) wide-slit form. Relevant physical properties supplied by the manufacturer and geometric properties mea-

sured from cross-sectional images of the as-received tape are given in Table 3.1. For each experiment, a 100 mm-long prepreg tape sample was positioned on the tool surface and fixed with Kapton tapes at the edges.

Table 3.1. Measured geometric properties of the as-received CF/PEEK tape along with physical properties provided by the manufacturer. The values in parentheses show the standard deviation for the measured properties.

Glass transition temperature (T_g) (°C)	Melting temperature (T_m) (°C)	Thickness (μm)	Width (μm)	Volumetric void content (%)	RMS surface roughness (μm)
143 [28]	343 [28]	151.34 (7.7)	12627 (50)	0.71 (0.10)	1.69 (0.39)

Two heated lengths, namely 30 mm and 80 mm, were examined. These values represent the lower and higher extreme cases for most of the heated lengths reported in the literature (e.g., 30 mm [29], 52 mm [22], 60 mm [30]). The experiments were performed with two different heating times, namely 0.2 s and 0.8 s. The heating time was bounded on the lower end with the available laser power to heat the material to a temperature above the melting temperature. The high heating time was determined so that the maximum temperature was reached in a similar manner to a rather slow placement speed in the actual LAFP process (37.5 mm/s, calculated for the heated length of 30 mm). The target temperature on the tape at the measurement area for each heated length and heating time was 360 °C. However, due to deformation of the tape at increased temperatures, a range between 340-400 °C was observed. This choice was made based on the achievable temperature above the melting point of the material with the shortest heated length and heating time.

To obtain the variations in the heated length, different zones on the VCSEL heater were activated. To reach the target temperature at the predefined heating time, the power level at each heating zone was adjusted. Table 3.2 provides the laser settings used in the experiments. Four samples were tested at each laser setting.

Table 3.2. Laser settings used in the experiments.

Experiment	Heated length (mm)	Heating time (s)	VCSEL zones activated	Power in each zone (%)	Total input power (W)	Equivalent placement speed (mm/s)
1	30	0.2	7-9	100	600	150
2	30	0.8	7-9	37	222	37.5
3	80	0.2	1-11	90	1980	400
4	80	0.8	1-11	30	660	100

3.2.3 In-situ Measurements

The surface profile and temperature along the width of the tape were measured at the center of the prepreg tape in the length direction ("Measurement Line" in Figure 3.2) during laser heating. The aim of the in-situ measurements was to understand the changes between the as-received tape and the deconsolidated tape at the nip point during the

actual LAFP process (please refer to Figure 3.1). The measurements before heating represented the as-received tape, whereas the measurements just after heating represented the deconsolidated tape at the nip point.

It should be noted that some assumptions are inherent when the state of the tape at the end of heating in the tape deconsolidation experiments is accepted as the state at the nip point in an actual LAFP process. Firstly, the reflection of the laser beams from the substrate on the tape are not considered. The tape is illuminated by only the laser heater and no secondary reflections are present in the experimental setup. Secondly, the cooling of the tape in the shadow prior to the nip point was neglected. The time spent in the shadow is highly dependent on the shape of the compaction roller and placement speed, and varies between a few to tens of milliseconds [8]. Finally, the tapes were heated in a static setup aiming increased control over the heating parameters and collection of high quality data, whereas the tape is heated dynamically during the LAFP process. The incoming tape passes through the laser illuminated zone with the prescribed placement speed, as shown in Figure 3.1. This might lead to a different through-thickness temperature gradient and influence the laser-affected zone in the thickness direction.

Surface Profile

To compare the as-received tape and the deconsolidated tape at the nip point, four quantities were calculated from the surface profile measurements at the end of heating: the maximum out-of-plane (OP) deformation, the wavelength/maximum amplitude of the waviness curves and the width of the tape. The maximum OP deformation was calculated by subtracting the average height of the initial tape from the highest peak of the profile at the end of the heating phase. The waviness curves were obtained by applying a Gaussian filter [31] with a cut-off wavelength of 0.8 mm to the raw data according to the ISO 4288 standard [32]. An example is demonstrated in Figure 3.3. In the waviness curves, the vertical and horizontal distances between the maximum peak and the minimum valley were termed as the maximum amplitude (A) and the half wavelength ($\lambda/2$). It was observed that due to warpage of the tape during heating, the projected width was not representative of the actual width of the tape. Hence, the captured surface profile was used to obtain the arc-length width of the specimens, which is also shown in Figure 3.3.

To observe the changes in the tape *during* the heating process, time-dependent data was also analyzed. The OP deformation during heating was calculated as the height difference between the tape profile at the analyzed time step and the initial tape profile, normalized by dividing with the initial tape thickness of 0.15 mm. This data was used for qualitative purposes only since abnormal spikes were observed in the surface profiles of a significant amount of specimens. The cause for this is thought to be the reflection of the laser beams emitted from VCSEL heater on the deforming tape surface. It is believed that some of the reflected beams were captured by the LLS, causing irregularities in the surface profile measurement during heating. As soon as the laser heating ended, such disturbances disappeared.

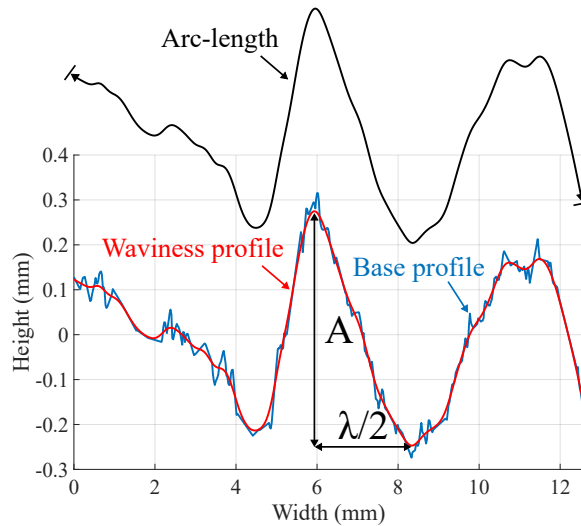


Figure 3.3. An example profile obtained from LLS and the corresponding waviness curve. The maximum amplitude (A), the associated half-wavelength ($\lambda/2$) and the arc-length width of the tape are demonstrated.

Temperature

Temperature during heating was extracted from measurement lines placed perpendicular to the fiber direction of the tape as shown in Figure 3.4 for each specimen. The location of the measurement lines was determined such that they cover the whole tape width and overlap with the projection of the laser beams emitted from the laser line scanner on the tape (shown in Figure 3.2). The emissivity of the tape was calibrated according to the ASTM E1933 standard [33] and found to be 0.84.

Temperature history and time-dependent surface profile data were synchronized after the experiments were completed. LLS measurements were converted to Comma Separated Value (.csv) files using the ScanCONTROL 3D software. The temperature measurements were exported in Matlab-formatted data format (.mat) using the ResearchIR software. Both sets of data were imported to Matlab software and arranged in two separate matrices so that each row shows the surface profile and temperature at a given frame. The surface profile data was cropped manually so that only the tape surface is included. This procedure was not required for the temperature profiles, as the measurement line was already defined to cover the tape width only, as shown in Figure 3.4. The final step of the synchronization was the time-wise alignment of both sets of data. The frame at which the heating started was used to align both datasets. This was manually found in the temperature data based on the increase in temperature on the measurement line. In the surface profile data, the beginning of heating was marked by reflections on the tool surface as shown in Figure 3.5.

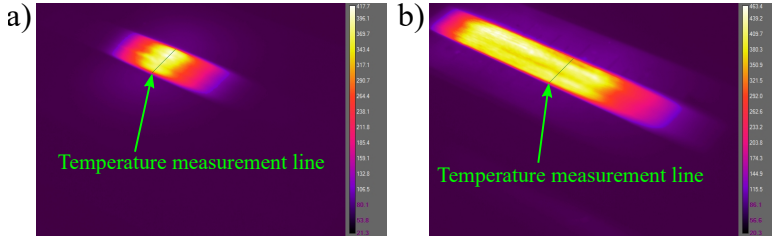


Figure 3.4. Representative thermal images of samples heated with heated lengths of a) 30 mm b) 80 mm.

3

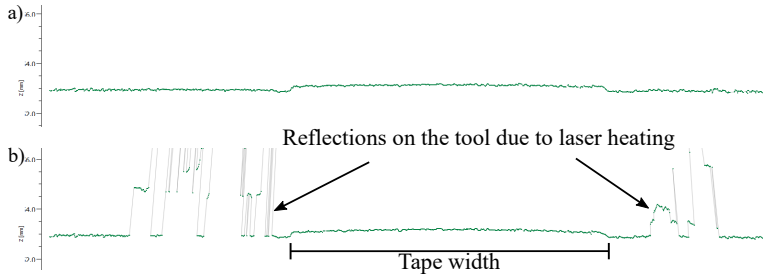


Figure 3.5. Example of the surface profile of the tape and the tool a) before heating, b) at the moment heating started.

3.2.4 Ex-situ Measurements

Ex-situ surface roughness, void content and thickness measurements were used to explain deconsolidation mechanisms in more detail with a resolution that could not be achieved during the in-situ measurements. These measurements were performed after the tape cooled down to room temperature; therefore, they may not fully represent the state of the tape at the nip point.

Surface Roughness

An Olympus OLS 3100 laser scanning confocal microscope (LSCM) was used to measure the local surface roughness. Due to the limitations of the equipment, four confocal images were captured for each specimen at 20%, 40%, 60% and 80% of the tape width. These images were captured at 20 \times magnification, which corresponds to an area of 640 μm (along the fiber direction) \times 480 μm (transverse to the fiber direction). From these measurements, ten line surface profiles were extracted along the direction transverse to the fibers. Following the guidelines in the ISO 4288 standard [32], a high-pass filter of 96 μm was applied to each primary line profile obtained for an evaluation length of 480 μm (transverse to fiber direction) to separate roughness profile from the primary profile and remove any global curvature effects. The average root-mean-square (RMS) roughness of each image were calculated by averaging the RMS roughness of ten surface profiles. Finally, the mean RMS roughness was calculated for each specimen by averag-

ing the RMS roughness at 20%, 40%, 60% and 80% of the tape width.

Void Content and Thickness

The final void content and thickness of the composite tape were determined by cross-sectional microscopy. To prepare the cross-sectional microscopy samples, the specimens were cut with an offset of 3 mm in the fiber direction from the measurement line shown in Figure 3.2 to account for material removal during polishing and grinding. The specimens were then embedded into slow-curing mounting epoxy (Struers Epofix) and ground/polished in a Struers Tegramin-20 specimen preparation equipment. A Keyence VHX-2000 digital microscope was used to capture the cross-sectional images.

The final void content of the samples was determined using the native image analysis software of the microscope (VHX-2000 Communication Software). The voids were separated from the fibers and resin using a gray level threshold analysis, similar to the segmentation method proposed in the authors' previous work [34]. To compare the specimens heated with different laser settings, the global void content along the complete width of the tape was determined.

The final tape thickness was measured from the perpendicular distance between the top and bottom surfaces of the tapes. Similar to the void content, it was observed that the thickness at locations corresponding to the peak of the waviness curve of the surface profile was locally high. Hence, the thickness was measured at 20%, 40%, 60% and 80% of the width of the tape. Three measurements were made and averaged at each location.

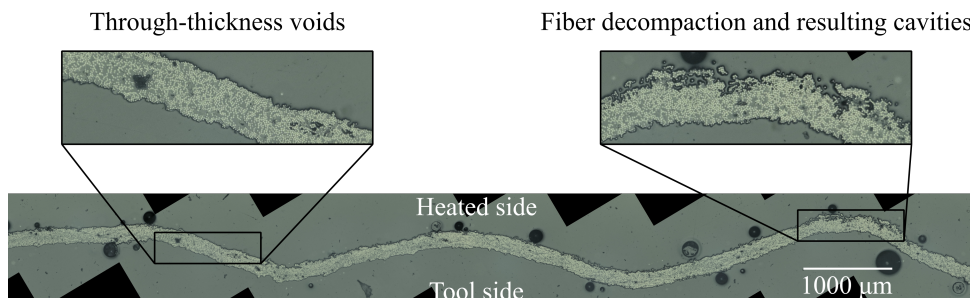


Figure 3.6. Representative cross-sectional image of a deconsolidated tape.

3.2.5 Analysis of Variance (ANOVA)

Two-way ANOVA method was applied on the results of the in-situ and ex-situ measurements to assess the effects of the heated length and heating time quantitatively. The Matlab built-in function *anovan* was used for this purpose [35]. The outputs of this function were p-values for laser settings shown in Table 3.2. p-values smaller than 0.05 imply that the mean response of the specific setting is different from the mean of all data within a confidence interval of 95 %. The effect of such a parameter can be considered statistically significant.

3.3 Results

3.3.1 Waviness at the nip point

Representative tape profiles before and after heating for each process variable are shown in Figure 3.7. The profiles after heating were captured at the end of laser heating without any further cooling so that they represent the state of the tape at the nip point in an actual LAFP process under the assumptions explained in Section 3.2.3. It can be observed that laser heating caused significant changes in the waviness of the tape in the width direction for all heating parameters. To explain the differences qualitatively, the classification scheme based on the number and distribution of waves which was proposed in the work of Thor et al. [36] can be used. In [36], two kinds of waviness are defined for distributed waves: in-phase distributed (with constant amplitude and wavelength) and stochastically distributed (with varying amplitude and wavelength) waviness. The heated length had an effect on the shape of the waviness after heating. The samples with a heated length of 80 mm (Figure 3.7b, d) resulted in in-phase distributed waviness. However, the samples with a heated length of 30 mm (Figure 3.7a, c) showed stochastically distributed waviness. Heating time did not seem to affect the shape of the waviness at the end of heating.

A quantitative assessment of the effect of laser heating on the waviness can be made with the resulting maximum amplitude (A) and wavelength (λ) values presented in Table 3.3. Assuming that the as-received tape is almost perfectly flat ($A = 0$ and $\lambda = \infty$), the laser heating process increased A and decreased λ . The maximum amplitude at the nip point state ranged between 0.21 mm (30 mm heated length, 0.8 s heating time) and 0.62 mm (80 mm heated length, 0.2 s heating time). The associated wavelength ranged between 4.24 mm (30 mm heated length, 0.2 s heating time) and 5.24 mm (80 mm heated length, 0.2 s heating time).

The heated length and the heating time had adverse effects on the maximum amplitude. Increasing the heated length from 30 mm to 80 mm caused an increase of 0.37 mm (148 %) and 0.33 mm (157 %) in the maximum amplitude for the heating times of 0.2 s and 0.8 s, respectively. Increasing the heating time from 0.2 s to 0.8 s resulted in a decrease of 0.04 mm (16 %) and 0.08 mm (13 %) in the maximum amplitude for the heated lengths of 30 mm and 80 mm, respectively. A clear trend was not observed for the wavelength for neither of the heating parameters. The effects of the heating time and heated length can be further analyzed using the results of ANOVA shown in Table 3.5. The heated length had a statistically significant effect on A ($p=0.0001$) but not on λ ($p=0.3711$). The heating time did not have a significant effect on neither A nor λ ($p=0.335$ and $p=0.8048$, respectively). This confirms the qualitative assessment on the effect of the heating time on the waviness shape.

3.3.2 Temperature history and out-of-plane deformation

Figure 3.8a and Figure 3.8b show representative synchronized temperature and OP deformation plots along the width of the tape at the measurement line (referring to Figure 3.2) for different heated lengths (30 and 80 mm). The measurements are presented from the beginning until the end of the heating. The first interesting observation was

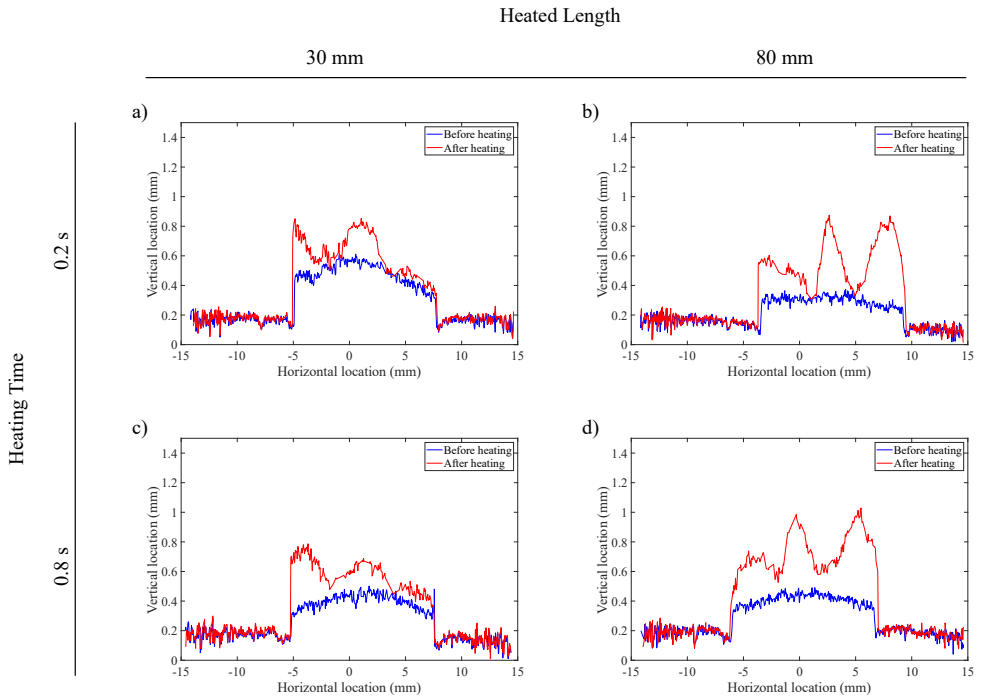


Figure 3.7. Representative surface profiles before and after heating for a) 30 mm heated length and 0.2 s heating time, b) 80 mm heated length and 0.2 s heating time, c) 30 mm heated length and 0.8 s heating time, d) 80 mm heated length and 0.8 s heating time.

Table 3.3. Process parameters and *in-situ* measurements immediately after the end of laser heating (nip point state). The values in parentheses show the standard deviation of the means of all experiments. Ideal as-received tape data is added for ease of comparison.

Heated length (mm)	Heating time (s)	Max. amplitude (A) (mm)	Wavelength (λ) (mm)	Max. OP deformation (mm)	Arc-length width change (%)
Ideal as-received tape		0	∞	0	0
30	0.2	0.25 (0.07)	4.24 (1.86)	0.48 (0.03)	2.5 (0.3)
30	0.8	0.21 (0.10)	4.89 (1.55)	0.40 (0.02)	1.4 (0.3)
80	0.2	0.62 (0.15)	5.24 (1.41)	0.64 (0.16)	5.5 (0.2)
80	0.8	0.54 (0.16)	4.70 (1.40)	0.70 (0.09)	3.9 (0.7)

Table 3.4. Process parameters and *ex-situ* measurements after the tape cooled down to room temperature. The values in parentheses show the standard deviation of the means of all experiments. As-received tape data is added for ease of comparison.

Heated length (mm)	Heating time (s)	Mean RMS roughness (μm)	Thickness increase (μm)	Volumetric void content (%)
As-received tape		1.7 (0.4)	0	0.7 (0.1)
30	0.2	6.0 (0.7)	27.3 (1.3)	3.3 (0.7)
30	0.8	6.4 (0.2)	34.5 (6.3)	4.0 (0.1)
80	0.2	7.9 (0.8)	24.8 (3.2)	3.6 (1.0)
80	0.8	13.8 (0.6)	25.6 (10.0)	4.3 (1.6)

Table 3.5. Results of ANOVA. Values in bold text show that the change in the parameter results in statistically significant changes in the response variable or the interaction between the effect of the parameters is statistically significant ($p < 0.05$).

Parameter	Max. amplitude (A)	Wavelength (λ)	Max. OP deformation	Arc-length (%) width increase	Max. RMS roughness	Thickness increase	Volumetric void content
Heated length	0.0001	0.6138	0.0012	0.0000	0.0000	0.2285	0.7043
Heating time	0.3711	0.9415	0.7885	0.0002	0.0000	0.3824	0.3406
Interaction	0.8060	0.4649	0.2347	0.3112	0.0000	0.4787	0.9452

that the temperature during heating was not uniform although the VCSEL laser heater provides a nearly homogeneous irradiance in the width direction [37]. In the beginning of the heating process, the temperature variation along the width of tape specimens was $\sim 0.8\%$. However, as the temperature exceeded T_g (at 150-200 ms from the beginning of heating), temperature variation started increasing. By the time some parts of the tape exceeded T_m (at 500-800 ms from the beginning of heating), temperature variations of up to 50 % were observed along the width.

Comparison of the temperature and the deformation history of the tape yielded further interesting results. At the moment the temperature exceeded T_g over the width, a sudden increase in the deformation was observed. Afterwards, the material deformed steadily until T_m was reached. At 500-800 ms (depending on the location in the width direction), T_m was reached and the material deformed drastically, causing significant waviness in the tape. It can be seen that the high and low values in the temperature plots followed a similar trend with the peaks and valleys in the deformation plots, respectively.

The maximum OP deformation at the nip point for different heating parameters is shown in Table 3.3. Laser heating caused OP deformation for all cases. The maximum OP deformation at the nip point state ranged between 0.40 mm (30 mm heated length, 0.8 s heating time) and 0.70 mm (80 mm heated length, 0.8 s heating time). Increasing the heated length from 30 mm to 80 mm resulted in an increase of 0.16 mm (33 %) and 0.30 mm (75 %) in the maximum OP deformation for the heating times of 0.2 s and 0.8 s, respectively. A clear trend was not observed for the effect of the heating time on the maximum OP deformation. Statistical significance of the effects of the heating time and heated length on maximum OP deformation are assessed in Table 3.5. ANOVA indicated that the effect of heated length was statistically significant ($p=0.012$) whereas the effect

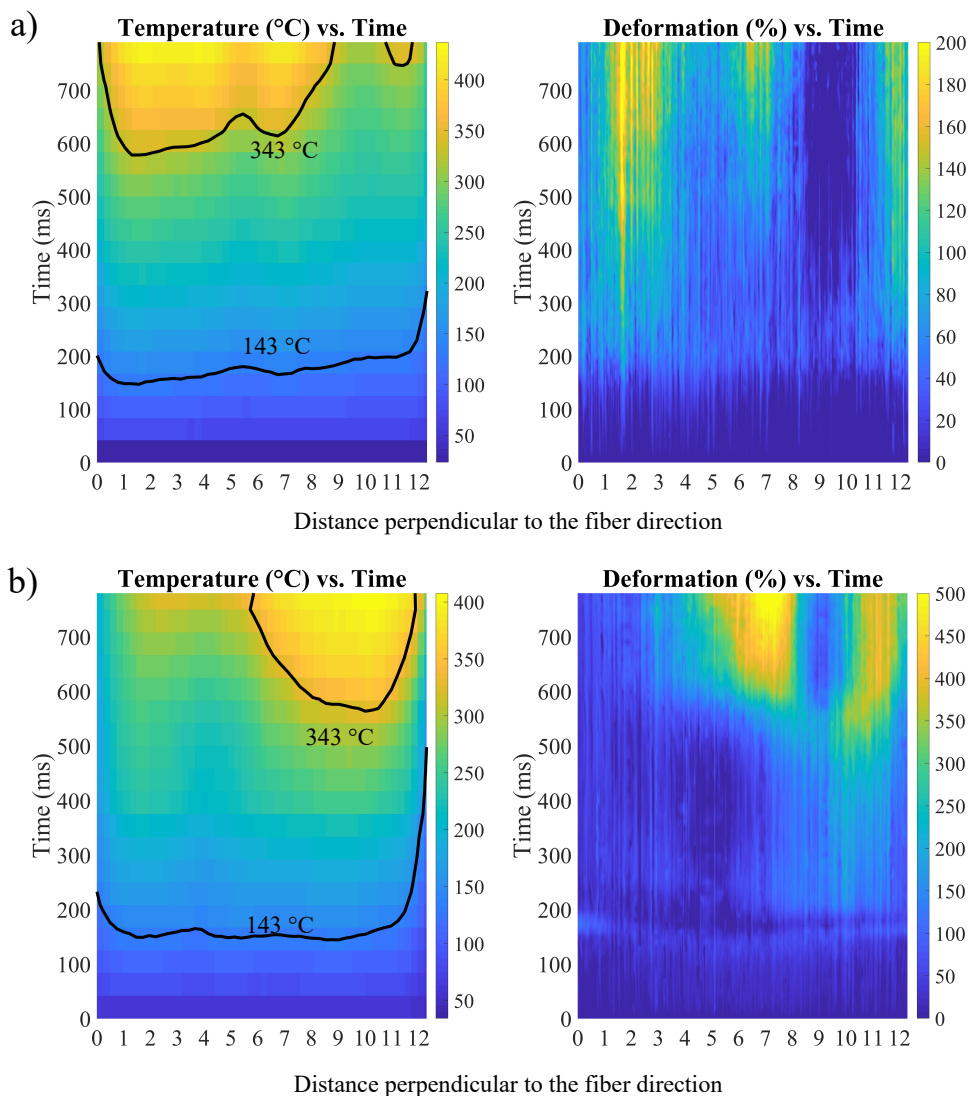


Figure 3.8. Representative synchronized temperature and out of plane deformation plots at the measurement line. The data is from experiments with long heating time (0.8 s) and a) small heated length (30 mm), b) large heated length (80 mm). The moments when T_m (343 °C) and T_g (143 °C) of PEEK are reached are marked on the temperature plots. The difference in the scales of the deformation plots is to be noted.

of heating time was statistically insignificant ($p=0.7885$). The effect of the heated length can also be observed from the deformation plots in Figure 3.8. The tape heated with the 30 mm heated length (Figure 3.8a) deformed much less than the tape heated with the 80 mm heated length (Figure 3.8b).

3.3.3 Arc-length width at the nip point

Table 3.3 shows the change in the arc-length width of the tape at the nip point state. Laser heating increased the arc-length width of the tape between 1.4 % (30 mm heated length, 0.8 s heating time) and 5.5 % (80 mm heated length, 0.2 s heating time) of the arc-length width of the tape before heating. The arc-length width increased more as the heated length was increased from 30 mm to 80 mm (120 % and 179 % for the heating times of 0.2 and 0.8 s, respectively.) or the heating time was decreased from 0.8 s to 0.2 s (21 % and 19 % for the heated lengths of 30 and 80 mm, respectively.), keeping the other heating parameter fixed. Table 3.5 statistically demonstrates the effects of heating time and heated length on arc-length width of the tape at the nip point state. Both the heated length ($p=0.0000$) and the heating time ($p=0.0002$) had a significant effect on arc-length width increase.

3.3.4 Ex-situ measurements

Figure 3.6 shows a typical cross-section of a deconsolidated specimen after cooling to room temperature. It can be seen that the surface roughness, void content and thickness differed locally along the width of the tape. Table 3.4 presents the effects of heating time and heated length on surface roughness, thickness increase and void content after the tape cools down to the room temperature. Table 3.5 shows the results of ANOVA on the influence of the heating parameters on the ex-situ measurements.

Laser heating led to an increase in the RMS surface roughness for all heating times and heated lengths. The lowest RMS roughness was observed for 30 mm heated length and 0.2 s heating time (252 % increase). The highest RMS roughness was observed for 80 mm heated length and 0.8 s heating time (712 % increase). Both heating parameters had a statistically significant effect on the surface roughness according to ANOVA ($p=0.0000$ and 0.0000 for heated length and heating time, respectively). Also, the interaction term was statistically significant ($p=0.0000$). Examining the mean values in Table 3.4, the interaction term implies that increasing the heating time had a much weaker effect on the RMS roughness for the heated length of 30 mm (7 % increase) compared to its effect for the heated length of 80 mm (75 % increase).

After the heating-cooling cycle, the thickness of the tape increased between $25.6\mu\text{m}$ and $34.5\mu\text{m}$ ($\sim 20\%$) on average for all parameters. However, neither of the heating parameters had a statistically significant effect ($p=0.2285$ and $p=0.3824$ for the heated length and heating time, respectively).

All experiments resulted in an increase in void content, whose final values ranges between 3.3-4.3 % on average. However, the effects of neither of the heating parameters on the final void content ($p=0.7043$ and $p=0.3406$ for the heated length and heating time, respectively) were statistically significant.

3.4 Discussion

3.4.1 Deconsolidation mechanisms during rapid laser heating

The results of this research indicate that thermoplastic tapes deconsolidate significantly under laser heating parameters relevant to the LAFP process. Deconsolidation occurred in the form of increased out-of-plane deformation, waviness, arc-length width, roughness, thickness and volumetric void content as shown in Tables 3.3 and 3.4. The observations and literature point out to the fact that a complex and intertwined relationship is present between the deconsolidation mechanisms and forms of deconsolidation at the micro- and meso-scale. An overall picture of this relationship is shown in Figure 3.9. Given the initial tape microstructure and laser heating parameters such as the heated length and heating time (shown with the brown circle), several deconsolidation mechanisms (red rectangles) will be triggered and result in different forms of deconsolidation (blue ellipses). Since the laser heating is affected by the surface properties of the tape, surface roughness and waviness formation lead to non-uniform temperature at the surface (green rounded rectangle), which exacerbates the deconsolidation mechanisms at several locations on the tape. This creates a unique link between the forms of deconsolidation and deconsolidation mechanisms, forming the loop in Figure 3.9.

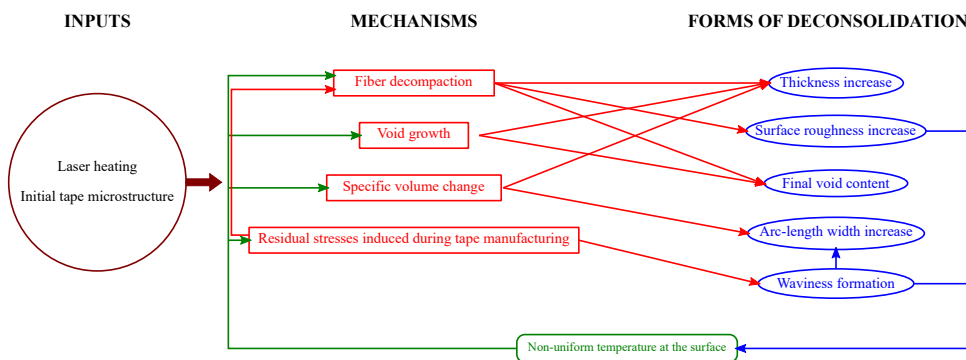


Figure 3.9. Deconsolidation mechanisms and the measured forms of deconsolidation during rapid laser heating.

Fiber decompaction

The first of these phenomena is fiber decompaction, which is demonstrated in Figure 3.6. It can be observed that fibers do not decompact uniformly along the width of the tape. This can be explained by the local fiber volume fraction near the surface of the as-received tape and softening of the surrounding resin above the glass transition temperature. It has been demonstrated that the incident laser energy on a thermoplastic tape is primarily absorbed by the fibers, as PEEK is practically transparent to laser sources in the wavelength range of 500-2000 nm [38]. The heat is then dissipated to the resin via conduction. The storage modulus of PEEK decreases more than ten-fold above

the glass transition temperature [39, 40]. This allows the fibers at the surface to move due to the micro-scale residual stresses introduced during tape manufacturing. During the heating experiments, fibers on the surface are thought to absorb the laser energy locally at the areas with a high local fiber volume fraction, soften the resin in their immediate vicinity and decompact.

Fiber decompaction contributed to three forms of deconsolidation: thickness increase, surface roughness increase and final void content. Thickness increase is an obvious outcome of fiber decompaction, as the fibers move in the out-of plane direction. Decompacked fibers increase the surface roughness as well, as there is a correlation between the thickness of the layer with dry fibers at the surface and surface roughness [21]. Moreover, there is an interesting relationship between the fiber decompaction and final void content. Figure 3.6 shows that not all the voids are within the tape but some are close to the tape surface where fiber decompaction can be observed. Therefore, it can be concluded that the cavities formed by the motion of fiber bundles at the surface also play a major role in void formation during rapid laser heating. A similar phenomenon has already been observed during the re-heating of pre-consolidated composite laminates [14].

Void growth

Void growth is a source of thickness increase of the tape at the nip point. It also determines the final void content in combination with the void formation due to fiber decompaction. The upper bound for void growth due to thermal expansion of air can be calculated by the ideal gas law if the elastic modulus and surface tension of the polymer melt are neglected [14]:

$$V_g(T) = \left(\frac{p_g^0}{p_0} \right) \left(\frac{T}{T_0} \right) V_g^0 \quad (3.1)$$

where V_g^0 , T_0 and p_g^0 are the initial average void volume, temperature and pressure, respectively. p_0 is the atmospheric pressure. Assuming $T_0 = 293 \text{ K}$ (20°C), $T = 633 \text{ K}$ (360°C) and $p_g^0 = p_0$, Equation (3.1) yields

$$V_g = 2.16 V_g^0 \quad (3.2)$$

Given an initial void content of 0.71 % (Table 3.1), this results in a void content of $\sim 1.5\%$ if the volume of the tape is assumed to stay constant (which is another conservative assumption since the volume of the whole tape also increases during heating, which would lead to a lower volumetric void percentage). This value is significantly lower than the final void content of the deconsolidated tapes given in Table 3.4 (3-4 %), meaning that other sources of void formation must take part. It was recently shown that dissolved moisture is not a major source of deconsolidation for blanks manufactured with LAFP [13]. Voids due to fiber traction are thought to be the source of the remaining final void content.

Specific volume change

During laser heating, the increasing specific volume of PEEK contributes to thickness and arc-length width increase. Figure 3.10 shows the temperature dependent specific volume of PEEK under ambient pressure, reproduced from the work of Zoller et al. [41]. The specific volume of PEEK at room temperature is $0.764 \text{ cm}^3/\text{g}$. Below T_g , the specific volume increases linearly with a rate of $1.2 \times 10^{-4} \text{ cm}^3/\text{g}^\circ\text{C}$. Between T_g and T_m , the specific volume increases in a linear fashion up to 320°C with a rate higher than the rate below T_g ($3.5 \times 10^{-4} \text{ cm}^3/\text{g}^\circ\text{C}$). However, as the temperature approaches T_m , a sudden increase is observed in the specific volume, which can be explained by melting of the crystalline phase of the polymer. Above T_m , the specific volume increases linearly with a rate of $6.1 \times 10^{-4} \text{ cm}^3/\text{g}^\circ\text{C}$. From a qualitative perspective, this behavior resembles with the OP deformation patterns demonstrated in Figure 3.8: a steady increase past the T_g and a sharp increase as the temperature approaches T_m is common for both the OP deformation and specific volume of PEEK.

The importance of the specific volume increase of PEEK for tape deformation can be assessed by the theoretical volume increase. According to Figure 3.10, the specific volume of PEEK increases by 17.2 % at T_m . Assuming that the change of the volume of the carbon fibers is negligible, an equivalent volume increase of 7 % is expected for a tape with a resin volume ratio of 41 %. The boundary between the solid and molten parts of the tape restricts the movement of PEEK in the longitudinal direction of the tape; so the specific volume change is expected to increase the width and thickness of the tape in the cross-sectional plane perpendicular to the fiber direction. Therefore, the changes in the cross-sectional area of the tape can be used to estimate the volume change. Using the thickness increase from Table 3.4 and arc-width length increase from Table 3.3, it can be calculated that the volume change of the tape is between 21-24 %. The comparison of the theoretical estimation and experimental data shows that the specific volume increase of PEEK plays a significant role in the deformation of the tape but there should also be other factors which contribute to tape deformation. This confirms the role of fiber decompaction and void growth in the increase in thickness and hence in volume.

Thermal expansion

The thermal expansion in the transverse directions of the tape is relevant for two forms of deconsolidation: arc-length width and thickness increase. Typical CTE values for the CF/PEEK tape and its constituents are given in Table 3.6. At all temperature levels, the longitudinal CTE of the tape is dominated by the fibers (which have a very small CTE in the longitudinal direction) and the tape can be treated as inextensible in this direction. However, it can be seen that the CTE of PEEK changes drastically as the tape is heated and this is reflected in the transverse CTE of the tape. Therefore, an expansion in the transverse directions can be expected.

Above the melting temperature, the initial tape width of $\sim 12.6 \text{ mm}$ (Table 3.1) and transverse CTE of $85 \times 10^{-6}/^\circ\text{C}$ (Table 3.6) results in a width increase of $1 \mu\text{m}$. In the thickness direction, a sub-micron increase is expected due to thermal expansion since the initial thickness is 0.15 mm . These values are negligible compared to the order of magnitude of the deformations in the tape. Therefore, it can be stated that thermal ex-

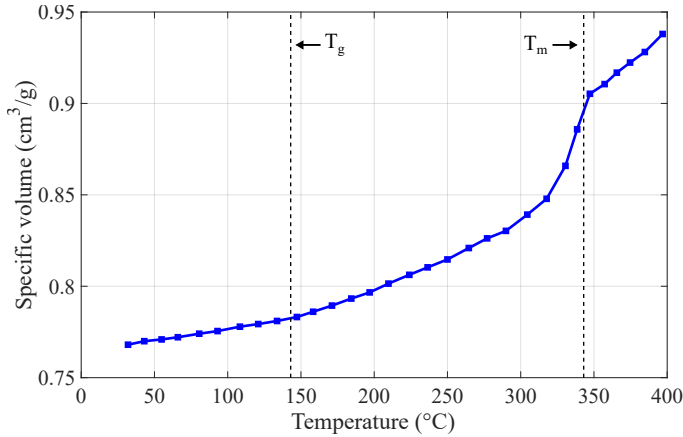


Figure 3.10. Temperature dependent specific volume of PEEK at ambient pressure, obtained from isothermal measurements at each temperature. Reproduced from Zoller et al. [41].

Table 3.6. Typical coefficients of thermal expansion ($10^{-6}/^{\circ}\text{C}$) of CF/PEEK and its constituents.

Material	Below T_g	Between T_g and T_m	Above T_m
CF-longitudinal	-1.2 – -0.5* [42, 43]	0.5* [43]	1.1* [43]
CF-transverse	4.0* – 12.0 [42, 43]	5.5* [43]	6.8* [43]
PEEK	50.0 – 70.0 [44, 45]	Increases up to 250 [45]	No data available
CF/PEEK-longitudinal	0.4 [46]	0.0 [†] [46]	0.0 [†] [42]
CF/PEEK-transverse	30.0 [46]	80.0 [†] [46]	85.0 [†] [42]

* Calculated using PAN-based HTA 5131 carbon fiber data

[†] Estimated values

pansion does not play a significant role in deconsolidation of the thermoplastic tapes slit in narrow widths and it was excluded from the mechanisms in Figure 3.9.

Residual stresses induced during tape manufacturing

The release of residual stresses in the thermoplastic tape is relevant to two forms of deconsolidation: increased surface roughness due to fiber decompaction in the micro-scale and waviness formation in the meso-scale. These stresses are introduced to the thermoplastic tape during the production process when individual fibers or fiber bundles are stretched, compressed or bent, and subsequently locked upon the solidification of the resin [13]. When the surface of the material reaches T_g , only individual fibers can decompact at the surface since the majority of the resin is in solid state beneath the tape surface. This leads to deformations at the scale of a fraction of the initial thickness of the tape as shown in Figure 3.8. However, when more resin content softens as the heating continues, motion of larger fiber bundles are enabled. This results in deformations in the order of multiple initial tape thicknesses in the out-of-plane direction, which cannot be explained by other mechanisms of deconsolidation discussed in the previous sections.

Non-uniform temperature at the surface

Rapid laser heating is unique in the sense that the forms of deconsolidation and deconsolidation mechanisms are linked to each other via the non-uniform temperature at the surface, as demonstrated in Figure 3.9. Therefore, the relationship between tape deformation and non-uniform temperature is very important. Figure 3.8 demonstrates that the temperature profile and the deformation of the tape followed similar patterns. Also, T_g and T_m mark important points for the non-uniformity of temperature and deformation of the tape.

The initiation of the temperature non-uniformity can be explained by fiber decompaction, which starts around T_g as a result of the reduction in the storage modulus of the resin. As the decompacted fibers moved closer to the laser source, the local heat flux on them increased. This led to an increase in local temperature and further softening of the resin accompanied with more decompaction of fibers.

While the temperature non-uniformity was initiated by fiber decompaction, it was succeeded by waviness formation. This led to even larger variations in tape temperature due to changing angle of incidence at the peaks and valleys formed on the surface. At the beginning of the heating process up to T_g , the coefficient of variation of the temperature along the width of the specimens was on the order of $\sim 1\%$. This value is similar to the calculations presented in the work of Yan et al. [47]. They claimed that on the surface of a thin composite layer with uniform fiber distribution, temperature variation due to the absorption rate difference between the fibers and resin is 0.5% . However, as the specimen reached T_m during the experiments presented in this paper, the coefficient of variation of the temperature along the width raised up to 50% .

The importance of the unique link between the heating and tape deformation mechanisms becomes clearer when the results in this work are compared with the behavior during hot plate heating of the same CF/PEEK material [19], where heat is transferred via conduction between the hot plate and composite. Contrary to laser heating, waviness

formation was reported only in the cooling stage and not in the heating stage during deconsolidation with a hot plate. This shows that the mode of heating plays a significant role and deconsolidation should be investigated specifically for the heating device of interest.

3.4.2 Relevance to LAFP process

Different forms of deconsolidation affect a number of aspects during the LAFP process. The increase in fiber decompaction induced surface roughness is important for bond strength development at the interface since resin must flow through dry fiber bundles to create effective intimate contact [10]. More dry fibers at the tape surface would hinder effective intimate contact development. The RMS roughness results in Table 3.4 show that the heating strategies that would result in less dry fibers at the surface are reducing the heated length of the tape or increasing the placement speed provided that the nip point temperature is kept fixed. This observation is positive for the industry, as higher placement speeds are expected to result in less dry fibers at the tape surface at the nip point.

The thickness at the nip point influences void compaction and heat transfer during the LAFP process. Void consolidation models such as the ones from Pitchumani et al. [6] and Simacek et al. [16] use the thickness at the nip point (and the subsequent momentary thickness during compaction) to calculate the pressure distribution within the composite material under the compaction roller. Also, as explained in the previous sections and shown in Figure 3.6, void growth and fiber decompaction play an important role in the change in tape thickness. Since these mechanisms are local and are not typically observed at every location along the tape width, the tape thickness increases non-uniformly at the nip point regardless of the heating strategy. This might cause non-uniform pressure distribution at the tape surfaces which are in contact with the compaction roller and the underlying substrate. The thickness increase and non-uniform contact should be incorporated to tape consolidation models to find the final void content of the fiber placed structures more accurately. The thickness increase at the nip point is also important for the through-thickness temperature distribution as the dominating heat transfer mechanism is internal conduction [24]; therefore, it should be considered in the heat transfer models.

Waviness formation at the nip point has potential consequences on mechanical aspects such as non-uniform pressure distribution under the compaction roller, more entrapped air at the interfaces and deviation of the fiber orientation from the design in the thickness direction of the part. In addition, optical-thermal phenomena may be affected by the waviness at the nip point, as the reflection of the laser beams in the cavity formed near the nip point is closely linked to the geometry of the tape and substrate surfaces [38, 48]. This would eventually affect the temperature distribution and increase the non-uniformity along the width. The heated length is the predominant factor for the maximum amplitude of the waviness at the nip point as shown in Table 3.3 and Table 3.5. This would mean that increasing the heated length of the tape by aiming the laser more towards the tape or activating more emitters would result in more waviness formation. The studies from Grouve et al. [22] and Di Francesco et al. [49] showed that

increasing the heated length of the tape led to increased fracture toughness and degree of intimate contact, respectively. This implies that increased waviness during the heating phase may not necessarily affect bond formation. The compaction behavior of deconsolidated tapes should be investigated in further detail to completely understand bond strength development during LAFP.

Tape width after placement is an important factor for LAFP due to its effects on gaps/overlaps in the final laminate. It has been traditionally explained with squeeze flow of the tape under the compaction roller [2]. Dimensional changes in the tape during the heating phase have been neglected so far. The experimental results presented in [50] show that a single CF/PEEK tape placed on an 8-layer cross-ply laminate widens by 8-10 % for a nip point temperature between 350-400 °C, with little dependency on the applied compaction force. The limited effect of the compaction force on tape widening suggests that the heating phase of the process plays a significant role for the final tape width. The results of this study confirm this hypothesis, as the arc-length width of the tapes increased significantly (up to 5.5 %) at the nip point state. When Table 3.3 is investigated, it can be seen that the arc-length width and the maximum amplitude of the waviness show a correlation (both increase with increasing heated length and decreasing heating time). This implies that the arc-length width can be heavily influenced by the waviness formation, which can also be seen in Figure 3.3.

Table 3.3 showed that the heated length and heating time had a positive and negative correlation with the arc-length width of the tape at the nip point, respectively. An interesting outcome is that the heated length and laser power should be continuously optimized to keep the tape width at the nip point fixed for the applications where the placement speed varies, such as helical tape winding [51]. Besides, to accurately predict the final tape geometry, not only the squeeze flow under the roller but also the tape deformation before consolidation should be calculated. Kok [50] took a step in that direction by proposing a model based on quasi-static tape spreading. However, there is still room for improvement as the effects of tape warpage and heating time were not accounted for.

The results presented in this work point out to important phenomena for the heating phase of LAFP; however, additional aspects should be considered for a complete assessment of the final part quality. Firstly, the effects of laser illumination on the substrate should be investigated, as the effect of laminate thickness on deconsolidation is not known. Also, residual stresses in the substrate due to local heating and compaction might influence the deconsolidation behavior of the substrate. Another factor that might possibly affect the deconsolidation of the incoming tape is the tape tension. In this work, the tapes were fixed to the tool with polyimide films without tension application. Even though the LAFP systems usually run on low tape tension to enable layup of complex geometries [52, 53], the effect of tape tension on deconsolidation has not been clearly demonstrated. The authors are investigating this effect in a separate research project. The role of the applied compaction pressure on reducing the effects of deconsolidation has also been identified as a topic for future research. Finally, being out of the scope of this study, residual stress build-up [54] and non-optimum crystallinity levels [55] remain as important challenges to the improvement of the final quality of the in-situ consolidated structures.

3.5 Conclusion

In this study, the effect of rapid laser heating, which is typical to the heating phase of LAFP, on the micro- and meso-structure of the thermoplastic tape was investigated. Thermoplastic tapes were heated with different heated lengths (30 and 80 mm) and heating times (0.2 and 0.8 s) in a dedicated experimental setup. Meso-scale changes in the tape during laser heating were monitored in-situ via temperature and surface profile measurements. Surface roughness measurements with a confocal microscope and cross-sectional images taken with an optical microscope were used to gain additional insight into the effects of laser heating at micro-scale.

All of the experiments in this study caused significant changes in the micro- and meso-structure of the tape. These changes are in the form of increased out-of-plane deformation, waviness, arc-length width, roughness, thickness and volumetric void content. It was found that heated length was a significant factor for waviness formation, arc-length width and surface roughness. Heating time had a statistically significant influence on the arc-length width and surface roughness, the latter being only for the large heated length.

As revealed in this work, deconsolidation of the tape during laser heating is influenced by a unique phenomenon: the correlation between the temperature distribution on the tape surface and the peaks and valleys of the surface profile. Increased surface roughness and waviness result in non-uniform temperature at the surface due to varying angle of incidence. As a result of non-uniform temperature, deconsolidation is exacerbated locally. It was also proposed that deconsolidation of the tape during laser heating is a result of multiple mechanisms. Fiber decompaction plays a role in thickness and surface roughness increase. It also creates cavities near the tape surface and contributes to the final void content. Thermal expansion of voids is a partial reason for the final void content and thickness increase. Specific volume change causes an increase in the thickness and the arc-length width. Residual stresses induced during tape manufacturing is a source of waviness formation, which is also a significant contributor to the arc-length width increase.

Based on the results, the following conclusions can be derived for the LAFP process. Higher placement speeds are expected to reduce the amount of decompacted fibers at the tape surface at the nip point, which is beneficial for effective intimate contact development. In order to keep the width of the tape at the nip point constant during a process where the placement speed is variable, the heated length and laser power should be continuously optimized. Heating a larger portion of the tape would lead to more waviness formation, which causes non-uniform temperature at the tape surface and may result in non-uniform pressure distribution under the compaction roller. Increased thickness at the nip point should be considered to calculate void compaction and heat transfer during the process accurately. For future work, it is suggested that the effects of the heating phase are further quantified using constitutive models and implemented in numerical models developed for the analysis of the LAFP process.

References

- [1] Roux, M., Eguémann, N., Dransfeld, C., Thiébaud, F., Perreux, D.. Thermoplastic carbon fibre-reinforced polymer recycling with electrodynamic fragmentation: From cradle to cradle. *Journal of Thermoplastic Composite Materials* 2017;30(3):381–403.
- [2] Ranganathan, S., Advani, S.G., Lamontia, M.A.. A Non-Isothermal Process Model for Consolidation and Void Reduction During In-Situ Tow Placement of Thermoplastic Composites. *Journal of Composite Materials* 1995;29:1040–1062.
- [3] Lee, W.I., Springer, G.S.. A Model of the Manufacturing Process of Thermoplastic Matrix Composites. *Journal of Composite Materials* 1987;21(11):1017–1055.
- [4] Mantell, S.C., Springer, G.S.. Manufacturing Process Models for Thermoplastic Composites. *Journal of Composite Materials* 1992;26(16):2348–2377.
- [5] Yang, F., Pitchumani, R.. A fractal Cantor set based description of interlaminar contact evolution during thermoplastic composites processing. *Journal of Materials Science* 2001;36(19):4661–4671.
- [6] Pitchumani, R., Ranganathan, S., Don, R.C., Gillespie, J.W., Lamontia, M.A.. Analysis of Transport Phenomena Governing Interfacial Bonding and Void Dynamics During Thermoplastic Tow-placement. *International Journal of Heat and Mass Transfer* 1996;39(9):1883–1897.
- [7] Levy, A., Heider, D., Tierney, J., Gillespie, J.W., Lefebure, P., Lang, D.. Simulation and optimization of the thermoplastic Automated Tape Placement (ATP) process. *SAMPE* 2012 - Baltimore 2012;(January):15p.
- [8] Stokes-Griffin, C.M., Compston, P.. Investigation of sub-melt temperature bonding of carbon-fibre/PEEK in an automated laser tape placement process. *Composites Part A: Applied Science and Manufacturing* 2016;84:17–25.
- [9] Leon, A., Argerich, C., Barasinski, A., Soccard, E., Chinesta, E.. Effects of material and process parameters on in-situ consolidation. *International Journal of Material Forming* 2019;12(4):491–503.
- [10] Çelik, O., Peeters, D., Dransfeld, C., Teuwen, J.. Intimate contact development during laser assisted fiber placement: Microstructure and effect of process parameters. *Composites Part A: Applied Science and Manufacturing* 2020;134.
- [11] Henninger, F., Ye, L., Friedrich, K.. Deconsolidation behaviour of glass fibre-polyamide 12 composite sheet material during post-processing. *Plastics, Rubber and Composites Processing and Applications* 1998;27(6):287–292.
- [12] Shi, H., Villegas, I.F., Bersee, H.E.. Analysis of void formation in thermoplastic composites during resistance welding. *Journal of Thermoplastic Composite Materials* 2017;30(12):1654–1674.

- [13] Slange, T.K., Warnet, L.L., Grouve, W.J.B., Akkerman, R.. Deconsolidation of C/PEEK blanks: on the role of prepreg, blank manufacturing method and conditioning. *Composites Part A: Applied Science and Manufacturing* 2018;113:189–199.
- [14] Ye, L., Lu, M., Mai, Y.W.. Thermal de-consolidation of thermoplastic matrix composites-I. Growth of voids. *Composites Science and Technology* 2002;62(16):2121–2130.
- [15] Lu, M., Ye, L., Mai, Y.W.. Thermal de-consolidation of thermoplastic matrix composites-II. "Migration" of voids and "re-consolidation". *Composites Science and Technology* 2004;64(2):191–202.
- [16] Simacek, P., Advani, S.G., Gruber, M.B., Jensen, B.. A non-local void filling model to describe its dynamics during processing thermoplastic composites. *Composites Part A: Applied Science and Manufacturing* 2013;46(1):154–165.
- [17] Wolfrath, J., Michaud, V., Manson, J.A.. Deconsolidation in glass mat thermoplastic composites: Analysis of the mechanisms. *Composites Part A: Applied Science and Manufacturing* 2005;36(12):1608–1616.
- [18] Brzeski, M.. Experimental and Analytical Investigation of Deconsolidation for Fiber Reinforced Thermoplastic Composites. Ph.D. thesis; Technischen Universität Kaiserslautern; 2014.
- [19] Krämer, E.T., Grouve, W.J.B., Koussios, S., Warnet, L.L., Akkerman, R.. Real-time observation of waviness formation during C/PEEK consolidation. *Composites Part A: Applied Science and Manufacturing* 2020;133:105872.
- [20] Kok, T., Grouve, W.J.B., Warnet, L.L., Akkerman, R.. Intimate Contact Development in Laser Assisted Fiber Placement. *ECCM17 - 17th European Conference on Composite Materials* 2016;1(June):26–30.
- [21] Kok, T., Grouve, W.J.B., Warnet, L.L., Akkerman, R.. Quantification of Tape Deconsolidation During Laser Assisted Fiber Placement. *Automated Composites Manufacturing: Third International Symposium* 2017;.
- [22] Grouve, W.J.B., Warnet, L.L., Rietman, B., Visser, H.A., Akkerman, R.. Optimization of the tape placement process parameters for carbon-PPS composites. *Composites Part A: Applied Science and Manufacturing* 2013;50:44–53.
- [23] Stokes-Griffin, C.M., Compston, P.. An inverse model for optimisation of laser heat flux distributions in an automated laser tape placement process for carbon-fibre/PEEK. *Composites Part A: Applied Science and Manufacturing* 2016;88:190–197.
- [24] Weiler, T., Emonts, M., Wollenburg, L., Janssen, H.. Transient thermal analysis of laser-assisted thermoplastic tape placement at high process speeds by use of analytical solutions. *Journal of Thermoplastic Composite Materials* 2018;31(3):311–338.

- [25] Stokes-Griffin, C.M., Compston, P. The effect of processing temperature and placement rate on the short beam strength of carbon fibre-PEEK manufactured using a laser tape placement process. *Composites Part A: Applied Science and Manufacturing* 2015;78:274–283.
- [26] Philips Photonics GmbH, . Laser System with Laser Module PPM412-12-980-24 with Driver Unit PPU104-12 Reference and Installation Manual Version 1.1. Tech. Rep.; 2017.
- [27] Micro-Epsilon, . Operating Instructions scanCONTROL 29xx. Tech. Rep.; 2018.
- [28] Composites, T.A.. TenCate Cetex® TC1200 PEEK Resin System Product Data Sheet 2017;.
- [29] Hosseini, S.M., Baran, I., van Drongelen, M., Akkerman, R.. On the temperature evolution during continuous laser-assisted tape winding of multiple C/PEEK layers: The effect of roller deformation. *International Journal of Material Forming* 2020;;1–19.
- [30] Stokes-Griffin, C.M., Compston, P. A combined optical-thermal model for near-infrared laser heating of thermoplastic composites in an automated tape placement process. *Composites Part A: Applied Science and Manufacturing* 2015;75:104–115.
- [31] International Organization for Standardization, . ISO 16610-21 Geometrical product specifications (GPS)- Filtration-Part 21: Linear profile filters: Gaussian filters. 2011.
- [32] International Organization for Standardization, . ISO 4288:1996 Geometrical Product Specifications (GPS) - Surface texture: Profile method - Rules and procedures for the assessment of surface texture. 1996.
- [33] ASTM E1933 - 14 (2014), . Standard Practice for Measuring and Compensating for Emissivity Using Infrared Imaging Radiometers. 2014.
- [34] Çelik, O., Hosseini, S.M.A., Baran, I., Grouve, W.J.B., Akkerman, R., Peeters, M.J., et al. The influence of inter-laminar thermal contact resistance on the cooling of material during laser assisted fiber placement 2021;145(March).
- [35] The MathWorks Inc, . MATLAB and Statistics Toolbox Release 2017b. 2017.
- [36] Thor, M., Sause, M.G.R., Hinterhölzl, R.M.. Mechanisms of Origin and Classification of Out-of-Plane Fiber Waviness in Composite Materials—A Review. *Journal of Composites Science* 2020;4(3):130.
- [37] Weiler, T. Thermal Skin Effect in Laser-Assisted Tape Placement of Thermoplastic Composites. Ph.D. thesis; 2019.
- [38] Stokes-Griffin, C.M., Compston, P. Optical characterisation and modelling for oblique near-infrared laser heating of carbon fibre reinforced thermoplastic composites. *Optics and Lasers in Engineering* 2015;72:1–11.

- [39] Zheng, B., Gao, X., Li, M., Deng, T., Huang, Z., Zhou, H., et al. Formability and failure mechanisms of woven CF/PEEK composite sheet in solid-state thermoforming. *Polymers* 2019;11(6).
- [40] Yurchenko, M.E., Huang, J., Robisson, A., McKinley, G.H., Hammond, P.T.. Synthesis, mechanical properties and chemical/solvent resistance of crosslinked poly(aryl-ether-ether-ketones) at high temperatures. *Polymer* 2010;51(9):1914–1920.
- [41] Zoller, P., Kehl, T.A., Starkweather Jr., H.W., Jones, G.A.. The Equation of State and Heat of Fusion of Poly(ether ether ketone). *Journal of Polymer Science: Part B: Polymer Physics* 1989;27:993–1007.
- [42] Cogswell, F.N.. Thermoplastic aromatic polymer composites: a study of the structure, processing, and properties of carbon fibre reinforced polyetheretherketone and related materials. Butterworth-Heinemann; 1992.
- [43] Pradere, C., Sauder, C.. Transverse and longitudinal coefficient of thermal expansion of carbon fibers at high temperatures (300–2500 K). *Carbon* 2008;46(14):1874–1884.
- [44] Barnes, J.A., Simms, I.J., Farrow, G.J., Jackson, D., Wostenholm, G., Yates, B.. Thermal Expansion Behaviour of Thermoplastic Composite Materials. *Journal of Thermoplastic Composite Materials* 1990;3(1):66–80.
- [45] Lu, S.X., Cebet, P. Thermal stability and thermal expansion studies of PEEK and related polyimides. *Polymer* 1996;37(14):2999–3009.
- [46] Cogswell, F.N.. The experience of thermoplastic structural composites during processing. *Composites Manufacturing* 1991;2(3-4):208–216.
- [47] Yan, H., Du, T.j., Peng, G.L.. Meso-scale simulation of temperature field in composite materials under laser irradiation. In: Ding, Y., Feng, G., Hoffmann, D.H.H., Cao, J., Lu, Y., editors. Fourth International Symposium on Laser Interaction with Matter; vol. 10173. International Society for Optics and Photonics; 2017, p. 101730K.
- [48] Hosseini, S.M.A., Schäkel, M., Baran, I., Janssen, H., van Drongelen, M., Akkerman, R.. A new global kinematic-optical-thermal process model for laser-assisted tape winding with an application to helical-wound pressure vessel. *Materials & Design* 2020;193:108854.
- [49] Di Francesco, M., Giddings, P.F., Scott, M., Goodman, E., Dell'Anno, G., Potter, K.. Influence of laser power density on the meso-structure of thermoplastic composite preforms manufactured by Automated Fibre Placement. In: SAMPE Long Beach 2016; vol. 53. ISBN 9788578110796; 2016, p. 1689–1699. arXiv:arXiv:1011.1669v3.
- [50] Kok, T.. On the consolidation quality in laser assisted fiber placement: the role of the heating phase. Phd thesis; University of Twente; 2018.

- [51] Hosseini, S.M.A., Schäkel, M., Baran, I., Janssen, H., van Drongelen, M., Akkerman, R.. A new global kinematic-optical-thermal process model for laser-assisted tape winding with an application to helical-wound pressure vessel. *Materials and Design* 2020;193.
- [52] Lukaszewicz, D.H., Ward, C., Potter, K.D.. The engineering aspects of automated prepreg layup: History, present and future. *Composites Part B: Engineering* 2012;43(3):997–1009.
- [53] Frketic, J., Dickens, T., Ramakrishnan, S.. Automated manufacturing and processing of fiber-reinforced polymer (FRP) composites: An additive review of contemporary and modern techniques for advanced materials manufacturing. *Additive Manufacturing* 2017;14:69–86.
- [54] Dedieu, C., Barasinski, A., Chinesta, E., Dupillier, J.M.. On the prediction of residual stresses in automated tape placement. *International Journal of Material Forming* 2017;10(4):633–640.
- [55] Comer, A.J., Ray, D., Obande, W.O., Jones, D., Lyons, J., Rosca, I., et al. Mechanical characterisation of carbon fibre-PEEK manufactured by laser-assisted automated-tape-placement and autoclave. *Composites Part A: Applied Science and Manufacturing* 2015;69:10–20.

Chapter 4

Intimate Contact Development During Laser Assisted Fiber Placement: Microstructure and Effect of Process Parameters

Intimate contact development under LAFP-specific thermal and mechanical boundary conditions/interactions and the effect of process parameters are investigated. One-layer, unidirectional strips of CF/PEKK material were placed with different process parameters on a flat tool surface to create different intimate contact conditions. The concept of effective intimate contact, which is based on the resin content at the surface, is introduced and a methodology to measure it from surface micrographs is provided. Degree of effective intimate contact measured from the samples was compared with the existing intimate contact models. The temperature history in the compaction zone was estimated with a finite element model and pressure sensitive films were used to determine the compaction pressure. It is shown that in addition to the squeeze flow mechanism, which is the base for the current intimate contact models, through-thickness percolation flow of the resin needs to be considered to explain the effective intimate contact development.

This chapter is based on: Çelik, O., Peeters, D., Dransfeld, C., Teuwen, J., Intimate contact development during laser-assisted fiber placement: Microstructure and effect of process parameters. Composites Part A: Applied Science and Manufacturing, 105888, Volume 134, 2020.

4.1 Introduction

Thermoplastic composites (TPC) have drawn significant interest in the aerospace industry for their infinite shelf life, high fracture toughness, chemical and solvent resistance, weldability and recyclability [1–3]. Automated fiber placement (AFP) has become a promising manufacturing solution for TPC, providing reduction in labor time per component, lower material scrap rates and higher repeatability [4]. In modern laser assisted fiber placement (LAFP) systems, a laminate is built by heating the surface of the tape and substrate with a laser heat source pointed towards the nip point and compacting with a flexible roller as shown in Figure 4.1.

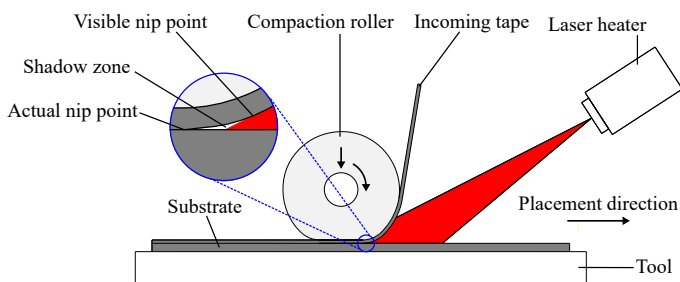


Figure 4.1. Working principle of LAFP systems.

Due to the re-melting capability of thermoplastic polymers, in-situ consolidated (i.e., without a post-consolidation step in an autoclave, oven or press) structures can be manufactured with the LAFP process. This aspect of the technology is especially appealing since significant capital investment and operating costs related to post-consolidation can be saved if sufficient part quality with a feasible processing speed is achieved. In order to achieve this goal, extensive research has been conducted in the last decades to understand the mechanisms which play a role at the heating, compaction and cooling phases of the process [5–14].

The compaction phase is especially critical since two subsequent plies consolidate only with the pressure supplied by the compaction roller. Intimate contact development is the first step of consolidation and affects several aspects during the process which significantly influence the properties of the final structure. Firstly, bond strength formation between subsequent plies requires intimate contact development between surfaces. Bonding is driven by diffusion and entanglement of polymer molecules across the interface through reptation [15]. This mechanism is active only at the locations which are in intimate contact [16]. Secondly, inter-laminar void content in the final structure is a direct result of intimate contact development. Such voids act as crack initiation points and reduce the mechanical performance of the final product, especially inter-laminar shear, compression and transverse tensile strength and fatigue life [17]. Finally, heat transfer might be reduced at the ply interfaces due to incomplete intimate contact [10, 18]. The effect of reduced heat transfer on the temperature history influences all temperature related phenomena during LAFP, e.g. crystallinity, healing, void compaction/decompaction and residual stresses. Understanding how intimate contact de-

velops during LAFP is therefore an important step for linking the process parameters to the final quality of the parts.

The common approach to explain how intimate contact develops during thermoplastic composite processing has been based on the squeeze flow of the surface asperities. Such models combine the compaction force, an idealized description of the composite surface and the temperature-dependent homogenized viscosity of the composite material to find the degree of intimate contact given the temperature and pressure history of the process. Using this approach, several models were proposed for intimate contact development. The first model was proposed by Dara and Loos for isobaric and isothermal conditions [19]. The squeeze flow mechanism was justified by the high viscosity of the thermoplastic polymers at melting temperature. They modeled the composite surface as a collection of rectangular elements with non-uniform height and width, approximated by a 2-parameter Weibull distribution. Lee and Springer [20] followed a similar rationale but simplified the surface representation with uniform rectangles. Mantell and Springer [21] extended this model for non-uniform pressures and temperatures, which is more suitable for automated fiber placement or winding. Yang and Pitchumani suggested that the asperities in the thermoplastic composite surfaces exhibit fractal characteristics and proposed a surface representation with a fractal Cantor set [22].

These models have been extensively used to predict intimate contact development for the AFP process [23–26]. However, limited prediction accuracy was reported for modern systems with laser heaters [26–28]. This raises the question of whether the squeeze flow mechanism with homogenized material assumption is completely suitable to explain intimate contact development during LAFP. Rapid heating to high processing temperatures (370–400 °C for carbon fiber reinforced polyetherketoneketone (CF/PEKK) [29] and carbon fiber reinforced polyetheretherketone (CF/PEEK) [30] tapes) without pressure application and very short compaction times (usually between 0.01–0.3 s depending on the deformation of the compaction roller and the placement speed) are distinctive features of LAFP. Moreover, heating above the melting temperature of the resin material without pressure application results in a fiber-rich and rough surface until the tape reaches the nip point [31]. Considering that a significant portion of the tapes already has a resin-poor surface in their original state such as the one shown in Figure 4.2 and the microstructure of the tape changes during the heating phase, intimate contact development might not be adequately described with the squeeze flow mechanism. Intimate contact models mentioned above were validated by press-consolidated samples with compaction times orders of magnitude higher than typical compaction times for LAFP, which might suppress the effect of non-uniform microstructure at the surface. Considering the state-of-the-art literature, how intimate contact develops at short time spans typically found in the LAFP process, taking the microstructural changes due to laser heating into account, is still an open question.

Another reason for the lack of knowledge about the mechanisms involved in intimate contact development is how the degree of intimate contact is measured. The degree of intimate contact was measured mostly at the interfaces between the plies [19, 22, 23, 32], although the available intimate contact models consider flattening of a single composite surface against a rigid surface. There is only one study where the predicted intimate con-

tact was compared with the surface of press-consolidated individual tapes [20]; however, the details of how the degree of intimate contact was measured was omitted. Moreover, the final state of the composite interface contains little information about the process of intimate contact development during compaction. Therefore, a more detailed analysis of the intimate contact development on a single tape under LAFP conditions is required.

The aim of this paper is therefore to understand the intimate contact development mechanism under LAFP-specific thermal and mechanical boundary conditions and interactions. Specifically, the following questions will be addressed: How can the degree of intimate contact be quantified considering the inhomogeneity of the composite surface? What is the effect of LAFP process parameters on intimate contact development? Can the squeeze flow mechanism fully explain the intimate contact development during LAFP?

To answer these questions, one-layer samples were prepared with a LAFP machine with different process parameters. The final degree of intimate contact of the samples was measured with a novel method which considers the non-homogeneous nature of the contact surface. Experimental findings were compared to and contrasted with the state-of-the-art intimate contact models. In order to do that, a heat transfer model of the process was formulated to estimate the temperature history of the tape in the compaction region. The estimated temperature history was then combined with the measured roller pressure and the degree of intimate contact was calculated. The results were used to present a new approach to describe the intimate contact development during LAFP.

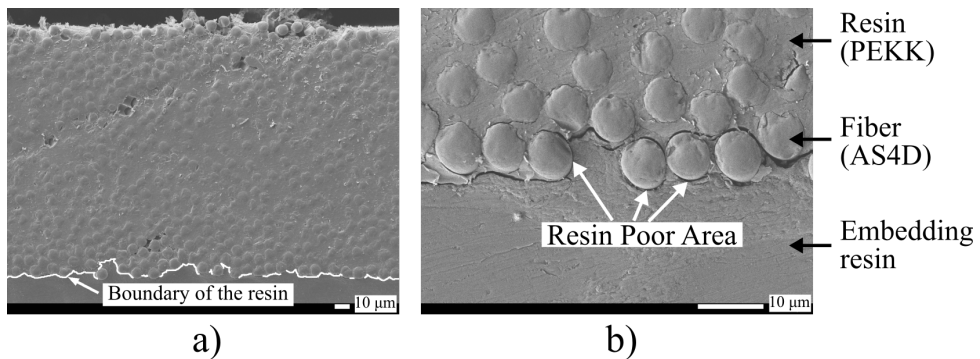


Figure 4.2. Scanning Electron Microscope images of the cross-section of the unprocessed CF/PEKK tape. a) moderate magnification (450x), resin level on the surface is indicated with a white boundary. b) high magnification (2000x), the microscopic morphology of the resin poor area is shown.

4.2 Materials and Methods

4.2.1 Fiber Placement System

Fiber placement experiments were conducted at Royal Netherlands Aerospace Center (NLR). A six-axis articulated robot on a linear axis provided by Coriolis was used. The machine was able to deliver eight 6.35 mm ($\frac{1}{4}$ in.)-wide tapes simultaneously up to 800 mm/s placement speed. The end effector was equipped with a 6 kW Laserline LDF series diode laser system and an optic lens which created a 56 mm \times 28 mm rectangular illuminated area at the 250 mm focal distance. A conformable compaction roller with 60 shore hardness and a diameter of 70 mm was installed on the machine. Figure 4.3 depicts the fiber placement system used for this study.

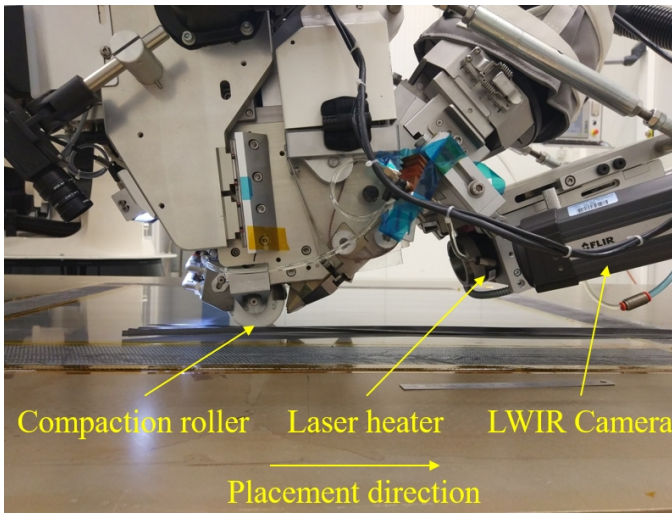


Figure 4.3. The fiber placement system used in the experiments. Courtesy of Royal Netherlands Aerospace Center (NLR).

4.2.2 Specimens for Intimate Contact Investigation

The material used in this study was TC1320-1 CF/PEKK supplied by TenCate, in $\frac{1}{4}$ in. slit tapes. Eight tapes with cross-sectional dimensions 6.35 mm \times 0.15 mm were placed next to each other simultaneously along 1000 mm long strips on a flat aluminum tool with each combination of process parameters shown in Table 4.1. The machine parameters were chosen such that they cover the range between the minimum and maximum compaction forces and placement speeds relevant to the industrial use of LAFP at processing temperatures suggested by the manufacturer [29]. The temperature of the heated tool was set to 155 °C to allow the compacted tape to cool down to below its glass transition temperature (159 °C [29]), so that the amorphous phase of the PEKK polymer stays in the glassy state and does not cause further changes in the microscopic struc-

ture after compaction. The tool surface was covered with 50 μm thick polyimide (thermalimide) film to reduce the possible effects of the scratches on the tool on the degree of intimate contact measurements. Samples were cut from the mid-section (between 400-600 mm from the beginning) of the strips so that the acceleration and deceleration phases of the placement head did not affect the microstructure.

Table 4.1. Process parameters used in the experimental study. A sample with each combination of parameters was manufactured.

Nip Point Temperature (°C)	Tool Temperature (°C)	Compaction Force (N)	Placement Speed (mm/s)
			100
380	20	100	200
400	155	400	400
		800	800

4.2.3 Process Temperature Measurement

The surface temperature of the visible nip point of the tape was measured using the long wave infrared (LWIR) camera. The apparent emissivity of the material is required for measuring the temperature with this method. To determine the apparent emissivity, a single layer of material was placed on the tool surface and a thermocouple was attached on the material surface. The material was heated by heating the tool and sufficient time was given to reach the steady state in the material. The end effector of the tape placement robot was positioned such that the thermal image was similar to actual placement conditions. Thermocouple readings were compared with thermal image readings of the same location. The calibration was performed around 220 °C and the apparent emissivity was found to be 0.85 for the CF/PEKK material.

4.2.4 Pressure Measurement

Although the process is controlled by the so called “compaction force”, the actual pressure distribution under the compaction roller is unknown. During placement, the compaction roller applies the pressure while rotating. However, the effect of roller rotation on the normal pressure is negligible and the dynamic case can be simplified into a static one [33]. Fujifilm Prescale LLW pressure sensitive films were used to measure the contact area under the compaction roller. Pieces of the pressure sensitive film were fixed on the tool and different compaction forces were applied with the placement robot statically, as demonstrated in Figure 4.4. A force range of 100 to 800 N was covered with steps of 100 N. Then, the dimensions of the stains on the pressure films were measured. It was assumed that the pressure distribution was uniform and the applied force was divided by the measured area to calculate the average compaction pressure.

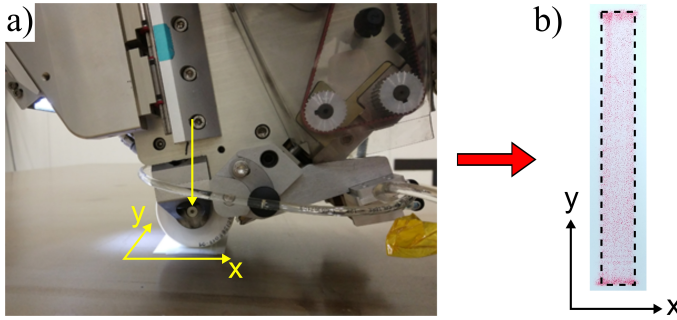


Figure 4.4. a) Static pressure application with the LAFP machine b) a stained pressure film with the assumed uniform pressure area.

4.3 Effective Intimate Contact

The resin-rich area on the surface is a pre-requisite for bond strength development between the subsequent layers, which is explained with the autohesion theory [7]. Therefore, the degree of intimate contact is meaningful only if it consists of resin-rich areas. However, current intimate contact models assume that the surface asperities are homogeneous. Considering the fiber-rich nature of the tape surface prior to compaction, there is a need for a new definition of the intimate contact phenomenon. Within a region of interest, the ratio of the compacted *resin-rich* area to the whole projected area is designated as the *degree of effective intimate contact* (DEIC) in this work.

4.3.1 Characterization

The methodology to obtain the degree of effective intimate contact is summarized in Figure 4.5. Micrographs were taken from the tool side of the surfaces with a Keyence VHX-2000 system equipped with a VH-Z100 lens. Five images were taken for each specimen with 200x magnification (image size approximately $1.6 \times 1.2 \text{ mm}^2$). In the first step, grayscale intensity histograms were generated for each image using the software of the microscope. These histograms show how many pixels are present for each grayscale value in an interval of 0 and 255 where 0 is black and 255 is white. Peaks in such a histogram designates the clusters of pixels that belong to certain features in the image [34]. Two classes of histograms were observed. The first class of histograms belonged to the samples which have significant amount of resin-rich area on the surface after compaction. There were two clear peaks which represent the dry fibers (the peak with a lower greyscale value) and the compacted resin area (the peak with a higher greyscale value). For each image, a threshold was determined at the local minimum between the two peaks. The pixels with a grayscale value higher than this threshold were selected as the area in effective intimate contact. The second class of histograms were observed for the samples with a low amount of resin on the surface after compaction. Only a single peak was present in these histograms, making it difficult to set a threshold value. In such cases, the threshold was determined based on the point where the slope of the histogram

curve is the closest to zero after the first peak as the grayscale intensity value increases. For both cases, this selected area included a low amount of dry fibers in addition to the compacted resin-rich areas. In an attempt to eliminate the dry fibers from the selected area, all sub-areas smaller than $500\mu\text{m}^2$ were excluded. This value was found to be appropriate for selecting the resin-rich areas as a result of trials with different minimum area thresholds on many images.

Two reference cases, unprocessed and fully compacted tapes, were examined with the proposed methodology to demonstrate its validity on the extreme cases and compare with the available intimate contact models. Fully compacted samples were created by compacting a single layer of a $30\text{ mm} \times 30\text{ mm}$ of the same material in a press at a temperature of 380°C and a pressure of 2 MPa for 20 minutes. These parameters were determined based on prior experience with CF/PEKK materials.

Microstructure of the LAFP-processed strips were qualitatively investigated with cross-sectional microscopy for more insight about effective intimate contact development. Samples were embedded in epoxy and polished for this purpose. The same microscopy system is used to obtain the images.

4.3.2 Analysis of Variance

The analysis of variance (ANOVA) method was used to evaluate the effects of the process parameters given in Table 4.1 on the mean of the degree of effective intimate contact measurements. Matlab function *anovan* was used for this purpose [35]. The outputs of this function were p-values for each process parameter. p-values smaller than 0.05 imply that the mean response of the specific parameter is different from the mean of all data within a confidence interval of 95 %. The effects of such a parameter can be considered statistically significant.

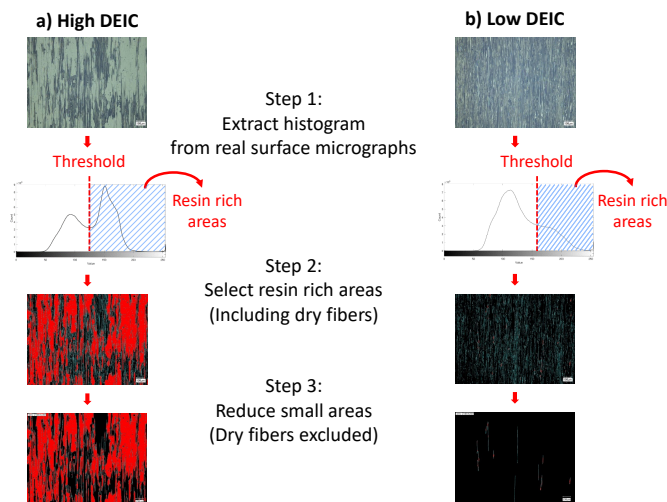


Figure 4.5. Measurement of degree of effective intimate contact from histograms of optical microscope images.

4.3.3 Intimate Contact Calculation Based on Squeeze Flow Models

Effective intimate contact measurements were compared with the squeeze flow-based intimate contact models. As explained in the following section, the temperature and pressure history of the material are required to calculate the final degree of intimate contact. The temperature history of the tape during compaction was calculated with a heat transfer model. The compaction pressure during the process was determined using the methodology presented in Section 4.2.4. These two process-induced parameters were then fed into two intimate contact models available in the literature.

Intimate Contact Models

Two squeeze flow-based intimate contact models were used to predict intimate contact development on a single tape processed with LAFP. The first model proposed by Lee and Springer [20] approximates the surface of the tape as a series of uniform rectangles. The degree of intimate contact can be found with the following equation:

$$D_{ic}(t) = \frac{1}{1 + \frac{w_0}{b_0}} \left[1 + 5 \left(1 + \frac{w_0}{b_0} \right) \left(\frac{a_0}{b_0} \right)^2 \int_0^{t_c} \frac{P_{app}}{\mu(T)} dt \right]^{\frac{1}{5}} \quad (4.1)$$

where $\frac{w_0}{b_0}$ and $\frac{a_0}{b_0}$ are geometrical parameters defining the uniform rectangular representation, T is the temperature, P_{app} is the compaction pressure, t is the compaction time and $\mu(T)$ is the temperature dependent viscosity of the material. The geometrical parameters were obtained from real surface measurements with a procedure similar to the work of Schaefer et al. [32]. Surface profiles were measured with an Olympus LEXT OLS3100 confocal laser scanning microscope. The parameters $\frac{w_0}{b_0}$ and $\frac{a_0}{b_0}$ were found by calculating the average of the ratio of the material and gaps at different height levels within $\pm 2\sigma$ from the mean surface height, where σ designates the standard deviation.

The second model proposed by Yang and Pitchumani [22] approximates the composite surface as a fractal Cantor set and calculates the degree of intimate contact as follows:

$$D_{ic}(t) = \frac{1}{f^n} \left[\frac{5}{4} \left(\frac{h_0}{L_0} \right)^2 \frac{f^{\frac{2nD}{2-D} + n + 4}}{(f+1)^2} \int_{t_{(n+1)}}^t \frac{P_{app}}{\mu(T)} dt + 1 \right]^{\frac{1}{5}} \quad (4.2)$$

for $t_{(n+1)} \leq t \leq t_{(n)}$

where f is the fractal scaling factor, n is the generation number of the Cantor set, D is the fractal dimension and $\frac{h_0}{L_0}$ is the ratio of the height of the first generation asperities to the Cantor block length. These parameters were determined as described in the original paper from real surface profiles and their power spectra. The rest of the parameters are the same with Equation (4.1).

Figure 4.6 demonstrates the corresponding idealized surface representations for both intimate contact models on an example measured surface profile. The average geometrical parameters used for the intimate contact models are summarized in Table 4.2.

T was calculated from the heat transfer model in Section 4.3.3. P_{app} was obtained from static contact measurements described in Section 4.2.4. t was calculated by dividing the contact length obtained from the pressure sensitive films by the placement

speed. $\mu(T)$ for CF/PEKK material was adapted from [36]. It is expressed as the following relation:

$$\mu(T) = 4.362 \times 10^7 e^{-0.0401(T-623)} \text{ Pas} \quad (4.3)$$

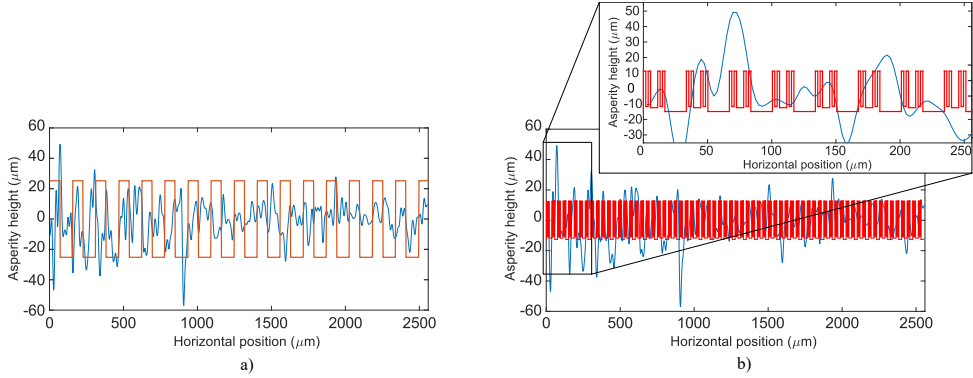


Figure 4.6. Corresponding idealized surface representations on a real surface profile.
a) Uniform rectangle approximation and b) Cantor set approximation (only first three generations are shown for clarity).

Table 4.2. Surface parameters used in the intimate contact models

Surface model	Parameter	Explanation	Value
Lee and Springer [20]	w_0/b_0	Ratio of asperity width to gap width	1.11
	a_0/b_0	Ratio of asperity height to asperity width	0.57
Yang and Pitchumani [22]	f	Scaling factor	1.09
	D	Fractal dimension	1.63
	h_0/L_0	Ratio of first generation asperity height to Cantor block length	0.20
	n	Total number of generations	15

Heat Transfer Model

A three dimensional Lagrangian finite element (FE) model of the placed tape and the tool with a moving placement head configuration, based on authors' previous work [37], was used to estimate the transient through-thickness temperature distribution during compaction. Abaqus 2017 finite element package was used to create and solve the model.

The model solves the energy equation to find the transient temperature distribution $T(t)$ within the bodies, assuming the internal heat generation is negligible:

$$\rho C_p \frac{\partial T}{\partial t} = \nabla(k \nabla T) \quad (4.4)$$

where ρ is the density, C_p is the specific heat and k is the conductivity of the material. Referring to Figure 4.7, the following boundary conditions were applied:

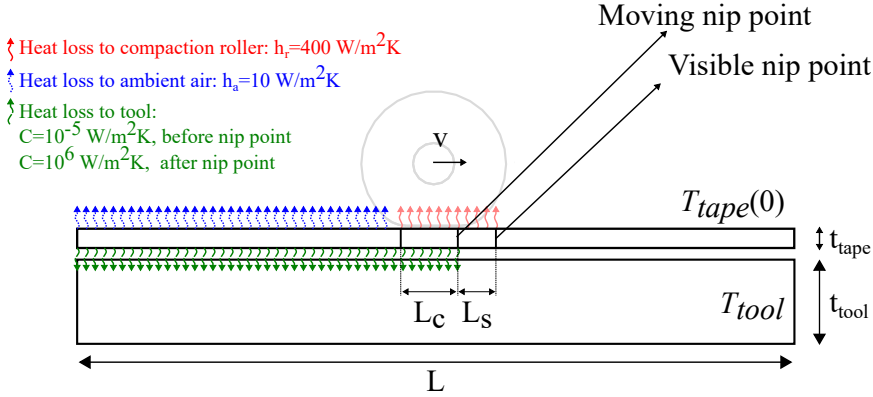


Figure 4.7. Modeling space and moving boundary conditions in the FE model. h and C represent the applied convection coefficient and thermal conductance, respectively. For the other parameters, please refer to Table 4.3.

4

The aluminum tool was assumed to have a fixed temperature T_{tool} due to its large thermal mass. The incoming tape was assumed to reach uniform through-thickness temperature $T_{tape}(0)$ at the visible nip point. Past the visible nip point, the tape cools down due to the contact with the compaction roller in the shadow and compaction zones (see Figure 4.1). Following that, the ambient air cools down the tape at the top surface. The heat loss to the compaction roller and the ambient air after compaction were formulated as a moving convection boundary condition:

$$k\nabla T = -h(T - T_a) \quad (4.5)$$

where h is the convection coefficient and T_a is the ambient temperature. The convection coefficient for the roller, h_r , and for the air, h_a , were taken as $400 \text{ W/m}^2\text{K}$ [38] and $10 \text{ W/m}^2\text{K}$ [39], respectively. T_a was approximated as 50°C for the roller [40] and 20°C for the ambient air. The coordinates of the areas where the convection boundary condition is active were updated with an Abaqus FILM subroutine.

At the tape-tool interface, the heat transfer was modeled with a thermal contact:

$$q = C(T_{tape} - T_{tool}) \quad (4.6)$$

where q is the heat flux between the tape and the tool and C is the thermal contact conductance. C was updated based on the location of the moving nip point and it was implemented with an Abaqus GAPCON subroutine. At the regions in front of the nip point, no heat transfer was possible between the tape and the tool. To impose this condition without creating numerical problems, the thermal contact conductance was set to a very low value, namely $10^{-5} \text{ W/m}^2\text{K}$. The thermal contact conductance was set to $10^6 \text{ W/m}^2\text{K}$ past the nip point, assuming almost perfect heat transfer occurs at the interface between the tape and the tool.

The temperature history of the tape was calculated for the scenario where the highest intimate contact is expected (the lowest placement speed (v) and the highest visible

nip point temperature ($T_{tape}(0)$), table temperature (T_{tool}) and compaction force in Table 4.1). The roller contact length at the compaction zone, L_c , was determined from the contact length measurements described in Section 4.2.4. The contact length for a compaction force of 800 N was used since it was observed that this parameter did not affect the temperature history significantly. The length of the shadow, L_s , was estimated from the computer aided design (CAD) drawings of the end effector. The process related and geometric parameters used in the model are summarized in Table 4.3. Thermal material properties provided in Table 4.4 were used for the composite tape.

DC3D8 linear hexahedral heat transfer elements were used to mesh the tape and the tool. The tape was meshed with 10, 120 and 6 uniform elements in the thickness, length and width directions, respectively.

Table 4.3. The process related and geometric parameters used in the heat transfer model

Parameter	Symbol	Value	Unit
Tape temperature prior the visible nip point	$T_{tape}(0)$	400	°C
Fixed tool temperature	T_{tool}	155	°C
Placement speed	v	100	mm/s
Compaction pressure (for intimate contact models)	P_{app}	0.29-0.86	MPa
Roller contact length in the compaction zone	L_c	16	mm
Roller contact length in the shadow zone	L_s	4	mm
Domain length	L	100	mm
Tape thickness	t_{tape}	0.15	mm
Tool thickness	t_{tool}	30	mm
Tape width		50.8	mm

4.4 Results

4.4.1 Pressure Measurement

The average compaction pressure has a nonlinear relationship with the applied compaction force, as seen in Figure 4.8. The compaction roller deforms more as the compaction force increases, creating a larger contact area. Even though a larger contact area is favorable for better intimate contact development, it poses a limitation on reaching high pressure. Comparison of compaction force and pressure under the roller provides useful information for further discussions.

4.4.2 Surface and Cross-Sectional Micrographs

Effective intimate contact measurements of unprocessed tapes and fully consolidated samples are summarized in Table 4.5 along with the predictions made with Equations (4.1) and (4.2). Reflecting the fiber-rich structure of the surface, the degree of effec-

Table 4.4. Thermal material properties of CF/PEKK

Density ^a (kg/m ³)	Thermal conductivity (W/m°C)		Specific Heat ^d (J/kg°C)	Temperature (°C)
	Longitudinal ^b	Transverse ^c		
1506	6	0.73	990	50
			1176	100
			1353	150
			1675	200
			1865	250
			2220	300
			2289	350

^a Measured at room temperature according to ASTM D792
^b Estimated from [38], based on the similarity of transverse thermal conductivity to APC-2
^c Averaged from [41]
^d Measured with differential scanning calorimetry with a heating rate of 20 °C/s

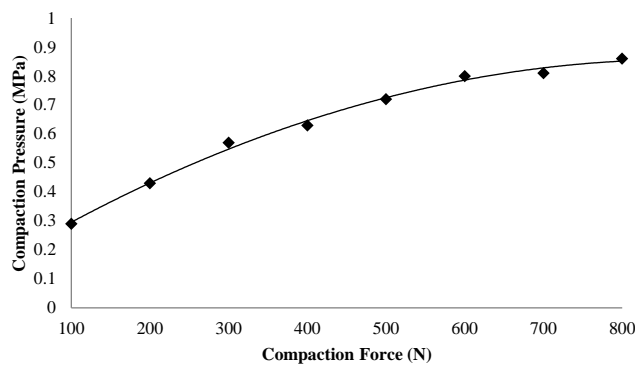


Figure 4.8. Nonlinear relation between the applied compaction force and the average compaction pressure measured with pressure sensitive films due to the increasing contact area

tive intimate contact was very low for the unprocessed tow. On the contrary, press consolidated samples showed almost complete effective intimate contact. The major difference between the predictions and measurements can be observed for the unprocessed tape. Both squeeze flow models indicate that the unprocessed tape is in considerable intimate contact with a hypothetical opposite surface, as demonstrated in Figure 4.6. However, since the models consider only the surface profiles and not the microstructure, the effect of resin content at the surface is not accounted for. The effective intimate contact concept illustrated in Figure 4.5 provides a methodology which is sensitive to the resin content at the surface and able to measure the whole range of degree of effective intimate contact (i. e., 0–100 %) for the fiber-placed samples.

Table 4.5. Degree of effective intimate contact of the reference cases and degree of intimate contact predictions with the currently available models

	Measured DEIC (%)	Lee & Springer (%)	Yang & Pitchumani (%)
Unprocessed Tape	0.2±0.4	47.4	27.5
Press Consolidated Ply (at 380 °C, 20 min)	96.6±1.8	100	100

The surface micrographs shown in Figure 4.9 demonstrate the morphology of the contact surface for a range of effective intimate contact levels. In Figure 4.9a, a specimen with a low degree of effective intimate contact (1 %) is shown. The surface exhibits very low amounts of resin content and the surface is covered with dry fibers. In Figure 4.9b, a surface with slightly higher amount of degree of intimate contact (23 %) is shown. Squeezed out and flattened resin portions are apparent. Fibers are covered with this squeezed-out resin locally. Flattened resin regions mostly elongate along fibers since dry fibers restrict the motion of the molten resin more in the perpendicular direction. The micrograph in Figure 4.9c shows a high degree of effective intimate contact obtained within this study (57 %), where more resin is squeezed out and covers a larger portion of the surface. The constraining effect of the dry fibers can still be observed on the wetting behavior of the resin material. Within large impregnated areas, some gaps elongated in the fiber direction exist.

Representative cross-sectional micrographs of specimens manufactured with the same nip point temperature (400 °C) and placement speed (100 mm/s) but different compaction forces (100 N and 800 N) are shown in Figure 4.10. Such a comparison is informative about the change in the microstructure during the intimate contact development. Figure 4.10a shows a sample with low intimate contact development (22.2 %) due to low compaction force. In addition to flattened fiber-resin mixture, incompletely compacted (non-flat) resin-fiber mixture and loose dry fibers can be observed at the surface on the tool side. The specimen in Figure 4.10b represents a specimen with higher degree of intimate contact (54.8 %) since higher compaction force results in more deformation at the surface given the same thermal history (Equations (4.1) and (4.2)). Regions with resin-fiber mixture at the surface on the tool side are mostly flattened. Dry fibers are present; however, it can be observed that they are compressed more than the case with the lower compaction force.

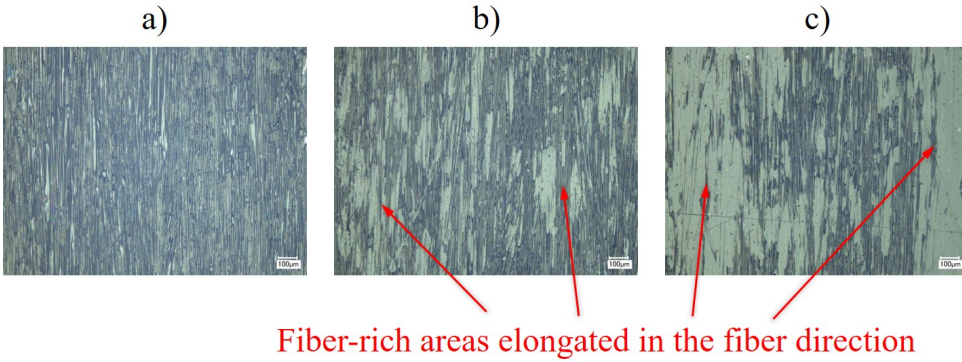


Figure 4.9. Representative surface micrographs for different levels of effective intimate contact: a) 1 % ($T_{\text{tool}}=20\text{ }^{\circ}\text{C}$, $T_{\text{np}}=380\text{ }^{\circ}\text{C}$, $F=100\text{ N}$, $V=100\text{ mm/s}$), b) 23 % ($T_{\text{tool}}=155\text{ }^{\circ}\text{C}$, $T_{\text{np}}=400\text{ }^{\circ}\text{C}$, $F=400\text{ N}$, $V=400\text{ mm/s}$), c) 57 % ($T_{\text{tool}}=155\text{ }^{\circ}\text{C}$, $T_{\text{np}}=400\text{ }^{\circ}\text{C}$, $F=800\text{ N}$, $V=400\text{ mm/s}$).

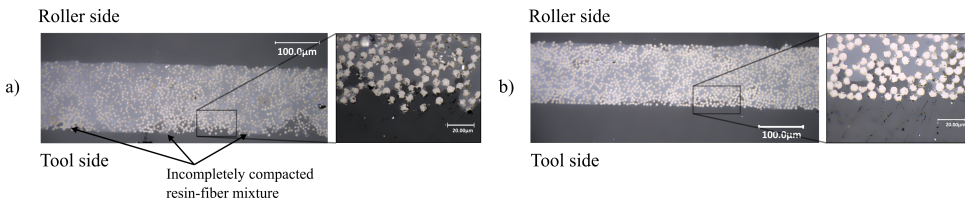


Figure 4.10. Representative cross-section micrographs for different levels of compaction force at the same nip point temperature ($400\text{ }^{\circ}\text{C}$) and process speed (100 mm/s). a) 100 N , loose dry fibers in magnified view. b) 800 N , compressed dry fibers in magnified view.

4.4.3 Effects of Process Parameters on Intimate Contact Development

Final degrees of effective intimate contact at different tool temperatures, nip point temperatures, compaction forces and placement speeds are summarized in Figure 4.11. ANOVA analysis is applied on this data set to find statistically significant parameters on effective intimate contact development.

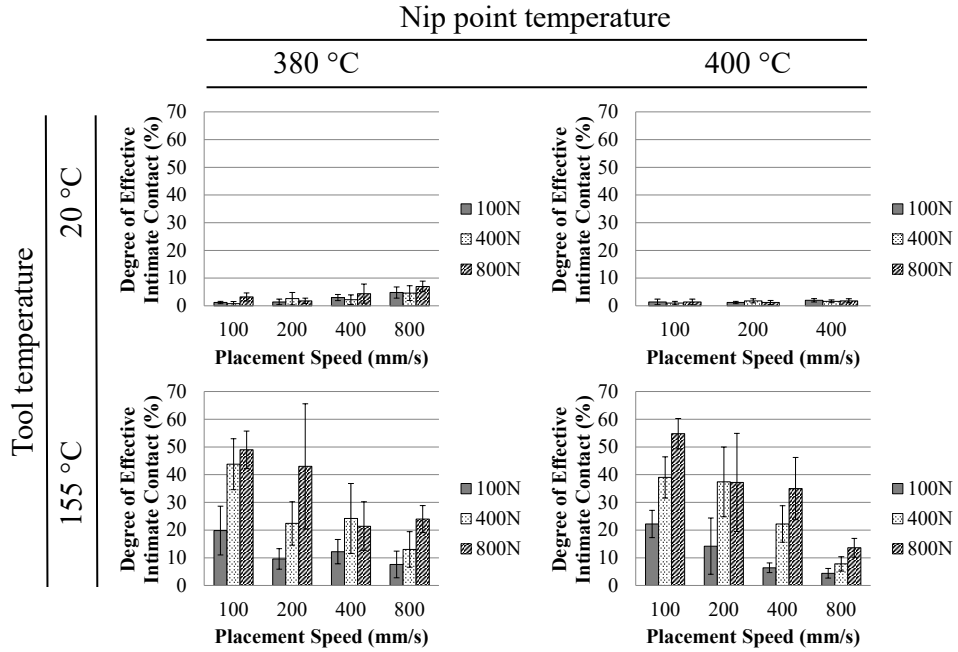


Figure 4.11. Experimental degree of effective intimate contact for all process parameters. Top row: cold tool (20 °C), bottom row: hot tool (155 °C), left column: 380 °C nip point temperature, right column: 400 °C nip point temperature. The error bars show the standard deviation.

Analysis of Variance

The results presented in Table 4.6 indicate that the sources tool temperature (TT), compaction force (CF), placement speed (PS) and the interaction terms TT*CF and TT*PS caused statistically significant differences on the degree of effective intimate contact within the parameters presented in Table 4.1. For the other sources, it is not possible to distinguish the effects from experimental scatter. Significance of the interaction terms (sources TT*CF and TT*PS) shows that the effect of the tool temperature dominates over the others. This is also evident in Figure 4.11: samples placed on the cold tool (top row) have very low degrees of effective intimate contact compared to the samples placed on the hot tool (bottom row) and effects of compaction force and placement speed are not

apparent. Therefore, in order to assess the effects of compaction force and placement speed, the results from the hot tool should be used.

Interestingly, the target nip point temperature (source NPT) did not cause significant changes on the degree of effective intimate contact. Although the squeeze flow viscosity of CF/PEKK decreases more than twice when the temperature increases from 380 °C to 390 °C according to Equation (4.3), this decrease was not reflected in the results as an increase in effective intimate contact development. A possible explanation is the very short time spent above the melting temperature due to the quenching effect of the tool. Hence, data from two different nip point temperatures were combined to present the results of the effects of compaction force and placement speed.

Compaction Force

The effect of the compaction force on the degree of effective intimate contact is shown in Figure 4.12. The horizontal axis of the figure is replaced with the compaction pressure instead of the compaction force, according to the relationship presented in Figure 4.8. The compaction forces of 100, 400 and 800 N correspond to the average compaction pressures of 0.29, 0.63 and 0.86 MPa, respectively. A linear fit can express the relationship for every placement speed. It should be noted that the linear relationship holds true only for the compaction pressure under the roller instead of the applied compaction force. As the placement speed increases, the effect of the compaction pressure decreases, which is shown with a decrease in the slope of the fit curves.

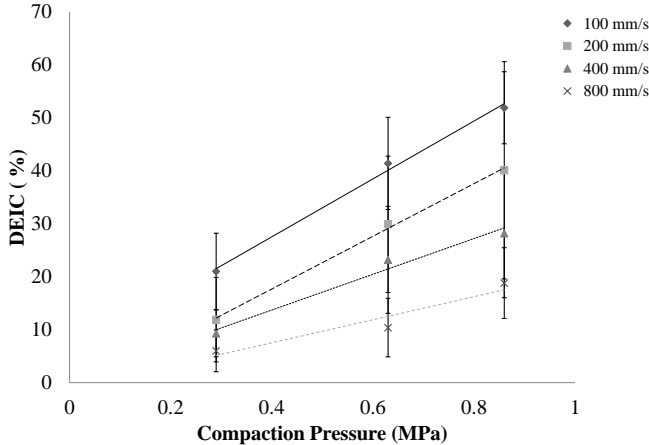


Figure 4.12. Degree of effective intimate contact as a function of the average compaction pressure under the roller at different placement speeds

Placement Speed

The effect of the placement speed on the degree of effective intimate contact is shown in Figure 4.13. As the process speed increases, the time available for compaction

decreases. A non-linear decrease is observed as the placement speed increases. At the lowest compaction force (100 N), the degree of effective intimate contact is affected less by the increasing placement speed and no significant change was observed above 100 mm/s.

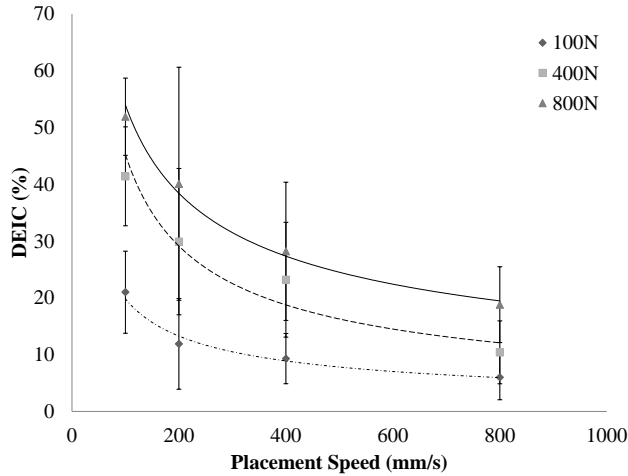


Figure 4.13. Degree of effective intimate contact as a function of placement speed at different compaction forces

4.4.4 Temperature History and Intimate Contact Predictions

The calculated temperature history of the top and bottom sides of the tape are shown in Figure 4.14. In the non-illuminated shadow zone, the temperature of the tape decreases unevenly in the thickness direction until it reaches the nip point (the beginning of the consolidation zone). The top surface of the tape cools down faster than the bottom side due to direct contact with the roller. When the tape reaches the nip point, the bottom and top surfaces are at 383 °C and 375 °C, respectively. However, as soon as the tape enters the consolidation zone, the bottom surface of the tape quenches to the mold temperature rapidly (Figure 4.14b). This causes the bottom surface to stay above the melting temperature for only 2.5 ms. On the other hand, the top surface stays above the melting temperature for 15 ms, a considerably longer duration.

The degree of intimate contact predictions based on the calculated temperature history of the bottom side of the tape are shown in Figure 4.15 along with the experimental results. Similar trends were observed for the fractal and uniform rectangular intimate contact models. Despite the increase in pressure, almost no change occurs in the predictions. Due to the very limited time spent above the melting temperature at the bottom surface of the tape, the surface asperities do not flatten and the final degree of intimate contact calculation is dominated by the initial surface parameters given in Table 4.2. The results are, therefore, only shown for the slowest placement speed (100 mm/s) since the

predictions for higher placement speeds would result in the same final degree of intimate contact.

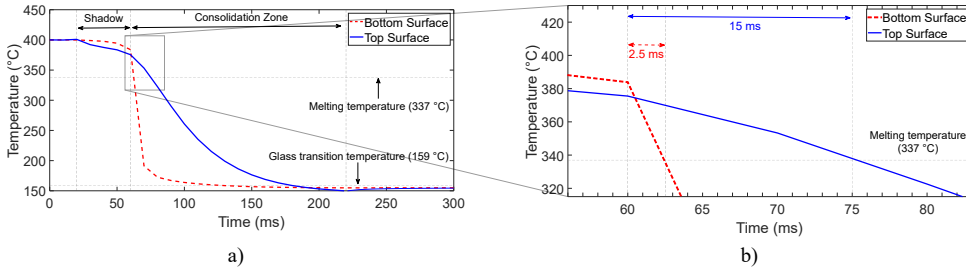


Figure 4.14. Calculated temperature history of the thermoplastic tape. a) Full history. b) Magnified view of consolidation zone above the melting temperature. Time spent above the melting temperature under the compaction roller is designated with a blue arrow for the top surface and a dashed red arrow for the bottom surface.

4.5 Discussion

Based on the results of surface and cross-sectional microscopy, it can be stated that intimate contact development during LAFP is a combination of multiple mechanisms. Squeeze flow of surface asperities, the common approach to explain intimate contact development for thermoplastic composites [19, 20, 22], plays a partial role. As seen in Figure 4.10, samples manufactured with lower compaction forces contain incompletely deformed surface asperities filled with a mixture of fiber and resin. As the material is processed with higher compaction forces, incompletely deformed surface asperities are less apparent. Clusters of dry fibers are present for all cases. At high compaction forces, although the squeeze flow of surface asperities seems to be completed, full effective intimate contact is not achieved. A portion of the compaction energy is spent on compressing the dry fiber clusters and does not result in effective intimate contact development.

Effective intimate contact development at the fiber-rich regions cannot be explained by the squeeze flow of a fiber-resin mixture. Resin infiltration, which has been investigated for other composite manufacturing methods [42, 43], should be taken into consideration. Two mechanisms can be identified for impregnation of dry fiber bundles. The first mechanism is the through-thickness percolation flow of the resin. The resin needs to permeate towards the surface to facilitate effective intimate contact. The other mechanism is the in-plane flow of resin at the compaction surface. This mechanism is effective mostly in the fiber direction because the dry fiber network restricts the resin flow in the direction perpendicular to fibers. As a result, the fiber-rich areas within the impregnated zones are typically elongated in the fiber direction, as demonstrated in Figure 4.9. This observation is in-line with the literature, where the permeability in the fiber direction is reported to be an order of magnitude higher than the permeability in the transverse direction [44, 45]. Figure 4.16 schematically depicts the proposed effective intimate contact development during LAFP based on our observations. In Figure 4.16a, the

Table 4.6. Results of the multiway ANOVA. Asterisk symbol (*) designates the interaction between the related parameters. $p < 0.05$ means that the effect of the parameter or the interaction is statistically significant.

Source	p-value
Tool temperature (TT)	0
Compaction force (CF)	0
Placement speed (PS)	0
Nip point temperature (NPT)	0.3684
TT*CF	0
TT*PS	0
TT*NPT	0.2586
CF*PS	0.3065
CF*NPT	0.956
PS*NPT	0.2065

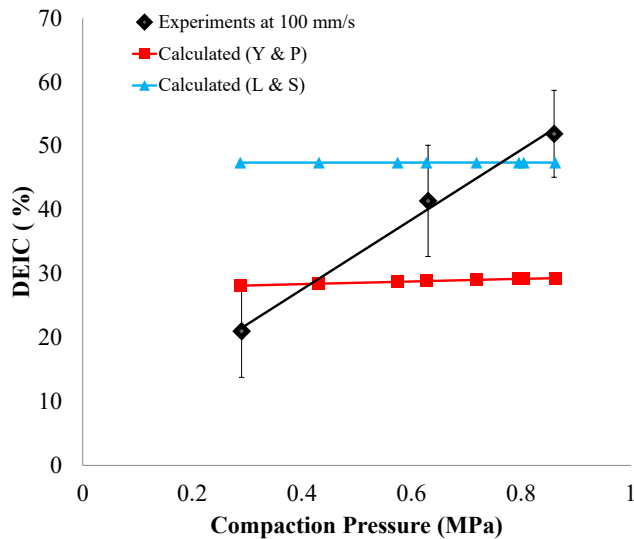


Figure 4.15. Experimentally obtained degree of effective intimate contact and calculated intimate contact based on calculated thermal history. Placement speed: 100 mm/s. L & S: Uniform rectangular surface representation [20], Y & P: Fractal surface representation [22].

state of the thermoplastic composite tape prior to the nip point is shown. Zones 1 and 3 are fiber-rich regions, whereas Zone 2 represents the resin-rich portions of the material. After compaction (Figure 4.16b), all of these regions are in physical contact. However, Zone 1 is not in effective intimate contact since no resin is present at the interface. Zone 2 achieves effective intimate contact with the squeeze flow mechanism. Zone 3 requires through thickness and in-plane percolation flow to establish effective intimate contact.

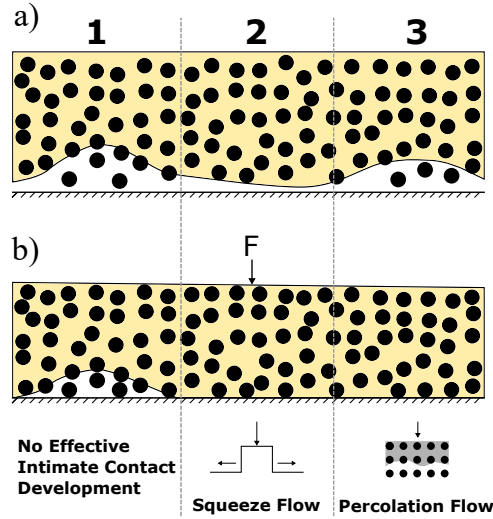


Figure 4.16. Development of effective intimate contact and underlying mechanisms for initial surfaces with different microstructure. a) uncompressed composite tape, b) compressed composite tape.

The share of these separate mechanisms on effective intimate contact development depends on the initial fiber-resin distribution of the tape and severity of microstructural changes during the heating phase of LAFP. Initial fiber-resin distribution of a thermoplastic composite tape highly depends on the tape manufacturing processes. Although similar constituents and specifications are provided for tapes produced by different manufacturers, fiber uniformity, resin content at the surface and void size/distribution varies [46–48]. In connection with the initial state of the material, the heating phase affects tapes manufactured by different suppliers differently, as reported in [28]. Also, the state of the substrate at the nip point should be considered for an accurate analysis of the final degree of effective intimate contact at each interface in a fiber placed laminate, which is beyond the scope of this work. Therefore, more efforts should be spent on understanding the microstructure of the thermoplastic tape and substrate just before the nip point during LAFP.

The response of the experimentally obtained degree of effective intimate contact to increasing compaction pressure differed from the response of the degree of intimate contact predicted by Equations (4.1) and (4.2), which use the squeeze flow assumptions. Intimate contact development based on homogenized transverse squeeze flow models were not sensitive to an increase in pressure. This insensitivity can be explained by the

fact that only the surface temperature was used for predicting intimate contact development with the squeeze flow models. With the quenching effect of the tool surface, the resin near the surface is expected to cool down rapidly. However, molten resin is present through the thickness of the tape for a longer duration and contributes to the effective intimate contact development via percolation flow. Such a mechanism can also explain bonding below melting temperature, reported for CF/PPS tapes welded onto carbon woven fabric reinforced PPS laminates [49] and CF/PEEK laminates manufactured with LAFP [27]. This phenomenon was attributed to the autohesion of the amorphous chains in the semi-crystalline polymer at temperatures between the melting and glass transition temperatures. However, bonding was found to be limited to the intimate contact development in both works, indicating that its effect on the inter-laminar bond development was more pronounced than the autohesion mechanism. This means that the effective intimate contact development concept, which is introduced in this paper, might improve the accuracy of bonding predictions.

The samples manufactured with different placement speeds at a fixed compaction force can be linked to different stages of intimate contact development. Figure 4.17 shows effective intimate contact development as a function of compaction time, calculated by dividing the contact length obtained from pressure sensitive films by the placement speed. Experimental data for intimate contact development available in the literature covers a range from tens to hundreds of seconds [19, 20, 22]. Since only a fraction of a second is available for compaction during LAFP, it is difficult to make a direct comparison. However, the trends show resemblance in terms of a steep increase at the beginning of compaction, followed by a decrease in the evolution rate. The same behavior was also confirmed for small time scales by numerical calculations presented in [50]. Two reasons can be identified as the reason for this behavior. The first one is the squeeze flow mechanism, which occurs at the resin-rich regions of the surface. Initially, the surface asperities have less contact and high local pressure, causing a rapid increase in the degree of effective intimate contact. As the asperities deform, increased contact area decreases the local pressure. Therefore, the evolution of the degree of effective intimate contact slows down. The second mechanism is the cooling of the tape as demonstrated in Figure 4.14. The drop in temperature plays a hindering role for both the squeeze flow and percolation flow mechanisms as it causes the polymer viscosity to increase.

4.6 Conclusion

Intimate contact development during LAFP is a complex process involving multiple mechanisms. Due to short compaction times and very limited time available above the melting temperature of the semi-crystalline polymer, complete resin flow cannot be established at the tape surface as in conventional processing methods such as press molding and autoclave. Dry fibers were observed at the material surface after compaction, meaning that complete mechanical contact with the opposing surface might not contribute to the elimination of the interlaminar voids or development of bonding strength. In order to quantify the amount of flattened resin content at the surface, the concept of *effective intimate contact* was proposed and a methodology to obtain the degree of effective intimate contact from surface micrographs was presented.

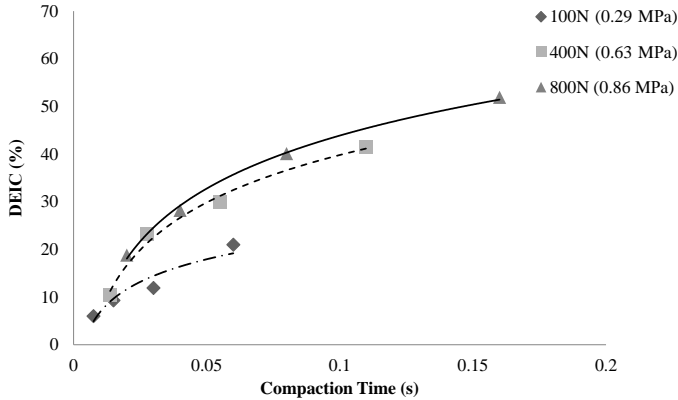


Figure 4.17. Time dependent effective intimate contact development based on different placement speeds at constant compaction force

Effective intimate contact develops with squeeze flow at the resin-rich portions of the surface; however, through-thickness and in-plane percolation flow is required to impregnate the regions with compressed dry fibers. Due to the percolation flow mechanism playing a role, the through-thickness temperature distribution of the tape gains importance for effective intimate contact development during the LAFP process. Currently available intimate contact models could not predict the experimentally obtained degree of effective intimate contact since they consider the material surface as a homogeneous fiber-resin mixture which deforms only with the squeeze flow mechanism. In addition, the through-thickness temperature distribution was not accounted for. Future work is identified as modeling effective intimate contact development with all contributing mechanisms and performing experiments for model validation.

References

- [1] Beyeler, E.P, Phillips, W., Guceri, S.I.. Experimental Investigation of Laser-Assisted Thermoplastic Tape Consolidation. *Journal of Thermoplastic Composite Materials* 1988;1(1):107–121.
- [2] Choe, C.R., Lee, K.H.. Nonisothermal Crystallization Kinetics of Poly(etheretherketone) (PEEK). *Polymer Engineering and Science* 1989;29(12):801–805.
- [3] Roux, M., Eguémann, N., Dransfeld, C., Thiébaud, F., Perreux, D.. Thermoplastic carbon fibre-reinforced polymer recycling with electrodynamical fragmentation: From cradle to cradle. *Journal of Thermoplastic Composite Materials* 2017;30(3):381–403.
- [4] Grant, C.. Automated processes for composite aircraft structure. *Industrial Robot* 2006;33(2):117–121.

- [5] Pitchumani, R., Ranganathan, S., Don, R.C., Gillespie, J.W., Lamontia, M.A.. Analysis of Transport Phenomena Governing Interfacial Bonding and Void Dynamics During Thermoplastic Tow-placement. *International Journal of Heat and Mass Transfer* 1996;39(9):1883–1897.
- [6] Sonmez, F.O., Hahn, H.T.. Analysis of the On-Line Consolidation Process in Thermoplastic Composite Tape Placement. *Journal of Thermoplastic Composite Materials* 1997;10:543–572.
- [7] Yang, F., Pitchumani, R.. Nonisothermal Healing and Interlaminar Bond Strength Evolution During Thermoplastic Matrix Composites Processing. *Polymer Composites* 2003;24(2):263–278.
- [8] Tierney, J., Gillespie, J.W.. Crystallization kinetics behavior of PEEK based composites exposed to high heating and cooling rates. *Composites Part A: Applied Science and Manufacturing* 2004;35(5):547–558.
- [9] Grouve, W.J.B., Warnet, L.L., Rietman, B., Akkerman, R.. On the weld strength of in situ tape placed reinforcements on weave reinforced structures. *Composites Part A: Applied Science and Manufacturing* 2012;43(9):1530–1536.
- [10] Barasinski, A., Leygue, A., Soccarr, E., Poitou, A.. Identification of non uniform thermal contact resistance in automated tape placement process. *International Journal of Material Forming* 2014;7(4):479–486.
- [11] Simacek, P., Advani, S.G., Gruber, M.B., Jensen, B.. A non-local void filling model to describe its dynamics during processing thermoplastic composites. *Composites Part A: Applied Science and Manufacturing* 2013;46(1):154–165.
- [12] Comer, A.J., Ray, D., Obande, W.O., Jones, D., Lyons, J., Rosca, I., et al. Mechanical characterisation of carbon fibre-PEEK manufactured by laser-assisted automated-tape-placement and autoclave. *Composites Part A: Applied Science and Manufacturing* 2015;69:10–20.
- [13] Stokes-Griffin, C.M., Compston, P.. The effect of processing temperature and placement rate on the short beam strength of carbon fibre-PEEK manufactured using a laser tape placement process. *Composites Part A: Applied Science and Manufacturing* 2015;78:274–283.
- [14] Weiler, T., Emonts, M., Wollenburg, L., Janssen, H.. Transient thermal analysis of laser-assisted thermoplastic tape placement at high process speeds by use of analytical solutions. *Journal of Thermoplastic Composite Materials* 2018;31(3):311–338.
- [15] Kim, Y.H., Wool, R.P. A theory of healing at a polymer-polymer interface. *Macromolecules* 1983;16(7):1115–1120.
- [16] Butler C.A., , McCullough R. L., . An Analysis of Mechanisms Governing Fusion Bonding of Thermoplastic Composites. *Journal of Thermoplastic Composite Materials* 1998;11:339–363.

- [17] Mehdikhani, M., Gorbatiikh, L., Verpoest, I., Lomov, S.V. Voids in fiber-reinforced polymer composites: A review on their formation, characteristics, and effects on mechanical performance. *Journal of Composite Materials* 2019;53(12):1579–1669.
- [18] Levy, A., Heider, D., Tierney, J., Gillespie, J.W. Inter-layer thermal contact resistance evolution with the degree of intimate contact in the processing of thermoplastic composite laminates. *Journal of Composite Materials* 2014;48(4):491–503.
- [19] Dara, P.H., Loos, A.C.. Thermoplastic matrix composite processing model. Tech. Rep.; NASA; Virginia; 1985.
- [20] Lee, W.I., Springer, G.S.. A Model of the Manufacturing Process of Thermoplastic Matrix Composites. *Journal of Composite Materials* 1987;21(11):1017–1055.
- [21] Mantell, S.C., Springer, G.S.. Manufacturing Process Models for Thermoplastic Composites. *Journal of Composite Materials* 1992;26(16):2348–2377.
- [22] Yang, F., Pitchumani, R.. A fractal Cantor set based description of interlaminar contact evolution during thermoplastic composites processing. *Journal of Materials Science* 2001;36(19):4661–4671.
- [23] Mantell, S.C., Wang, Q., Springer, G.S.. Processing Thermoplastic Composites in a Press and by Tape Laying–Experimental Results. *Journal of Composite Materials* 1992;26:2378–2401.
- [24] Tierney, J., Gillespie, J.W.. Modeling of In Situ Strength Development for the Thermoplastic Composite Tow Placement Process. *Journal of Composite Materials* 2006;40(16):1487–1506.
- [25] Khan, M.A., Mitschang, P., Schledjewski, R.. Parametric study on processing parameters and resulting part quality through thermoplastic tape placement process. *Journal of Composite Materials* 2013;47(4):485–499.
- [26] Stokes-Griffin, C.M., Compston, P. An inverse model for optimisation of laser heat flux distributions in an automated laser tape placement process for carbon-fibre/PEEK. *Composites Part A: Applied Science and Manufacturing* 2016;88:190–197.
- [27] Stokes-Griffin, C.M., Compston, P. Investigation of sub-melt temperature bonding of carbon-fibre/PEEK in an automated laser tape placement process. *Composites Part A: Applied Science and Manufacturing* 2016;84:17–25.
- [28] Kok, T.. On the consolidation quality in laser assisted fiber placement: the role of the heating phase. Phd thesis; University of Twente; 2018.
- [29] Composites, T.A.. TenCate Cetex® TC1320 PEKK Resin System Product Data Sheet 2015;.
- [30] Composites, T.A.. TenCate Cetex® TC1200 PEEK Resin System Product Data Sheet 2017;.

- [31] Kok, T., Grouve, W.J.B., Warnet, L.L., Akkerman, R.. Intimate Contact Development in Laser Assisted Fiber Placement. ECCM17 - 17th European Conference on Composite Materials 2016;1(June):26–30.
- [32] Schaefer, P.M., Guglhoer, T., Sause, M.G., Drechsler, K.. Development of intimate contact during processing of carbon fiber reinforced Polyamide-6 tapes. *Journal of Reinforced Plastics and Composites* 2017;36(8):593–607.
- [33] Jiang, J., He, Y., Ke, Y.. Pressure distribution for automated fiber placement and design optimization of compaction rollers. *Journal of Reinforced Plastics and Composites* 2019;.
- [34] Burger, W., Burge, M.J.. *Principles of Digital Image Processing: Advanced Methods. Undergraduate Topics in Computer Science*; London: Springer London; 2013.
- [35] The MathWorks Inc, . *MATLAB and Statistics Toolbox Release 2017b*. 2017.
- [36] Lin, H.R., Advani, S.G.. Processing models and characterization of thermoplastic composite wound parts. *Polymer composites* 1997;18(3):405–411.
- [37] Çelik, O., Shroff, S., Teuwen, J.J.E., Bergsma, O.K., Benedictus, R.. A 3-D Finite Element Model for Thermal Analysis of Laser Assisted Fiber Placement. In: *SAMPE Europe*. Southampton; 2018,.
- [38] Sonmez, F.O., Hahn, H.T.. Modeling of Heat Transfer and Crystallization in Thermoplastic Composite Tape Placement Process. *Journal of Thermoplastic Composite Materials* 1997;10(3):198–240.
- [39] Cogswell, F.N.. *Thermoplastic aromatic polymer composites: a study of the structure, processing, and properties of carbon fibre reinforced polyetheretherketone and related materials*. Butterworth-Heinemann; 1992.
- [40] Stokes-Griffin, C.M., Compston, P.. A combined optical-thermal model for near-infrared laser heating of thermoplastic composites in an automated tape placement process. *Composites Part A: Applied Science and Manufacturing* 2015;75:104–115.
- [41] Coulson, M., Dantras, E., Olivier, P., Gleizes, N., Lacabanne, C.. Thermal conductivity and diffusivity of carbon-reinforced polyetherketoneketone composites. *Journal of Applied Polymer Science* 2019;136(38):47975.
- [42] Sommer, J.L., Mortensen, A.. Forced unidirectional infiltration of deformable porous media. *Journal of Fluid Mechanics* 1996;311(1):193–217.
- [43] Michaud, V., Törnqvist, R., Månson, J.A.. Impregnation of compressible fiber mats with a thermoplastic resin. Part II: Experiments. *Journal of Composite Materials* 2001;35(13):1174–1200.
- [44] Gebart, B.R.. Permeability of Unidirectional Reinforcements for RTM. *Journal of Composite Materials* 1992;26(8):1100–1133.

- [45] Zarandi, M.A.F, Arroyo, S., Pillai, K.M.. Longitudinal and transverse flows in fiber tows: Evaluation of theoretical permeability models through numerical predictions and experimental measurements. *Composites Part A: Applied Science and Manufacturing* 2019;119:73–87.
- [46] Lamontia, M.A., Gruber, M.B.. Remaining developments required for commercializing in situ thermoplastic ATP. In: *Proceedings of the SAMPE 2007 Conference*. Baltimore, MD. ISBN 1934551007; 2007, p. 1–15.
- [47] Gruber, M.B., Lockwood, I., Dolan, T., Funck, S., Tierney, J., Simacek, P., et al. Thermoplastic in situ placement requires better impregnated tapes and tows. In: *International SAMPE Technical Conference*. ISBN 9781934551127; 2012, p. 1–15.
- [48] Slange, T.K., Warnet, L.L., Grouve, W.J.B., Akkerman, R.. Influence of prepreg characteristics on stamp consolidation. *AIP Conference Proceedings* 2017;1896:30032.
- [49] Grouve, W.J.B., Warnet, L.L., Rietman, B., Visser, H.A., Akkerman, R.. Optimization of the tape placement process parameters for carbon-PPS composites. *Composites Part A: Applied Science and Manufacturing* 2013;50:44–53.
- [50] Leon, A., Argerich, C., Barasinski, A., Soccard, E., Chinesta, F. Effects of material and process parameters on in-situ consolidation. *International Journal of Material Forming* 2019;12(4):491–503.

Chapter 5

The Effect of Laser-Induced Deconsolidation on the Compaction Behavior of Thermoplastic Composite Tapes

The effects of laser-induced deconsolidation on the compaction process of CF/PEEK tapes were investigated. First, tapes with different degrees of deconsolidation were manufactured with the laser heater used in Chapter 3. This procedure resulted in samples with different waviness, thickness, void content and surface roughness values. Then, as-received and laser-deconsolidated tapes were compacted under two different temperature histories and four different pressure levels. Waviness induced by laser-deconsolidation vanished when the material was heated up to the glass transition temperature even at a very low compaction pressure. Unlike waviness; increased thickness, void content and surface roughness due to laser-deconsolidation remained between the glass transition and melting temperatures. After the melting temperature was exceeded, the effects of laser-deconsolidation were dependent on the applied pressure and initial degree of deconsolidation. The final surface roughness, thickness and degree of effective intimate contact were affected by the degree of laser-deconsolidation when a compaction pressure of less than 300 kPa was applied.

This chapter is based on: Çelik, O., Bussink, T., Peeters, D., Teuwen, J., Dransfeld, C., The effect of laser-induced deconsolidation on the compaction behavior of thermoplastic composite tapes. Composites Part A: Applied Science and Manufacturing, 106670, Volume 151, 2021.

5.1 Introduction

Laser-assisted fiber placement (LAFP) with in-situ consolidation (without a post-consolidation step such as an autoclave, oven or press) has been a focal point of research for composite manufacturing methods in the recent years. It offers precise and repeatable production of near net-shaped thermoplastic composite parts with minimum human intervention. Moreover, skipping the post-consolidation step has the potential for a great reduction in processing time and energy consumption. A typical LAFP system is demonstrated in Figure 5.1. Layers of thermoplastic composite material are joined by first heating via a laser heater pointed at the nip point between the incoming tape and underlying substrate and then, compacting with a silicone or metal roller.

The resulting part quality is highly dependent on the short (< 1 s) compaction phase of the process. Several phenomena such as intimate contact development [1–3], void compression [4] and tape deformation [5] take place during the time spent under the compaction roller. These phenomena play a significant role in determining the final mechanical properties, dimensions and porosity of the structure; therefore, it is crucial to have a deep understanding on the compaction behavior of the tape during LAFP.

As demonstrated in Figure 5.1, laser heating changes the micro- and meso-structure of the tape significantly. These changes have been termed as deconsolidation in the literature [6]. Specifically, the laser-deconsolidated tape has a higher waviness, roughness, thickness and volumetric void content than the as-received tape as shown in Chapter 3. The effects of deconsolidation on the compaction of the tape is important due to the limited compaction time during LAFP.

The effects of deconsolidation on the compaction behavior of the thermoplastic composite tapes have been investigated by only few researchers. Kok et al. focused on the influence of fiber decompaction at the tape surface due to laser heating [7]. They showed that laser irradiation may lead to a resin-poor layer at the tape surface and formulated an intimate contact model based on through-thickness impregnation of the dry fibers [8]. The model predicted the experimental results with limited success. The assumption of a one-dimensional problem domain may have led to oversimplification of the intimate contact development phenomenon. Later on, in Chapter 4 of this thesis, it was shown that due to the presence of dry fibers at the tape surface, a complete mechanical contact against the opposite surface may not eliminate interlaminar voids or ensure full bond strength development [3]. The concept of effective intimate contact, which is the ratio of the *resin* material in contact with the opposing surface to the whole projected surface area, was proposed. Experimental results suggested that effective intimate contact develops as a result of a combination of squeeze flow and percolation flow in both the thickness and fiber directions. In Chapter 3, the possible effects of other forms of deconsolidation such as waviness formation, void content increase and non-uniform thickness increase on the compaction of the tape were discussed. It was suggested that these effects should be considered for calculation of heat transfer, void compaction and effective intimate contact development. An experimental study which directly addresses the effect of deconsolidation during the compaction of thermoplastic plies is not present in the literature.

The objective of this study is therefore to understand the differences between the

compaction behavior of as-received and laser-deconsolidated tapes exposed to the same temperature and pressure history. To reach this goal, a two-step experimental procedure was performed. First, carbon fiber reinforced polyetheretherketone (CF/PEEK) tapes were deconsolidated using a Vertical-Cavity Surface-Emitting Laser (VCSEL) heater under conditions similar to the heating phase of LAFP. Then, samples from these tapes were compacted under two temperature histories with relatively fast heating/cooling rates, and four pressure levels. As-received tape samples were also compacted as reference. The effects of deconsolidation were studied with in-situ and ex-situ methods. The gap thickness and temperature were measured during the compaction experiments. Cross-sectional microscopy, effective intimate contact measurement and confocal microscopy were employed after the experiments.

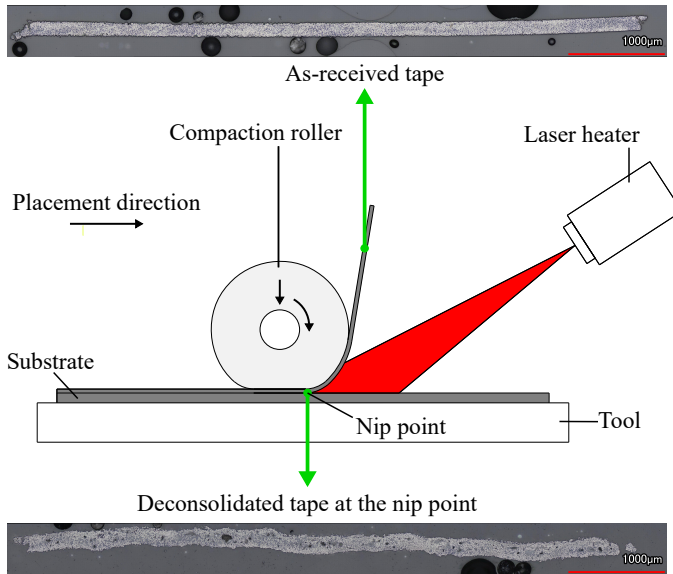


Figure 5.1. Working principle of a typical LAFP system with representative cross-sectional images demonstrating how laser heating can alter the micro-structure of the composite tape prior to the nip point.

5.2 Materials and Experimental Methods

5.2.1 Materials

The material used in this study was Toray TC1200 CF/PEEK slit in 6.35 mm-wide tapes. The nominal thickness of the as-received tape was 0.15 mm. The glass transition (T_g) and melting (T_m) temperatures of PEEK were reported as 143 °C and 343 °C, respectively [9].

5.2.2 Deconsolidation of As-received Tapes

An experimental setup was designed to deconsolidate CF/PEEK tapes under conditions similar to the heating phase of LAFP. Figure 5.2 demonstrates the setup and its components. A composite tape was attached to an aluminum tool using polyimide tapes at the ends and heated with a laser heater while the temperature at the tape surface was measured with a thermal camera.

A TRUMPF PPM411-12-980-24 laser module with a total output capacity of 2.4 kW was used to heat the surface of the composite tape. The device contains 12 heating zones which can be independently activated and adjusted to get a tailored heating profile. The heater was positioned so that the emitted laser beams were perpendicular to the plane the composite tape lies on. The distance between the laser heater and the tape was 5 cm.

Temperature on the tape surface during heating was measured with a FLIR A655sc long-wave infrared (LWIR) camera. The resolution of the detector of the camera was 640×480 pixels. The accuracy of the temperature measurement was $\pm 2^\circ\text{C}$ or $\pm 2\%$ (whichever is greater). The camera was calibrated in the range of $100\text{--}650^\circ\text{C}$.

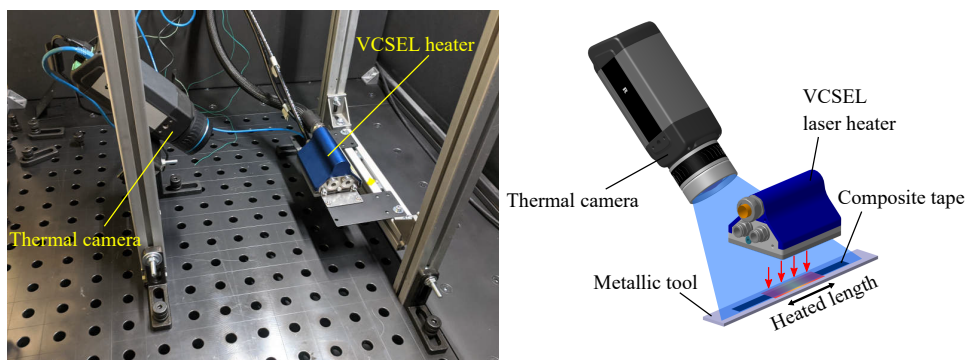


Figure 5.2. Experimental setup for laser-deconsolidation of composite tapes.

The specimens were deconsolidated at two different laser settings to obtain different degrees of deconsolidation and split into two groups based on the laser settings: highly and slightly laser-deconsolidated samples (HLD and SLD, respectively.). The laser settings used for each group of samples are shown in Table 5.1. The settings were determined so that the HLD samples reached an average temperature over the heated area significantly above the T_m , whereas the SLD samples reached an average temperature between T_g and T_m to limit the effects of deconsolidation. The high scatter in temperature at the tape surface is a result of the varying angle of incidence between the laser beams and the surface features caused by waviness formation during laser heating (Chapter 3).

5.2.3 Compaction of As-received and Deconsolidated Tapes

The as-received (ASR), SLD and HLD samples were compacted in a TA Instruments RSA-G2 Solids Analyzer. A compression fixture was installed on the instrument as

Table 5.1. Laser settings used in deconsolidation experiments.

Specimen group	Activated zones	Total power (W)	Time (ms)	Max. average temperature (°C)	Max. local temperature (°C)
Highly laser-deconsolidated (HLD)	1–11	550	800	395–511	448–566
Slightly laser-deconsolidated (SLD)	1–11	286	800	232–296	268–341

demonstrated in Figure 5.3. 6–7 mm long samples were extracted from the as-received and laser-deconsolidated tapes and placed between two 25 μm -thick Polyimide (Kapton) films to prevent damage to the compression platens. Following that, a heating/cooling cycle was applied on the samples under constant compressive force. The samples were compacted under constant compressive force for two reasons. Firstly, further deconsolidation during the heating or cooling phases of the compaction experiments was prevented by applying a compaction force. Secondly, application of compaction force during the whole temperature history allows one to observe the compaction behavior at different temperature ranges. This is especially important for the LAFP process, where the temperature of the incoming tape might drop below the melting temperature under the compaction roller [10].

5

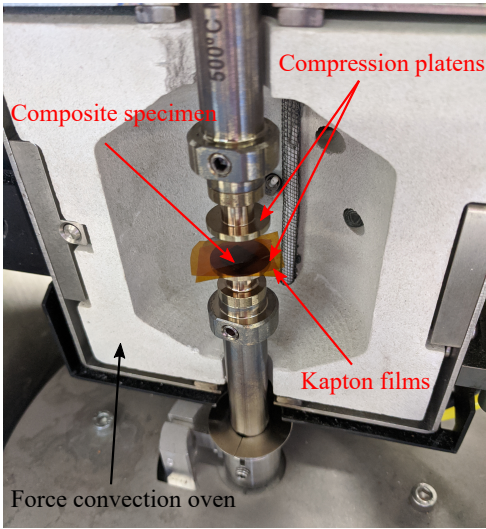


Figure 5.3. Experimental setup for compaction of composite tapes.

Two different compaction settings were used as shown in Table 5.2. The first group of samples was heated from 25 °C to the target temperature of 400 °C (above T_m) with a rate of 60 °C/min, held at that temperature for 20 s and cooled down to 25 °C with a rate of 60 °C/min. The experiments were repeated at four different pressure levels: 10, 50, 100 and 300 kPa. The compaction force was calculated for each experiment by multiplying the desired pressure and the initial projected area of each sample, and kept constant throughout the whole experiment. The second group of samples was heated from 25 °C

to the target temperature of 245 °C (between T_g and T_m). The heating/cooling rates and holding duration were the same with the previous set of experiments and the highest ones that could be achieved with the experimental set-up. These experiments were performed only at 300 kPa pressure.

The pressure values of the experiments above T_m were determined to cover a range between the minimum and maximum compaction forces which could be reliably achieved with the instrument. During the LAFP process, the pressure under the compaction roller is dependent on the roller geometry and material as well as the applied compaction force. A pressure of 300 kPa was reached by applying a compaction force of 100 N on a flat surface using a roller with a hardness of Shore A 60 and a diameter of 70 mm [3]; however, the same pressure was obtained for a compaction roller with a hardness of 20HA and a diameter of 80 mm when a compaction force of 800 N was applied [11]. Also, pressures lower than 300 kPa can be observed on convex surfaces [11].

Table 5.2. Parameters used in the compaction experiments.

Specimen group	Heating rate (°C/min)	Target temperature (°C)	Soak time (s)	Cooling rate (°C/min)	Max. thermocouple (°C)	Pressure (kPa)
Above T_m	60	400	20	60	363	10, 50, 100 and 300
Above T_g	60	245	20	60	200	300

The target temperature set in the instrument represents the temperature of the gas circulating in the convection oven. Due to the relatively fast heating/cooling cycle and the lack of time to equilibrate with the environment, the temperature of the objects between the compression platens differs from the gas temperature. To determine the actual sample temperature during the experiments, a 100 μ m-thick K-type thermocouple was placed between two Kapton films and compacted with the settings explained above. As shown in Figure 5.4, the temperature measured with the thermocouple lagged behind the programmed target temperature and reached 363 °C and 200 °C at its peak for the target temperatures of 400 and 245 °C, respectively. In this work, the temperature history measured with the thermocouple was used as the reference temperature throughout the compaction process.

Due to the presence of the Kapton tapes between the platens, the gap thickness measured during the experiments needed to be corrected to obtain the net gap thickness associated with the composite specimen. To do that, a reference experiment was performed with only two Kapton films between the compression platens before each experiment. The reference gap thickness was recorded during the compaction cycle. Three repetitions were performed for each degree of deconsolidation and temperature/pressure combination in Table 5.2 and the average reference gap thickness was calculated for each combination. Following that, the actual experiment including the composite tape was completed (also performed for three specimens). The average reference gap thickness was subtracted from the gap thickness of each actual experiment to obtain the net gap thickness. Finally, the three net gap thickness curves were aligned in the time axis and averaged to obtain a single net gap thickness curve for each combination of the degree of deconsolidation, temperature and pressure. These gap thickness curves are demonstrated in Figure 5.5.

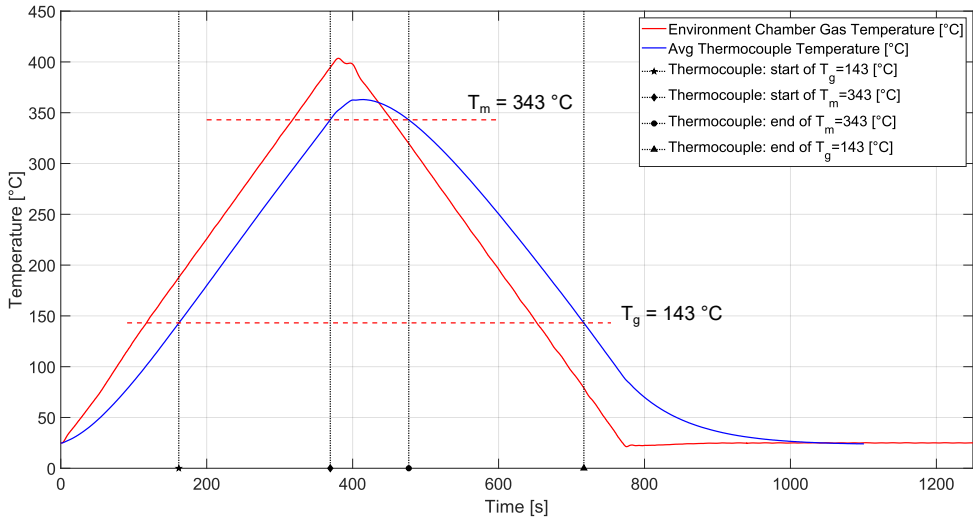


Figure 5.4. The gas temperature programmed in the software of the compaction set-up and the temperature measured with a thermocouple placed between two Kapton films.

5

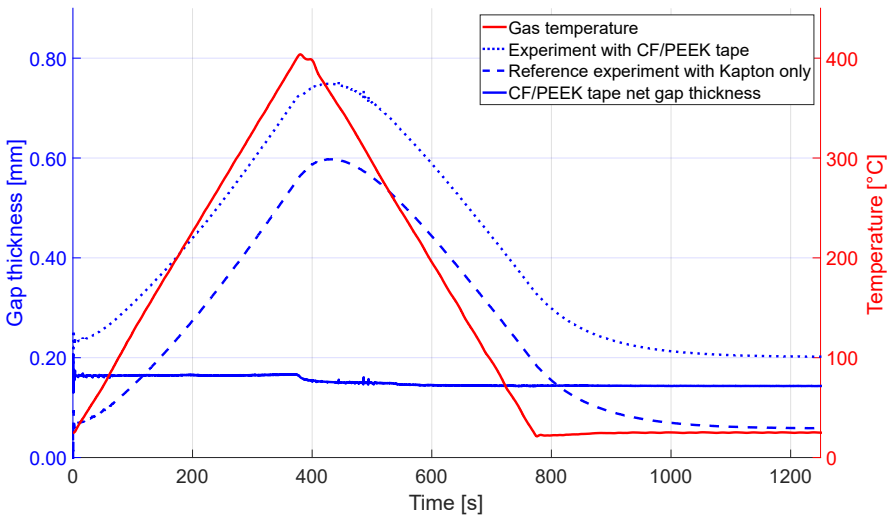


Figure 5.5. Representative gas temperature along with the corresponding gap thicknesses from the experiment with CF/PEEK tape, the reference experiment with Kapton tape only, and the calculated net gap thickness of the CF/PEEK sample.

5.2.4 Degree of Effective Intimate Contact

Degree of effective intimate contact (DEIC), which was defined as the amount of compacted resin at the tape surface, was measured using the methodology provided in Chapter 4. A Keyence VHX-2000 optical microscope equipped with a VH-Z100 lens was used to capture the whole surface of the specimens after the compaction tests. These images were converted to grayscale images and the grayscale histogram was used to segment the resin-rich areas from the rest as shown in Figure 4.5 and explained in Section 4.3.1. DEIC was calculated as the ratio of the resin-rich area to the whole area of the image.

5.2.5 Cross-sectional Microscopy

The final void content and thickness of the composite specimens after the compaction tests were determined by cross-sectional microscopy. Also, additional samples were cut from the composite tapes to represent the state of the specimens prior to the compaction tests. The specimens were embedded into slow-curing mounting epoxy (Struers Epofix) and ground/polished in a Struers Tegramin-20 specimen preparation equipment. A Keyence VK-X1000 Laser Scanning Confocal Microscope (LSCM) was used to obtain the cross-sectional images. To capture the whole tape width with high resolution, several images were taken and stitched with the $20\times$ lens in the Focus Variation method. The thickness of each tape was determined using the native software of the instrument. The void content of each tape was manually measured using ImageJ software.

5.2.6 Roughness and Waviness

A Keyence VK-X1000 LSCM was used to measure surface roughness and waviness of each specimen before and after the compaction experiments. Three sections (top, middle and bottom) spanning the whole width of the top (laser-irradiated) surface of each specimens were captured. At each section, multiple images were taken in the tape width direction using the $20\times$ lens and stitched together to form a single confocal image. The size of each section in the fiber direction was the height of a single image, which was approximately $525\mu\text{m}$. 11 primary profiles were extracted from each section.

The primary profiles were filtered to distinguish the roughness and waviness profiles following the ISO 4287 [12] and ISO 4288 [13] standards. The filter required the definition of the cut-off wavelengths λ_s , λ_c and λ_f shown in Figure 5.6. To obtain the roughness profile, λ_s and λ_c were set to 0 mm and 0.8 mm, respectively. To separate the waviness profile from the larger-wavelength components of the surface profile; λ_f was set to 2.5 mm. From this data, root mean square (RMS) roughness (R_q) and waviness (W_q) were calculated.

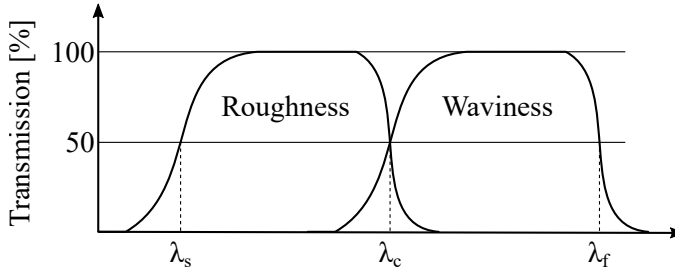


Figure 5.6. Transmission characteristic of roughness and waviness profiles with the demonstration of cut-off wavelengths λ_s , λ_c and λ_f . Reproduced from [12]

5.3 Results

5.3.1 Effects of Laser-Deconsolidation on the Structure of the Tape before Compaction

The laser-deconsolidated tapes had significantly different micro-structures compared to the as-received tapes due to deconsolidation mechanisms such as fiber decompaction, void growth, specific volume change and residual stresses (Chapter 3). Figure 5.7 demonstrates representative cross-sectional micrographs of the ASR, SLD and HLD specimens. As shown in Figure 5.7a, the overall shape of the ASR tapes was flat. There was no resin-rich layer at the tape surface; however, the fibers at the surfaces were not detached from the body of the tape. A slight variation in fiber volume fraction was observed throughout the tape but no resin pockets or dry fibers were present. The SLD tapes demonstrated in Figure 5.7b, however, contained some forms of deconsolidation such as waviness and a few voids. Such features were rather localized and a major portion of the tape width was unaffected by the laser heating. The most severe signs of deconsolidation were observed in the HLD tapes as pointed out in Figure 5.7c. The tape was warped and the thickness of the tape was irregular. The void content was much higher than the SLD tapes. Fibers detached from the tape surface were widespread.

Using the cross-sectional micrographs of each sample, the void content of the ASR, SLD and HLD tapes was calculated. Figure 5.8a shows the effect of degree of deconsolidation on the void content for samples prepared for experiments at different pressure levels. The ASR tapes had a very low void content (<1 %). However, laser heating resulted in a significant increase in the void content even when the average surface temperature was below T_m as the SLD tapes had an average void content of 2.8 %. The void content of the HLD samples was even higher (4.6 % on average), confirming the qualitative observations based on the cross-sectional images.

Laser-deconsolidation also led to an increase in surface roughness as shown in Figure 5.9a. As the degree of deconsolidation increased, the surface roughness increased. The difference between the average roughness of the ASR (3.7 μm) and SLD (5.7 μm) tapes were around 2 μm . The average roughness of the HLD tapes (10 μm) was much higher (4.3 μm) than the SLD tapes.

In addition to the local features at the surface, features of the tape at a larger scale

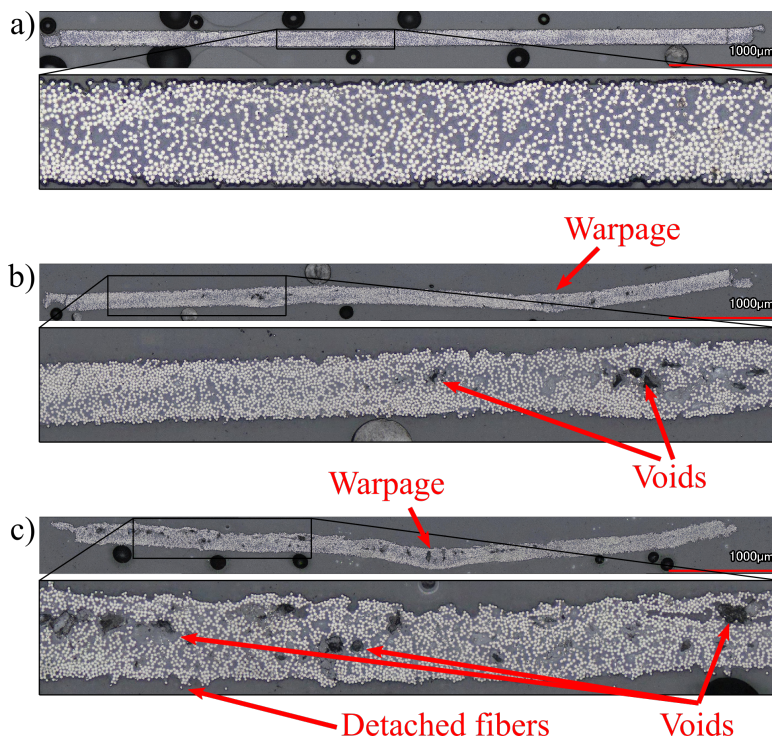


Figure 5.7. Representative cross-sectional images of a) as-received, b) slightly laser-deconsolidated, and c) highly laser-deconsolidated samples.

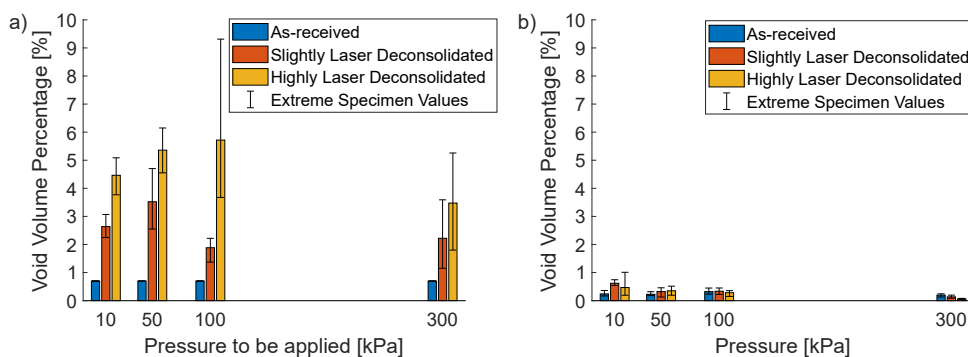


Figure 5.8. a) Void content of the as-received (ASR), slightly laser-deconsolidated (SLD), and highly laser-deconsolidated (HLD) samples prior to the experiments with a maximum temperature of 363 °C and pressure levels of 10, 50, 100 and 300 kPa. b) Void content of the samples after being subjected to the respective compaction pressure. The data for ASR tapes in a) is reproduced from Chapter 3.

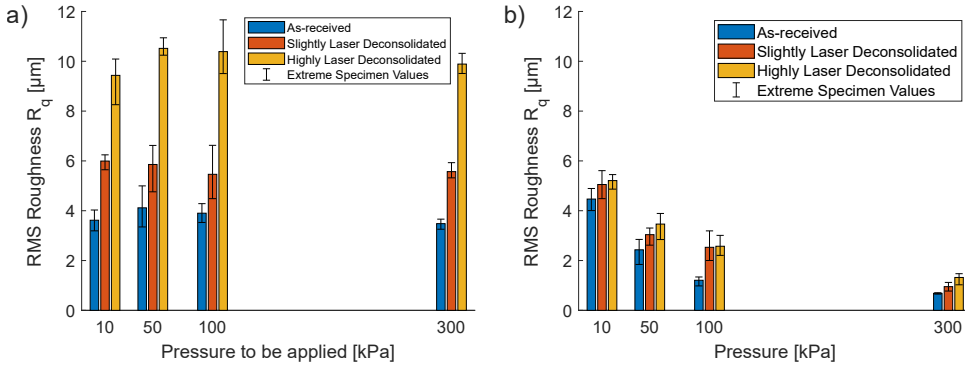


Figure 5.9. a) RMS roughness of the as-received (ASR), slightly laser-deconsolidated (SLD), and highly laser-deconsolidated (HLD) samples prior to the experiments with a maximum temperature of 363 °C and pressure levels of 10, 50, 100 and 300 kPa. b) RMS roughness of the samples after being subjected to the respective compaction pressure.

also varied as a result of the warpage and motion of the fiber bundles after laser heating. This can be seen in the RMS waviness of each degree of deconsolidation presented in Figure 5.10a. The ASR tape was practically flat with a very low waviness value, 1 μm . As the degree of deconsolidation increased, the waviness increased significantly. On average, the SLD and HLD tapes had an RMS waviness of 8.2 μm and 13.7 μm , respectively.

The average initial DEIC of the ASR tapes was found to be 5.9 %. Unfortunately, it was not possible to measure the initial DEIC of the laser-deconsolidated samples. The surface micrographs were out-of-focus at many locations due to the high amount of out-of-plane deformation. Considering the increased roughness and detached fibers at the surface due to laser-deconsolidation (shown in Figure 5.7), it can be expected that the laser-deconsolidated samples have a lower initial DEIC than the ASR samples.

5.3.2 Compaction Behavior of the As-received and Deconsolidated Tapes

In-situ Gap Thickness

In-situ gap thickness of the ASR, SLD and HLD tapes that were heated up to 363 °C were grouped by the applied pressure and presented with the accompanying temperature history in Figure 5.11a-d. A common behavior was observed at each pressure level. A significant drop in gap thickness was observed around T_g for the SLD and HLD tapes at all pressures and the ASR tape at 10 kPa. This sudden decrease was followed by a plateau until T_m . When T_m was exceeded, a second large decrease in gap thickness was observed for all samples at each pressure. After this point, the gap thickness decreased slightly further and then stayed practically constant. Based on the overall behavior of the gap thickness curves, three distinct characteristic points were defined and used to compare the samples quantitatively. As demonstrated in Figure 5.12, these points are the initial

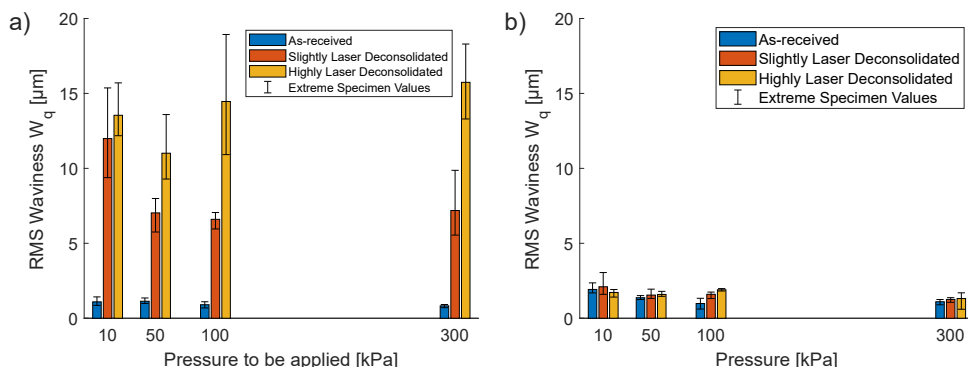


Figure 5.10. a) RMS waviness of the as-received (ASR), slightly laser-deconsolidated (SLD), and highly laser-deconsolidated (HLD) samples prior to the experiments with a maximum temperature of 363 °C and pressure levels of 10, 50, 100 and 300 kPa. b) RMS waviness of the samples after being subjected to the respective compaction pressure.

5

gap, gap after T_g and the final gap.

Figure 5.13a shows the initial gap thickness of the ASR, SLD and HLD tapes. The degree of deconsolidation clearly affected the initial gap thickness at each pressure level. At the pressure of 10 kPa, the initial gap thickness of the ASR, SLD and HLD tapes were around 190, 260 and 320 μm, respectively. It is thought that the low pressure was not sufficient to flatten the overall form of the tape, which was a result of the warpage that occurred during sample extraction. As the pressure was increased to 50 kPa, the warpage was eliminated and the initial gap thickness of the tapes decreased to ~150, 200 and 300 μm for the ASR, SLD and HLD tapes, respectively. Experiments performed at a pressure of 100 kPa resulted in a slight decrease in the initial gap thickness for ASR and SLD tapes but the difference was small and stayed within the measurement accuracy of the initial gap thicknesses at 50 kPa. At 300 kPa, the initial gap thickness did not change significantly for the ASR and SLD tapes but reduced to ~240 μm for the HLD tapes.

Figure 5.13b shows the reduced gap thickness after the T_g . A significant reduction in gap thickness was observed for the HLD samples, ranging between 80–150 μm at each pressure level. The gap thickness of the SLD tapes decreased less, within a range of 20–50 μm. The gap thickness of the ASR samples reduced significantly at only 10 kPa and it was around 30 μm. The reduction was below 10 μm for the pressure levels of 50 and 100 kPa and zero at 300 kPa. The SLD and HLD samples had a higher gap thickness than the ASR samples at every pressure level. However, the degree of deconsolidation did not have a significant effect on the gap thickness after T_g for the laser-deconsolidated samples.

Figure 5.13c and d show the final gap thickness and the thickness from the cross-sectional images, respectively, for all samples. It can be seen that the values obtained via the two methods agree with each other very well in general. Only at 10 kPa, the gap length was slightly higher than the thickness, which can be explained by the effect of

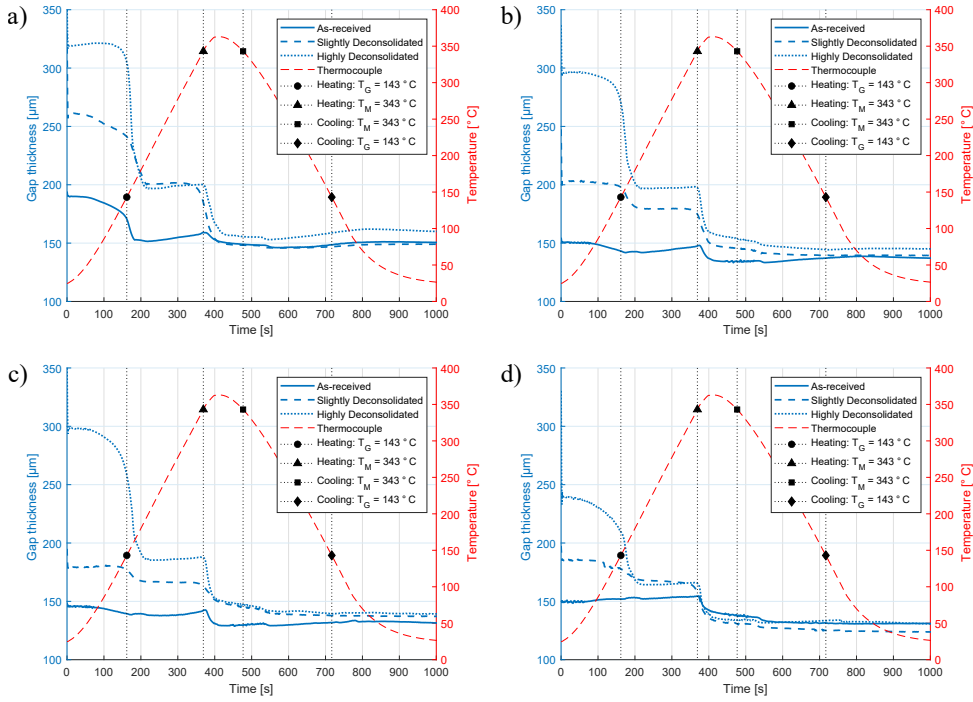


Figure 5.11. In-situ gap thickness of ASR, SLD and HLD tapes heated up to 363 °C under the pressure of a) 10 kPa, b) 50 kPa, c) 100 kPa and d) 300 kPa. The temperature histories are also added and T_g and T_m during heating and cooling are marked.

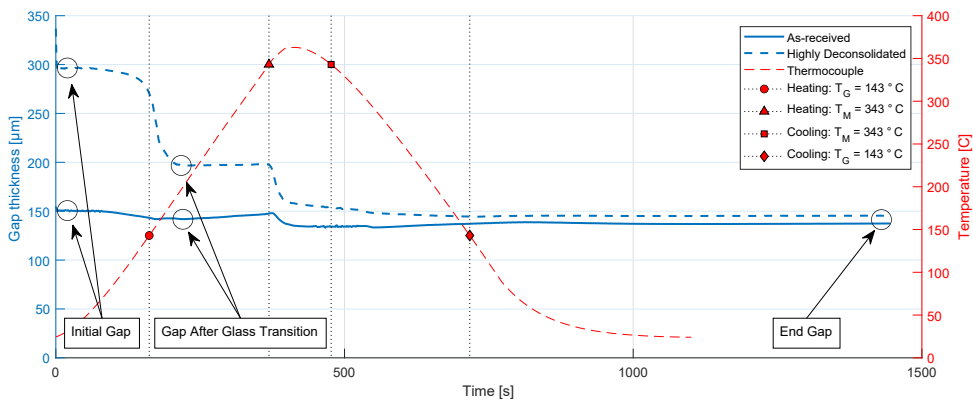


Figure 5.12. Characteristic points on the gap thickness curves that were selected to compare the samples quantitatively.

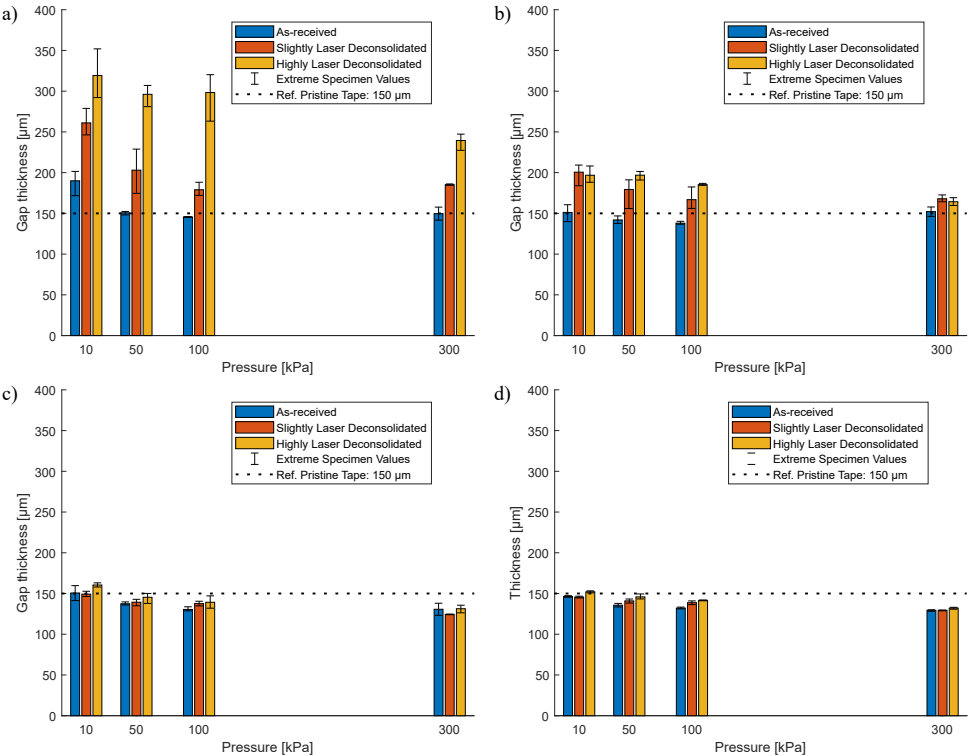


Figure 5.13. a) The initial gap thickness, b) gap thickness after T_g , c) final gap thickness and d) thickness from cross-sectional microscopy for the ASR, SLD and HLD tapes subjected to different pressures with a maximum temperature of 363 °C.

the overall form of the tape due to the lack of sufficient pressure to keep the tape flat. A comparison of Figure 5.13c and Figure 5.13b reveals that the SLD and HLD tapes were compacted significantly from their thickness at T_g at all pressures, whereas this was the case for the ASR tape at only 300 kPa. Figure 5.13d demonstrates that the thickness of all the samples were below the nominal thickness of the ASR tape with the exception of the HLD tape at 10 kPa. The effect of the degree of deconsolidation was minor as the average final thickness of the ASR and HLD tapes differed around 10 μm at most.

The in-situ gap thickness measurements from the experiments with a maximum temperature of 200 °C are shown in Figure 5.14. Figure 5.14a demonstrates that the gap thickness of the SLD and HLD samples dropped significantly at T_g as in the previous experiments (shown in Figure 5.11). The ASR tape did not go through significant changes as it did not exceed T_m . Figure 5.14b–d show that the gap thickness of the tapes in the experiments with 200 and 363 °C maximum temperature were similar to each other until the T_m was reached during the 363 °C experiments. Since the samples from the 200 °C experiments cooled down below T_g shortly after that point (at around 400 s), it can be assumed that their microstructure represents the state of the tape just after T_g .

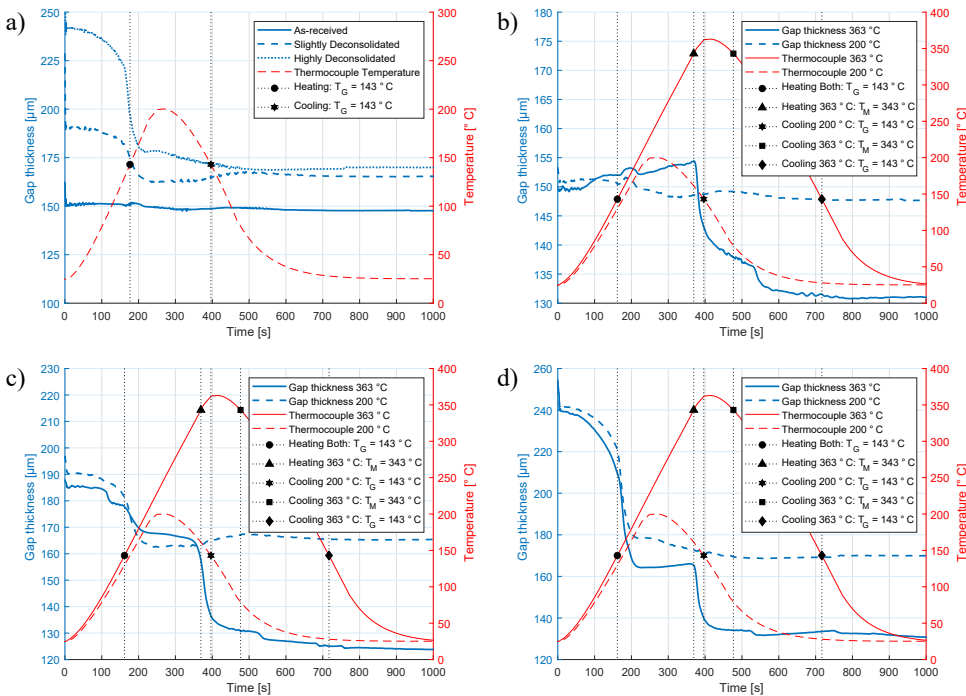


Figure 5.14. In-situ gap thickness of a) ASR, SLD and HLD tapes heated up to 200 °C under the pressure of 300 kPa and comparison between b) ASR tapes, c) SLD tapes and d) HLD tapes heated up to 200 °C and 363 °C under the pressure of 300 kPa.

Morphological Analysis

Figure 5.15 shows the representative cross-sections of the pristine ASR and HLD specimens and their states after the compaction experiments at a pressure of 300 kPa. Figure 5.15b shows that the micro-structure of the ASR tapes changed minimally from the initial state (Figure 5.15a) when subjected to a maximum temperature of 200 °C. The surface features of the tape did not flatten and the thickness did not change much. When compacted above T_m , the tape surface was much smoother and the thickness decreased, as shown in Figure 5.15c.

The effects of the compaction treatments just above T_g and above T_m was much more pronounced for the HLD tapes. Samples treated at just above T_g (Figure 5.15d) were much flatter than their initial states (Figure 5.15a) in the meso-scale. The waviness and thickness variations were mostly eliminated. However, the tape surface was still rough and voids were present within the tape. When the samples were compacted above T_m , the surface was smoothened, voids were compacted and thickness was reduced (Figure 5.15e), leading to a state similar to the ASR samples compacted under the same conditions.

5

Void Content

The final void content of the samples which were compacted above T_m is shown in Figure 5.8b. At 10 kPa, the SLD samples had a slightly higher average void content than the ASR samples. However, a relatively high scatter was observed for the HLD samples, ranging between 0.1–1 %. At higher pressures, all samples had a similar average final void content between 0.1–0.4 %. It should be noted that even at 10 kPa, the final void content was below 1 %, which is considered a low and tolerable value in industry applications [14].

Figure 5.16 shows the final void content of the samples subjected to a maximum temperature of 200 and 363 °C under a pressure of 300 kPa. Compaction just above the T_g led to reduction of voids, as the void content of ASR, SLD and HLD samples decreased for 0.4, 0.7 and 1.6 % on average. However, the voids were not completely eliminated. The degree of deconsolidation had an effect on the void content just above T_g and the SLD and HLD tapes had a significantly higher void content than the ASR tapes. However, when the T_m was exceeded, the compaction cycle was sufficient to eliminate the voids and all three degrees of deconsolidation resulted in the same, very low amount of void content.

Effective Intimate Contact

The final degree of effective intimate contact (DEIC) of the ASR, SLD and HLD tapes subjected to 363 °C is shown in Figure 5.17. The effect of both the pressure and the degree of deconsolidation can be observed in the results. An increase in the applied pressure increased the DEIC for all degrees of deconsolidation. Even at the lowest pressure setting (10 kPa), the DEIC was significant (45–50 % for the ASR tape and 35–45 % for the SLD and HLD tapes) for all samples. At the highest pressure (300 kPa), all samples reached an average DEIC of ~85 %. The effect of the degree of deconsolidation was apparent at

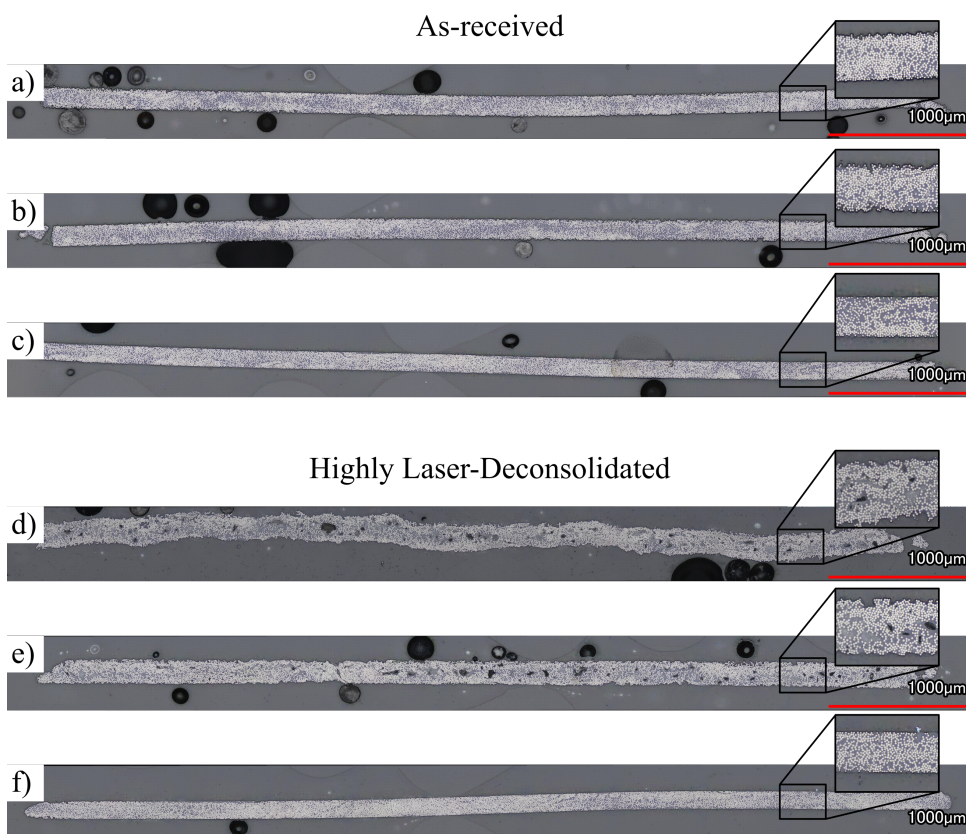


Figure 5.15. Representative cross-sectional images of the ASR and HLD tapes before the compaction experiments (a) and d)), after being subjected to a maximum temperature of 200 °C and 300 kPa (b) and e)) and after being subjected to a maximum temperature of 363 °C and 300 kPa. a)–b) and d)–e) are from different locations of the same specimen.

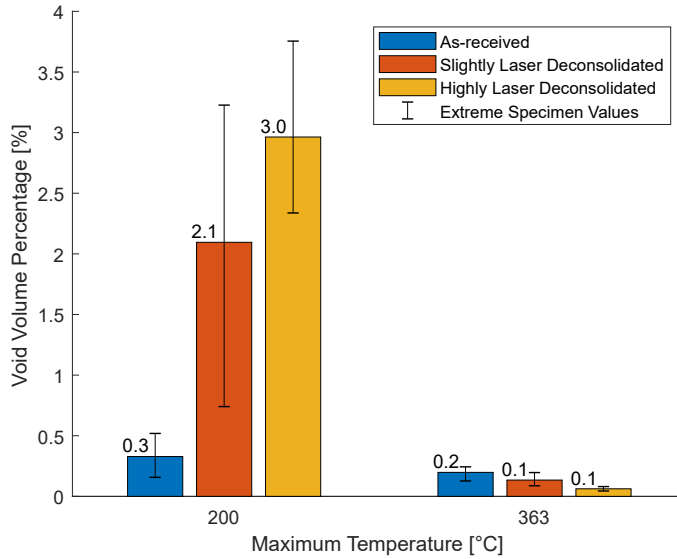


Figure 5.16. Final void content of the ASR, SLD and HLD specimens subjected to a maximum temperature of 200 and 363 °C and pressure of 300 kPa. Initial average void content of ASR: 0.7 %, SLD: 2.8 %, HLD: 4.6 %.

pressures below 300 kPa. The average DEIC decreased as the degree of deconsolidation increased.

Figure 5.18 shows the final DEIC of the samples subjected to a maximum temperature of 200 and 363 °C under a pressure of 300 kPa. Unlike the samples that were compacted above T_m , the samples compacted just above T_g had a very low final DEIC. Also, the degree of deconsolidation did not affect the DEIC just after T_g .

Surface Roughness

The final RMS roughness of the samples subjected to a maximum temperature of 363 °C is shown in Figure 5.9b. The degree of deconsolidation had an effect at every pressure level. The mean roughness of the SLD and HLD tapes was higher than the ASR tapes. The HLD samples were slightly rougher than the SLD samples on average; however, due to scatter, no clear distinction can be made. The effect of pressure was also apparent for all degrees of deconsolidation. As the pressure increased, the roughness decreased. At 10 kPa, the roughness of the ASR tape was slightly higher than its initial value shown in Figure 5.9a; however, the roughness of the laser-deconsolidated tapes, especially the HLD ones, decreased significantly.

Figure 5.19 shows the final RMS roughness of the samples subjected to a maximum temperature of 200 and 363 °C under a pressure of 300 kPa. During the 200 °C experiments, the surface features of the tapes were not flattened as much as the 363 °C experiments, which is shown by the higher roughness values. For the samples subjected to 200 °C, the roughness increased as the degree of deconsolidation increased. It should

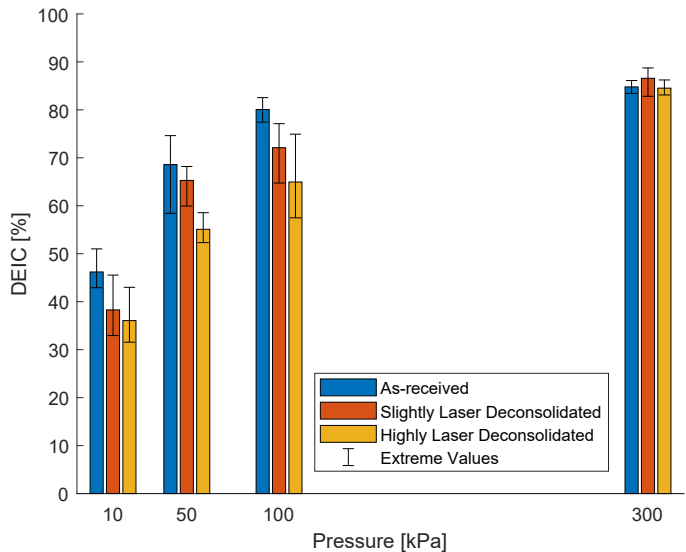


Figure 5.17. The final degree of effective intimate contact for the ASR, SLD and HLD samples subjected to a maximum temperature of 363 °C.

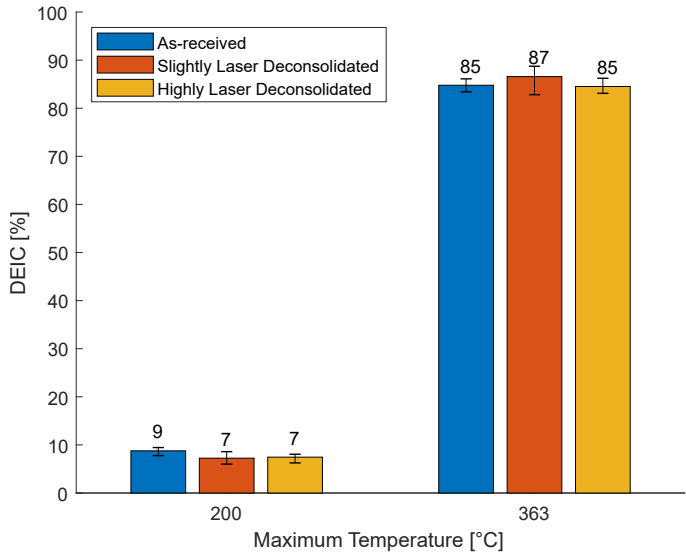


Figure 5.18. The final degree of effective intimate contact for the ASR, SLD and HLD samples subjected to a pressure of 300 kPa and a maximum temperature of 200 °C and 363 °C. The initial average DEIC of ASR: 5.9 %, SLD and HLD are not available but expected to be lower than the DEIC of ASR.

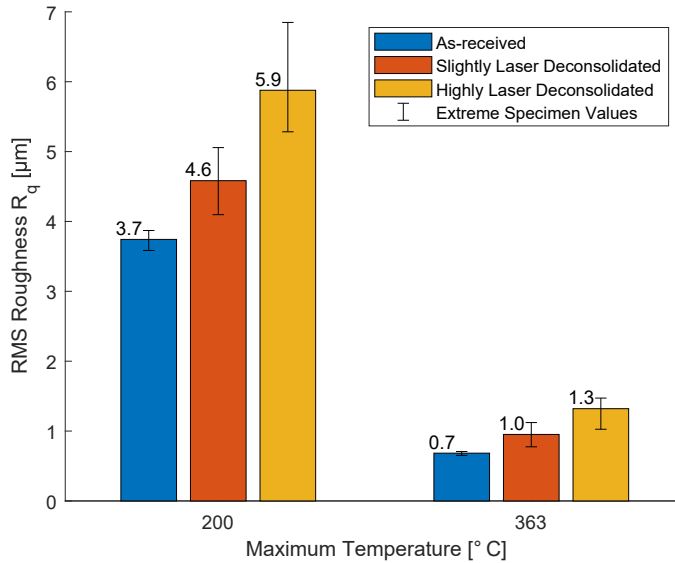


Figure 5.19. The final RMS roughness of the ASR, SLD and HLD samples subjected to a pressure of 300 kPa and a maximum temperature of 200 °C and 363 °C. Initial average RMS roughness of ASR: 3.7 μm, SLD: 5.7 μm, HLD: 10.0 μm.

be noted that the roughness of the ASR tapes did not change significantly from the initial value, whereas a reduction of 1.1 μm and 4.1 μm was observed for the SLD and HLD tapes, respectively. All of the samples which were subjected to 363 °C reached a roughness which is smaller than the initial roughness of the ASR tape. The difference between the degrees of deconsolidation was much less compared to the samples subjected to a maximum temperature of 200 °C.

Waviness

The final RMS waviness of the samples subjected to a maximum temperature of 363 °C is shown in Figure 5.10b. It can be seen that all of the samples had a significantly reduced waviness at the end of the experiments compared to their initial waviness (shown in Figure 5.10a). The degree of deconsolidation and pressure seem not to have a significant effect on the final waviness. Only at 10 kPa, the waviness of the ASR tape was slightly higher than its initial value.

Figure 5.20 compares the final RMS waviness of the samples subjected to a maximum temperature of 200 and 363 °C under the pressure of 300 kPa. Confirming the micrographs in Figure 5.15, the low RMS waviness values for the samples subjected to 200 °C show the flattening of meso-scale features of the tape surface at T_g . Past the T_g , the SLD and HLD samples had slightly more waviness than the ASR tapes; however, the difference was minute. The waviness reduced a bit further for all samples subjected to 363 °C and the degree of deconsolidation did not affect the results.

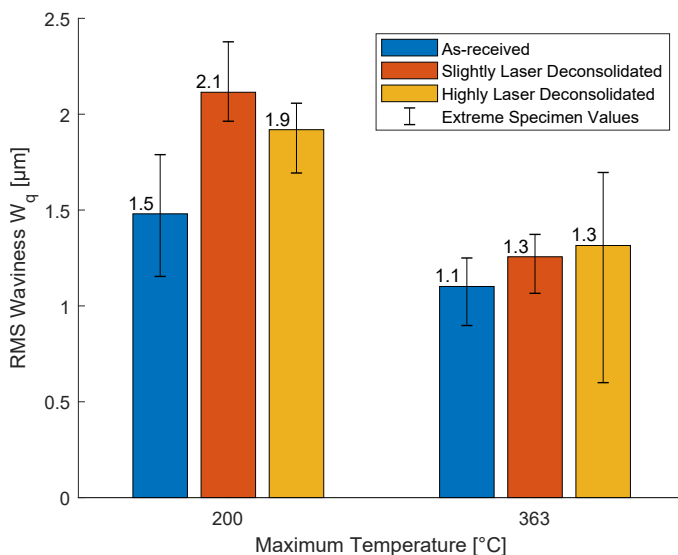


Figure 5.20. The final RMS waviness of the ASR, SLD and HLD samples subjected to a pressure of 300 kPa and a maximum temperature of 200 °C and 363 °C. Initial average RMS waviness of ASR: 1 μm, SLD: 8.2 μm, HLD: 13.7 μm.

5.4 Discussion

As explained in Section 5.3.1, laser-deconsolidation increases the void content, roughness and waviness of the tape. This study shows that such micro-structural changes affect the compaction process of the thermoplastic composite tapes in a number of ways. The effects can be grouped under three temperature ranges: between the room temperature and T_g , between T_g and T_m and above T_m . The severity of the effects varies in each temperature range.

At room temperature, the waviness of the samples and the thickness increase induced by void growth and fiber decompaction due to laser-deconsolidation were the main reasons of the difference in the gap thickness shown in Figures 5.11 and 5.14. The sudden decrease in the gap thickness when the T_g was exceeded suggests that the tapes were significantly deformed even if the resin was not in the molten state. The cross-sectional micrographs of the HLD samples shown in Figure 5.15e and the final waviness values of the samples subjected to a maximum temperature of 200 °C reported in Figure 5.20 suggest that the waviness was eliminated at the T_g . Unlike waviness, the voids and surface roughness were reduced but not completely eliminated (shown in Figures 5.16 and 5.19, respectively). At the T_g , the storage modulus of CF/PEEK decreases significantly and PEEK transforms into the rubbery state [15]. This transition is sufficient to flatten the meso-scale features of the tape even under very low pressures but fails to fill in the voids or cause them to migrate out of the tape completely, or establish effective intimate contact at the surface.

Between the T_g and T_m , the in-situ gap thickness measurements in Figure 5.11 show

no sign of change in the micro-structure of the as-received and deconsolidated tapes regardless of the applied compaction pressure. It is thought that the void content and surface roughness of the tapes just above the T_g stay almost constant in this phase since the change of the gap thickness is on the order of few microns. Thus, it can be stated that the microscopic effects of laser-deconsolidation cannot be completely eliminated if the resin is not in a molten state.

When the T_m was exceeded during compaction, the difference between the in-situ gap thickness curves of the as-received and laser-deconsolidated tapes decreased first rapidly, then gradually as shown in Figure 5.11. It is thought that the decrease in the difference is dominated by void compaction, as the trend in gap thickness shows resemblance with the calculated decrease of the void content in a tape with a void content of 2% and a void spacing smaller than 4 mm [4]. Another supporting aspect is that the size of the large voids are larger than the surface asperities after the T_g as shown in Figure 5.15e. As depicted in Figure 5.8b and Figure 5.15f, the majority of these voids were compacted. Along with void compaction, effective intimate contact was also established due to flow of the molten polymer to the tape surface, as demonstrated in Figure 5.17.

Among the abovementioned effects of laser-deconsolidation, the gap thickness after T_g (Figure 5.13b), RMS roughness (Figure 5.9b) and DEIC (Figure 5.17) showed dependence to the level of applied pressure. Below a pressure of 300 kPa, the influence of laser-deconsolidation was apparent in terms of an increased thickness after T_g , increased RMS roughness, and decreased DEIC. In [3], it is reported that a compaction pressure above 300 kPa can be reached even with low levels of compaction force on flat surfaces. However, the pressure under the compaction roller is determined by the mechanical properties of the roller and softer rubbers might require higher compaction forces to reach that pressure level. Also, moulds with non-flat surfaces have been increasingly used, as LAFP can be used to manufacture structures such as fuselage panels [16], variable-stiffness wingboxes [17] or pressure vessels [18]. During the material deposition on these surfaces, a reduction of the compaction pressure might occur between the contact points of concave surfaces [19] or the roller not conforming with the complete tow at corners [17]. It is suggested that laser-deconsolidation should be especially considered for such applications, as the regions with decreased pressure are susceptible to its effects.

Recent works showed that intimate contact can develop significantly between T_g and T_m for CF/PEEK laminates manufactured with LAFP [20] (Chapter 6) and CF/PEKK laminates manufactured with out-of-autoclave consolidation [21]. This was not the case during the compaction experiments performed at a maximum temperature of 200 °C, as shown in Figure 5.18. Two reasons can be identified for the difference between the experimental results and the literature. The first one is the temperature level reached during compaction. In [20], the nip point temperature was between 310–330 °C, whereas in [21], the CF/PEKK composite, whose T_m was 335 °C, was heated to 230 °C. In both studies, the maximum temperature was closer to the T_m of the material than it was in this study, which might have allowed more deformation of the surface asperities. The second reason concerns the scale of the surface deformation required for the development of intimate contact. So far, the existing squeeze flow-based intimate contact models [1, 2] considered the intimate contact phenomenon to occur at the scale of the *roughness* profile of the surface. However, Figure 5.15e shows that it is the *waviness* profile of the tape

which deforms significantly past the T_g . Such a result suggests that flattening of the waviness of the tape plays a role in intimate contact development.

The compaction behavior of the laser-deconsolidated tapes during the experiments leads to additional novel insights for the compaction phase of the actual LAFP process. Firstly, the significant reduction of laser-induced waviness above the T_g means that pressure variation along the width of the tape due to local contact of the tape–substrate and tape–compaction roller at the peaks and valleys of the *waviness* profile can be neglected since the temperature of the tape usually exceeds the T_g . Nevertheless, the laser-induced voids and surface roughness are expected to be present above the T_g and might play a role in the final quality of the part. Given that the tape might be compacted between the T_g and T_m during LAFP due to rapid heat dissipation [10], several phenomena would be affected by this micro-structural difference. Firstly, the amount of voids that need to be compacted can be an order of magnitude higher than the ASR tape, as suggested by Figure 5.16. This is crucial for the calculation of the final void content since the void content at the beginning of compaction is an important parameter for void filling models [4, 5]. Additionally, heat transfer mechanisms during the compaction phase are expected to be influenced by the difference between the as-received and laser-deconsolidated states. As shown in Figure 5.13b, the laser-deconsolidated samples were thicker than the as-received tapes significantly: ~30 % at pressures below 300 kPa and ~15 % at 300 kPa. Also, the voids and the rough tape surface would increase the intra- and inter-layer thermal resistance. These effects would influence the temperature gradient within the tape and the heat flux between the tape and surrounding bodies (the compaction roller and substrate) and should be considered for a more accurate analysis of the temperature history during the compaction phase of LAFP. Finally, if sufficient dwell time is allowed above T_m , the voids and surface roughness due to laser-deconsolidation can be remedied. During LAFP, raising the tape temperature prior to the nip point high enough so that it stays above the T_m at the beginning of compaction can be a viable option to reduce the effects of laser-deconsolidation. However, it should be ensured that the temperature of the newly placed tape is lower than the T_g at the roller exit (i.e. by means of active cooling systems such as convective air cooling, a secondary cooling roller or water cooling for the compaction roller [22]) so that further deconsolidation is prevented during the cooling phase.

The results presented in this work provide important insight that can be reflected to the actual LAFP process; however, it should be noted that the laser-deconsolidation and compaction experiments presented in this work may deviate from the heating and compaction phases of the LAFP process. Firstly, during the laser-deconsolidation experiments explained in Section 5.2.2, the CF/PEEK tapes were heated in a static setting. In an actual LAFP process, the incoming tape moves across a fixed laser-illuminated zone with the programmed placement speed as shown in Figure 5.1. This might change the through-thickness temperature gradient and hence, the extent of the effects of deconsolidation in the thickness direction. In the static setup, the heat can diffuse much more towards the non-irradiated surface of the tape and lead to more deconsolidation. Considering the difference in through-thickness temperature gradient, it can be stated that the HLD specimens represent a worst-case scenario for the state of the tape at the nip point in an actual LAFP process. Moreover, one should be aware of the fact that the

time spent at temperatures near the T_m of the material during the compaction experiments (although it was shorter than conventional composite processing times, which is on the order of several minutes) was significantly longer than the actual compaction phase of the LAFP process. As a result, the effects of the degree of deconsolidation on surface roughness, DEIC and void content can be even more pronounced during the actual LAFP process. In terms of the compaction time, the results from the samples which were subjected to a maximum temperature of 363 °C represent the best-case scenario for LAFP.

5.5 Conclusion

This study investigates the effects of laser-deconsolidation on the compaction process of CF/PEEK tapes experimentally. A two-step experimental procedure was performed. In the first step, a VCSEL heater was utilized to deconsolidate composite tapes under conditions similar to the heating phase of LAFP. Samples with two degrees of deconsolidation, which differed by the surface roughness, waviness and void content from the as-received tapes, were obtained using two different laser power settings. In the second step of experiments, the as-received and laser-deconsolidated tapes were compacted under different temperature and pressure settings. In-situ measurement of the gap thickness during compaction and ex-situ measurement of surface profile, degree of effective intimate contact and void content were used to assess the effects of laser-deconsolidation.

The results have shown that waviness induced by laser-deconsolidation vanishes when the material is heated up to the glass transition temperature even at a very low compaction pressure. This suggests that the compaction phase of LAFP would not be affected by the meso-scale deformations in the tape due to laser heating since the material is usually heated above its glass transition temperature. Unlike waviness; increased thickness, void content and surface roughness due to laser-deconsolidation remained between the glass transition and melting temperatures. These forms of deconsolidation were removed only above the melting temperature. This shows the importance of increasing the temperature of the material before the nip point high enough so that it stays above the melting temperature for a duration under the compaction roller, provided that it is cooled down below the glass transition temperature at the roller exit. Applied pressure also plays a significant role in the final properties of the compacted tapes. The final surface roughness and degree of effective intimate contact were affected by the laser-deconsolidation when a compaction pressure less than 300 kPa was applied. For future work, it is suggested that the effects of laser-deconsolidation are considered in process models, especially for process settings which do not ensure that the tape stays above the melting temperature under the compaction roller.

References

- [1] Lee, W.I., Springer, G.S.. A Model of the Manufacturing Process of Thermoplastic Matrix Composites. *Journal of Composite Materials* 1987;21(11):1017–1055.

- [2] Yang, F., Pitchumani, R.. A fractal Cantor set based description of interlaminar contact evolution during thermoplastic composites processing. *Journal of Materials Science* 2001;36(19):4661–4671.
- [3] Çelik, O., Peeters, D., Dransfeld, C., Teuwen, J.. Intimate contact development during laser assisted fiber placement: Microstructure and effect of process parameters. *Composites Part A: Applied Science and Manufacturing* 2020;134.
- [4] Simacek, P., Advani, S.G., Gruber, M.B., Jensen, B.. A non-local void filling model to describe its dynamics during processing thermoplastic composites. *Composites Part A: Applied Science and Manufacturing* 2013;46(1):154–165.
- [5] Pitchumani, R., Ranganathan, S., Don, R.C., Gillespie, J.W., Lamontia, M.A.. Analysis of Transport Phenomena Governing Interfacial Bonding and Void Dynamics During Thermoplastic Tow-placement. *International Journal of Heat and Mass Transfer* 1996;39(9):1883–1897.
- [6] Henninger, F., Ye, L., Friedrich, K.. Deconsolidation behaviour of glass fibre-polyamide 12 composite sheet material during post-processing. *Plastics, Rubber and Composites Processing and Applications* 1998;27(6):287–292.
- [7] Kok, T., Grouve, W.J.B., Warnet, L.L., Akkerman, R.. Intimate Contact Development in Laser Assisted Fiber Placement. *ECCM17 - 17th European Conference on Composite Materials* 2016;1(June):26–30.
- [8] Kok, T.. On the consolidation quality in laser assisted fiber placement: the role of the heating phase. Phd thesis; University of Twente; 2018.
- [9] Composites, T.A.. TenCate Cetex® TC1200 PEEK Resin System Product Data Sheet 2017;.
- [10] Stokes-Griffin, C.M., Compston, P. Investigation of sub-melt temperature bonding of carbon-fibre/PEEK in an automated laser tape placement process. *Composites Part A: Applied Science and Manufacturing* 2016;84:17–25.
- [11] Jiang, J., He, Y., Ke, Y.. Pressure distribution for automated fiber placement and design optimization of compaction rollers. *Journal of Reinforced Plastics and Composites* 2019;38(18):860–870.
- [12] ISO 4287:1997, . Geometrical Product Specifications (GPS) – Surface texture: Profile method – Terms, definitions and surface texture parameters. International Organization for Standardization 1997;.
- [13] International Organization for Standardization, . ISO 4288:1996 Geometrical Product Specifications (GPS) - Surface texture: Profile method - Rules and procedures for the assessment of surface texture. 1996.
- [14] Mehdikhani, M., Gorbatikh, L., Verpoest, I., Lomov, S.V.. Voids in fiber-reinforced polymer composites: A review on their formation, characteristics, and effects on mechanical performance. *Journal of Composite Materials* 2019;53(12):1579–1669.

- [15] Zheng, B., Gao, X., Li, M., Deng, T., Huang, Z., Zhou, H., et al. Formability and failure mechanisms of woven CF/PEEK composite sheet in solid-state thermoforming. *Polymers* 2019;11(6).
- [16] Rodriguez-Lence, E, Martin, M.I., Fernandez Horcajo, K.. In-situ consolidation of integrated thermoplastic fuselage panels: The future in structural comercial aero-composites. In: ECCM 2018 - 18th European Conference on Composite Materials. ISBN 9781510896932; 2018,.
- [17] Peeters, D., Clancy, G., Oliveri, V., O'Higgins, R., Jones, D., Weaver, P.M.. Concurrent design and manufacture of a thermoplastic composite stiffener. *Composite Structures* 2019;212:271–280.
- [18] Hosseini, S.M.A., Schäkel, M., Baran, I., Janssen, H., van Drongelen, M., Akkerman, R.. A new global kinematic-optical-thermal process model for laser-assisted tape winding with an application to helical-wound pressure vessel. *Materials and Design* 2020;193.
- [19] Lichtinger, R., Lacalle, J., Hinterhölzl, R., Beier, U., Drechsler, K.. Simulation and experimental validation of gaps and bridging in the automated fiber placement process. *Science and Engineering of Composite Materials* 2015;22(2):131–148.
- [20] Çelik, O., Amin Hosseini, S., Baran, I., B. Grouve, W.J., Akkerman, R., J. Peeters, D.M., et al. The Influence of Inter-laminar Thermal Contact Resistance on the Cooling of Material during Laser Assisted Fiber Placement. *Composites Part A: Applied Science and Manufacturing* 2021;145(March):106367.
- [21] Saffar, F., Sonnenfeld, C., Beauchêne, P., Park, C.H.. In-situ Monitoring of the Out-Of-Autoclave Consolidation of Carbon / Poly-Ether-Ketone-Ketone Prepreg Laminate. *Frontiers in Materials* 2020;7(June):1–12.
- [22] Henne, F, Ehard, S., Kollmannsberger, A., Hoeck, B., Sause, M.G.R., Drechsler, K.. Thermoplastic in situ fiber placment for future solid rocket motor casing manufacturing. SAMPE Europe SETEC 14 - Efficient composite solutions to foster economic growth 2014;(September 2014).

Chapter 6

The Influence of Inter-laminar Thermal Contact Resistance on the Cooling of Material during Laser Assisted Fiber Placement

The effect of thermal contact resistance (TCR) correlated to the degree of intimate contact (DIC) between the incoming tape and the substrate on the temperature history during laser-assisted fiber placement (LAFP) was investigated. A novel experimental methodology was designed to understand the effect with a non-contact method which did not influence the local consolidation quality. To assess the influence of TCR numerically, a three-dimensional optical-thermal model was developed. Experimental results indicated that, for the same tape temperature near the nip point, an increase in the compaction force resulted in a decrease in the temperature at the roller exit and the following cooling phase, in correlation with an increase in the final DIC. Also, the effect of the laser power on the final DIC was less pronounced than the compaction force. In the thermal model, when TCR at the tape-substrate interface was not considered, the temperature predictions underestimated the experimental measurements.

This chapter is based on: Çelik, O., Hosseini, S.M.A., Baran, I., Grouve, W.J.B., Akkerman, R., Peeters, D.M.J., Teuwen, J.J.E., Dransfeld, C.A., The influence of inter-laminar thermal contact resistance on the cooling of material during laser assisted fiber placement. Composites Part A: Applied Science and Manufacturing, 106367, Volume 145, 2021.

6.1 Introduction

The current production rates of lightweight composite structures are far from meeting the demand of the commercial aerospace industry. For example, the production capacity of Airbus allowed 863 aircraft to be delivered in the year 2019 [1] whereas the forecasts show that around 1900 aircraft per year will be demanded from the company over the next twenty years [2]. Automated solutions are needed to increase the production rates to the required level.

Automated Fiber Placement (AFP) is a suitable candidate for production of typical aerospace components [3]. An 8-tow AFP machine can reduce the layup time up to 20 times as compared to the conventional hand layup technique [4]. In addition to that, in-situ consolidation (without a post-consolidation step in an autoclave, oven or press) is achievable with laser-assisted fiber placement (LAFP) if thermoplastic composites are used. This method has the potential for providing further reduction in cycle time, energy consumption and cost. In modern LAFP systems, a laser heat source pointed towards the nip point is used to melt the incoming tape and the substrate locally and a flexible compaction roller is used to consolidate the layers as demonstrated in Figure 6.1.

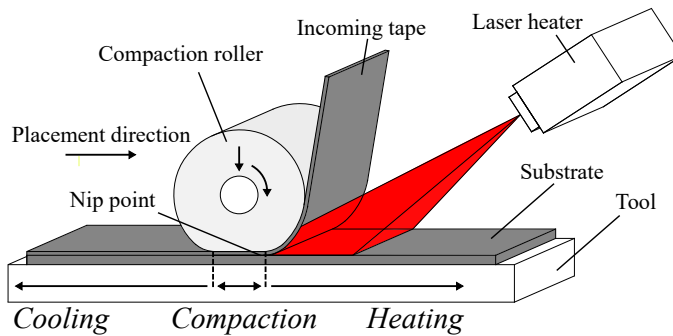


Figure 6.1. Working principle of a typical LAFP system.

During LAFP temperature is one of the main drivers for a number of phenomena that determine the final part quality such as intimate contact development, void compaction/decompaction, crystallinity evolution, healing and residual stress development. Hence, the relationship between the process parameters and the resulting temperature history must be understood very well to predict the final quality. The majority of the research considered the nip point temperature as the most important part of the temperature history and investigated the optical-thermal phenomena that determine the temperature of the tape and substrate just before compaction. Among the high number of parameters that can be modified during the process, the effects of laser power, laser angle, spot size and placement speed on the temperature history has received notable attention so far [5–9].

The effect of the void content at the interfaces after the compaction phase on the thermal history has often been overlooked. Ideally, inter-laminar voids are eliminated by squeeze flow of the fiber-resin mixture and infiltration of the resin material through the dry fibers [10] and intimate contact is established between the incoming tape and the

substrate during the compaction phase. Due to incomplete intimate contact, however, air pockets remain between the subsequent plies of the laminate. These air pockets act as insulators due to low thermal conductivity and reduce the through-thickness heat transfer as shown in Figure 6.2. This phenomenon is referred to as the inter-layer thermal contact resistance (TCR) [11]. TCR might influence the final part quality by altering the temperature history during the process.

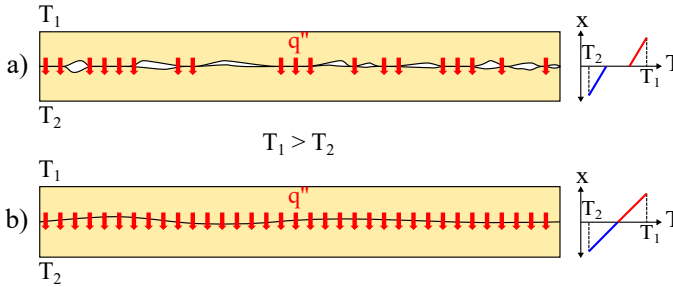


Figure 6.2. Heat flux through a composite interface and example through-thickness temperature distributions for boundary temperatures T_1 and T_2 at the top and bottom surfaces, respectively. a) Incomplete intimate contact, the air pockets act as insulators and decrease the heat flux locally. b) Complete intimate contact, uniform heat flux across the whole interface.

Typically, the thermal models of the LAFP process have been built on the assumption of perfect intimate contact between the compacted tape and substrate [8, 9, 12, 13] without experimental justification. In the work of Barasinski et al. [14], the importance of TCR for the thermal analysis of the LAFP process was mentioned. They concluded that TCR is one of the missing factors to accurately model the temperature history within the substrate. A point to note is that their experimental setup worked with a heating strategy which is different than the current LAFP systems. The tape was heated from the top instead of using a nip point heating strategy shown in Figure 6.1. The highest temperature was not generated at the nip line, which resulted in a sharper difference between the temperatures of the tape and the substrate at the point of contact. Following that work, an analytical formulation of the relationship between the degree of intimate contact and TCR was presented and validated with experimental data in the work of Levy et al. [15]. It was stated that neglecting TCR would be equivalent to deviating from the actual through thickness thermal conductivity by 50 %. However, the pressure used to manufacture the imperfectly bonded laminates was 1.34 kPa, which is orders of magnitude lower than the pressure levels commonly used in LAFP. Due to the aforementioned reasons, the results in both works may lead to an overestimation of the effects of TCR during LAFP.

Later on, Leon et al. [16] investigated the dependency between the fractal intimate contact model [17] and TCR numerically. The fractal dimension and material viscosity were found to have an effect on the evolution of TCR at the interface. However, no experimental work was conducted to validate the analyses. Chinesta et al. [18] and Lichtinger et al. [19] suggested finding the inter-layer TCR such that the temperature predictions of a thermal model matched the empirical temperature measurements. Such a method

provided little insight on the link between the microstructure at the interfaces and the accompanying TCR. Kollmannsberger et al. [20] measured TCR for in-situ consolidated laminates manufactured with and without post-consolidation and used these values to predict the temperature history with a thermal model. They compared the temperature predictions made with the experimentally obtained TCR and the equation proposed by Levy et al. [15]. Based on the results, they claimed that the equation overestimates the effect of TCR. However, the material parameters required for this equation were not measured; rather the roughness which was reported in the original publication and a constant intimate contact value of 0.75 was used without any reference to the actual degree of intimate contact of the laminate. Therefore, the theory was not related to the actual microstructure at the interfaces, which may lead to an underestimation of the effects of TCR.

To measure the effect of TCR on thermal history, thermocouples were embedded in the substrate so far [14, 20]. Contact temperature measurement methods are questionable in this case, since they directly affect the intimate contact in their surroundings. Moreover, insulation material and voids around the thermocouple add more ambiguity to the obtained data. The proposed existence or non-existence of the effects of TCR in thermal history during LAFP in the literature might be a direct result of the complications introduced by adding a thermocouple to the interface. This is why this effect must be investigated with an alternative, and preferably non-contact, temperature measurement method. Thermography is such a method and it has been applied as an in-situ, non-contact inspection method for AFP with thermoset prepreps. In the works of Denkena et al. [21] and Juarez and Gregory [22], a thermal camera was mounted on the rear side of the placement head. The acquired in-situ temperature measurement was used to detect process-induced meso-scale defects such as gaps/overlaps, twisted/spliced tows, bridging and foreign bodies but the effect of TCR was not analyzed.

The thermal history of the newly placed tape has a significant importance since, under common processing conditions, the temperature of the material is above the melting point mostly during the initial placement [7, 23]. Obviously, TCR affects the compaction and cooling phases for the newly placed tape since it requires a contact between the tape and the substrate. However, it is not possible to monitor the compaction phase of the process with current non-contact technologies.

The objective of this paper is therefore to investigate the effect of TCR (and the related degree of intimate contact) on the temperature history during the *cooling phase of the newly placed tape* considering the actual microstructure of the laminate. A novel experimental methodology and numerical model were used for the investigation. First, specimens with varying degrees of intimate contact were manufactured with a state-of-the-art LAFP setup (Section 6.2). During manufacturing, the temperatures before and after compaction were recorded with two long-wave infrared (LWIR) cameras. After manufacturing the samples, the degree of intimate contact at the topmost interface of the samples was measured from cross-sectional micrographs. An optical-thermal model of the process and the formulation by Levy et al. [15] were combined to calculate the temperature history for different degrees of intimate contact (Section 6.3). Finally, the effects of TCR were discussed combining the experimental and numerical results.

6.2 Materials and Experimental Methods

6.2.1 Fiber Placement System and Specimen Manufacturing

The specimens were manufactured at Royal Netherlands Aerospace Center (NLR) as in a previous study [10]. A six-axis articulated robot on a linear axis provided by Coriolis was used. The machine was able to deliver eight 6.35 mm ($\frac{1}{4}$ in.)-wide tapes simultaneously with a placement speed of up to 800 mm/s. The end effector was equipped with a 6 kW Laserline LDF series diode laser system and an optic lens which created a 56 mm×28 mm rectangular illuminated area at the 250 mm focal distance. A conformable compaction roller with 60 shore hardness and a diameter of 70 mm was installed on the machine. The roller had a coating on the outer surface which increased the contact stiffness and reduced the effects of temperature. For this study, a second thermal camera was mounted to the rear side of the machine in addition to the front thermal camera which is commonly used for process control as shown in Figure 6.3.

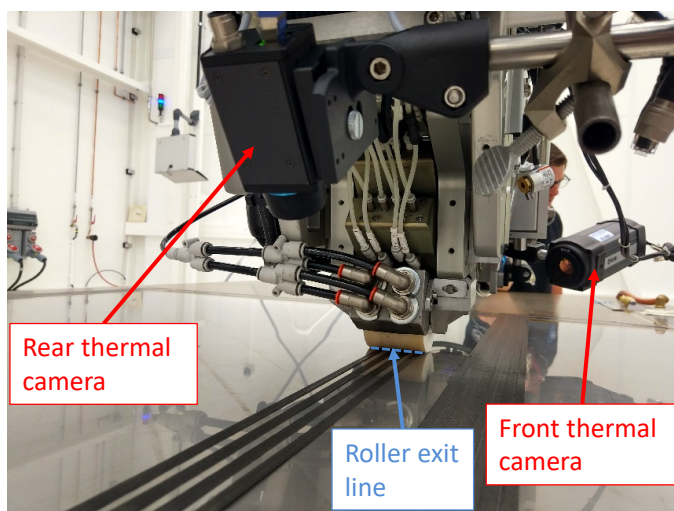


Figure 6.3. Front and rear thermal cameras on the fiber placement machine to measure the tape inlet and roller exit temperatures during the process.

The material used in this study was Toray Cetex TC1200 carbon fiber reinforced polyetheretherketone (CF/PEEK) tapes (fiber volume fraction 59 %, melting temperature (T_m) 343 °C, glass transition temperature (T_g) 143 °C [24]) in 6.35 mm-wide slit form. The thickness of the prepreg was 0.15 mm. First, 1000 mm-long, $[0]_5$ substrates were placed on an aluminum tool for each specimen depositing only the odd tows (Tows 1-3-5-7 as demonstrated in Figure 6.4) instead of all eight tows. This was done to reduce the laminate width so that loss of contact with the aluminum tool due to warpage was minimized. Additionally, the pressure over the width of the compaction roller was kept uniform by depositing four odd tows simultaneously. The laser power was set to 1500 W for the first layer and 1750 W for the remaining four layers. The compaction force and the

placement speed were set to 500 N and 100 mm/s, respectively. These parameters were determined based on previous experience so that the substrates have low inter-laminar void content.

Following the substrate production, the sixth layer of each specimen was placed with the process parameters in Table 6.1. The laser power was varied so that the effects of TCR could be investigated for three different tape inlet temperatures. Throughout this paper, the term "tape inlet temperature" will be used to describe the temperature of the tape just before the nip point as it can be observed from the front thermal camera images shown in Figure 6.4a. At the lowest power level, a tape inlet temperature below the melting temperature of PEEK (343 °C) was aimed for. This processing condition is not ideal for a high quality laminate since the viscosity of the CF/PEEK tape is expected to be very high, hindering the material flow at the layer interfaces. At the medium power level, the tape was kept within the processing temperature range suggested by the tape manufacturer (370–400 °C [24]). At the highest power level, a processing temperature which is highly above the melting temperature, yet below the degradation temperature (500 °C for a placement speed of 100 mm/s [7]) was aimed for. Such a tape inlet temperature was reported to result in superior laminate quality [7]. The compaction force levels were determined considering the range in which the closed loop control system can apply the desired compaction force reliably and conveniently.

Table 6.1. Process parameters used for manufacturing the samples.

Experiment No.	Laser Power (W)	Compaction Force (N)	Placement speed (mm/s)
1	1300	100	100
2	1300	500	100
3	1300	1000	100
4	1500	100	100
5	1500	500	100
6	1500	1000	100
7	1750	100	100
8	1750	500	100
9	1750	1000	100

6.2.2 Process Temperature Measurement

The process temperature was recorded during the placement of the sixth layer with two LWIR cameras as shown in Figure 6.3. A FLIR SC325 (320×240 pixel-resolution, calibrated in the 200–1200 °C range to ± 2 °C or ± 2 %) and a FLIR A35 (320×256 pixel-resolution, calibrated in the -40–550 °C range to ± 5 °C or ± 5 %) were mounted on the front and rear sides, respectively. Examples of in-situ measurements from both cameras are demonstrated in Figure 6.4.

The measurements from the front camera were used to compare the effect of different laser power and compaction force values on tape inlet and substrate temperatures. Two measurement lines were placed on the tape and the substrate near the visible nip

point of the fifth tow as shown in Figure 6.4a. The average temperature during the steady portion of the placement course was calculated.

The rear camera was used to measure the temperature distribution along the length on the top surface of the newly placed tape at the roller exit. This was done by placing a measurement line at the centerline of the fifth tow in the thermal image as demonstrated in Figure 6.4b. The length of the measurement line was determined from a calibration image in which a ruler is positioned parallel to the roller exit line (referring to Figure 6.3) at 50 mm distance. The measurement line was positioned so that it extended from the roller exit to the edge of the ruler in the calibration image. The distance between the roller exit line and the calibration ruler was determined such that the measurements were performed in close vicinity to the compaction roller to avoid the effects of the macroscopic deformation, i.e. sliding of the slender laminates during placement. The average temperature distribution on the line was calculated for 100 frames where the process had reached steady state.

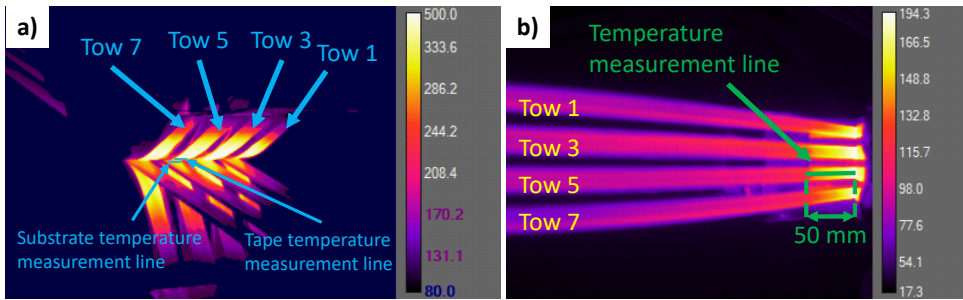


Figure 6.4. Thermal images obtained from a) the front thermal camera to measure the tape inlet and substrate temperatures, b) the rear thermal camera to measure the temperature distribution at the roller exit during the process.

6.2.3 Intimate Contact Measurement

To measure the intimate contact at the topmost interface of each specimen, cross-sectional micrographs were captured and analyzed. Samples were extracted from the fifth tow of each placement trial since this tow is the closest to the center of the compaction roller in the width direction. Five 15 mm-long samples were cut along the width past the first 300 mm of the laminate, where the nip point temperature reaches the steady state, as shown in Figure 6.5. The samples were embedded in mounting resin, ground and polished for high quality images. A Keyence VK-X1000 laser microscope was used to capture the cross-sectional micrographs of the topmost interface of the laminates. The whole width of each interface was captured by stitching multiple images taken with a 50x-magnification lens to obtain high resolution images ($0.55 \mu\text{m}/\text{pixel}$).

A custom-made Matlab script was used to analyze the cross-sectional images with the methodology shown in Figure 6.6. The script requires the cross-sectional image of the interface as an input (Figure 6.6a). Since the topmost interface was not a straight line for most of the images, a measurement curve was defined by selecting points manually

(Figure 6.6b). The script allows the user to magnify the image, so the interface can be selected with high precision. This initial curve was offset by one pixel in positive and negative vertical directions to create two additional curves. This was done to ensure that the results were not affected by local features in the image without deviating too much from the bond line into the tape and substrate material. Then, a grayscale histogram was generated for each image. From this histogram, a threshold was determined with Otsu's threshold method [25] and the image was segmented such that the fiber-matrix mixture was distinguished from the voids (Figure 6.6c). After the segmentation procedure, the voids and the fiber-matrix mixture at the interface can be identified by the black and white pixels, respectively (Figure 6.6d). Finally, the degree of intimate contact was calculated as the ratio between the length of the white areas on the measurement curve and the total length of the measurement curve. The results from the three curves were averaged to obtain the final degree of intimate contact for each sample (Figure 6.6e). The maximum deviation between the measured degrees of intimate contact on the three curves for an individual cross-section was 2.3 %.

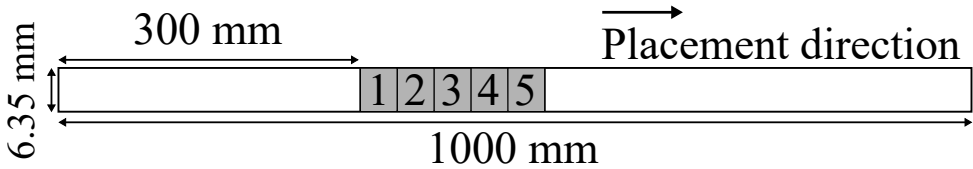


Figure 6.5. Top view of the extraction locations of five samples for intimate contact investigation. The dimensions are not to scale.

6.2.4 Analysis of Variance (ANOVA)

Two-way analysis of variance (ANOVA) method was applied on the results of the temperature measurements described in Section 6.2.2 and intimate contact measurements described in Section 6.2.3 to assess the effects of the laser power and compaction force quantitatively. The Matlab built-in function *anovan* was used for this purpose [26]. The outputs of this function were p-values for each parameter investigated in Table 6.1. p-values smaller than 0.05 imply that the mean response of the specific parameter is different from the mean of all data within a confidence interval of 95 %. The effect of such a parameter can be considered statistically significant.

6.3 Numerical Methods

The compaction force changes a number of parameters during the LAFP process not only by altering TCR (and degree of intimate contact) via applied pressure but also changing the roller geometry. The first effect concerns the laser irradiation on the tape and substrate. As the roller deforms by increased compaction force, the location of the nip point and the shape of the incoming tape near the nip point changes. This theoretically results in a decreased shadow area and a higher temperature at the nip point [27],

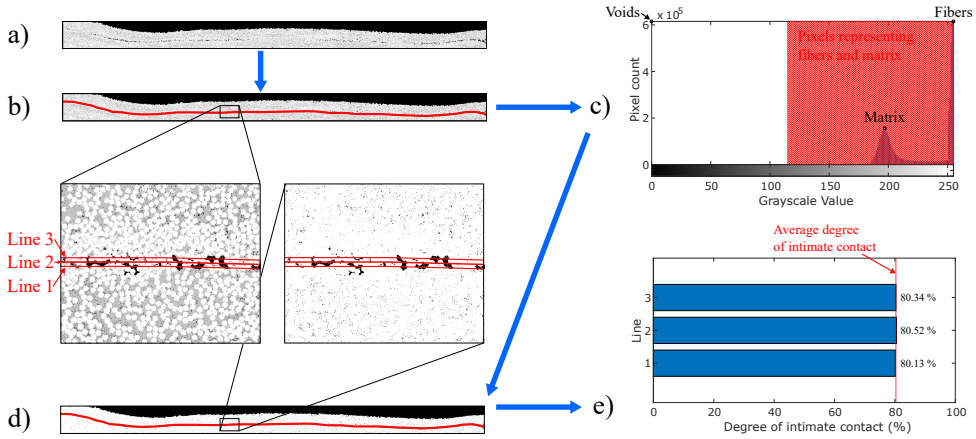


Figure 6.6. Methodology for intimate contact measurement at the topmost interface from cross-sectional images. a) High resolution image of the interface. b) Definition of bond line manually (Line 2) and automatic generation of offset curves (Lines 1 and 3). The distance between the lines are not to scale. c) Segmentation of the image using the grayscale histogram and Otsu's thresholding method to distinguish the fiber-matrix mixture from the voids. d) Segmented cross-sectional image with the measurement curves. e) Calculated degree of intimate contact on each curve and the average intimate contact for the interface.

and hence, the roller exit. The second effect is observed during the compaction phase. An increasing compaction force extends the contact length, which causes more heat to be dissipated to the roller. This might cause a lower temperature at the roller exit [28]. Since the effects of the change in the nip point location and the contact length contradict with each other, a heat transfer model which includes an optical model and a variable roller contact length was formulated. Such a model can be used to isolate the effects of TCR on the temperature history. The following sections describe the calculation of TCR from intimate contact measurements and the temperature distribution during the process using a heat transfer model.

6.3.1 Thermal Contact Resistance Calculation

To calculate the thermal contact conductance from the experimentally obtained degree of intimate contact at the interface, the equation proposed by Levy et al. [15] was used:

$$\frac{1}{C} = R = D_{ic,init} a_0 \left(\frac{1}{\lambda_{CFRP} D_{ic}^2} + \frac{1 - D_{ic}}{\lambda_{air} D_{ic}} + \frac{1}{\lambda_{CFRP}} \right) \quad (6.1)$$

where C is the thermal contact conductance, R is the thermal contact resistance, $D_{ic,init}$ is the initial degree of intimate contact, a_0 is the height of the rough surface layer, λ_{CFRP} is the through-thickness thermal conductivity of the composite material, D_{ic} is the degree of intimate contact at a given moment and λ_{air} is the thermal conductivity of air.

This equation expresses the thermal contact conductance assuming that the interface is a thin layer of homogenized mixture of the composite and air.

During LAFF, $D_{ic,init}$ is very difficult, if not impossible, to measure with the current technology since the nip point poses extreme difficulty in positioning any kind of sensors and the consolidation takes place in a very short time. Therefore, the initial surface profile of the tape was utilized to estimate $D_{ic,init}$ as it was done in literature [29, 30] instead of the methodology proposed in Section 6.2.3. This methodology is not convenient to analyze the surface of an individual tape since it requires voids trapped in solidified resin at the interfaces of multiple layers to define measurement curves. $D_{ic,init}$ and a_0 were calculated from surface profiles measured from samples of unprocessed tape with an Olympus LEXT OLS3100 confocal laser scanning microscope using a $\times 50$ lens. The resolution was $0.25 \mu\text{m pixel}^{-1}$ and the profile length was $256 \mu\text{m}$. In total, fifteen profiles were captured. For $D_{ic,init}$, the surface profiles were approximated as a series of uniform rectangles that are schematically shown in Figure 6.7. The width of the rectangles (b_0) and the surrounding gap (w_0) were found by calculating the average width of the material and gaps at different height levels within $\pm 2\sigma$ from the mean surface height, where σ designates the standard deviation. Having the dimensions of the rectangles, $D_{ic,init}$ is calculated as [29]:

$$D_{ic,init} = \frac{b_0}{b_0 + w_0} \quad (6.2)$$

Equation (6.2) yielded an initial degree of intimate contact of 0.437 for the material used in this study. a_0 was calculated as the average standard deviation, σ , which was $12.6 \mu\text{m}$. D_{ic} was measured for each experiment in Table 6.1 with the methodology described in Section 6.2.3. The values for λ_{CFRP} and λ_{air} were taken as 0.72 W/mK [31] and 0.0043 W/mK [32], respectively.

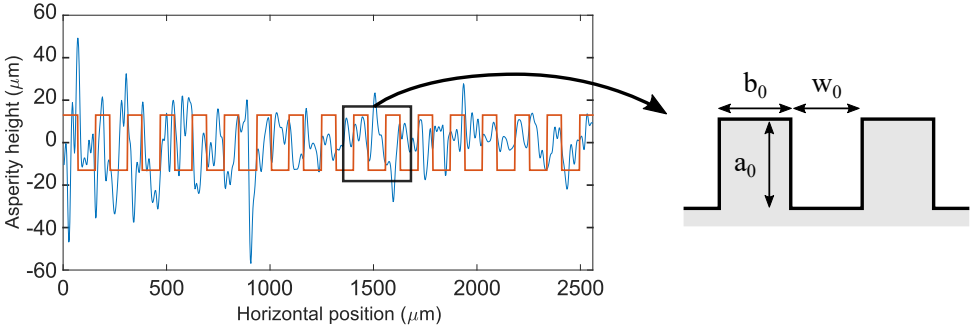


Figure 6.7. Uniform rectangle idealization of the composite surface and associated geometric parameters.

6.3.2 Heat Transfer Model

The transient temperature distribution during the fiber placement process was calculated with a three dimensional finite element (FE) model adapted from authors' previous work [33]. Abaqus 2017 finite element package was used to create and solve the

model. The incoming tape and substrate were modeled as two stationary bodies in a Lagrangian reference frame. A moving placement head configuration was implemented, i.e. the laser illuminated area and the area where the convection coefficient was applied due to the compaction roller moved according to the placement speed. The modeling space and boundary conditions are visually demonstrated in Figure 6.8.

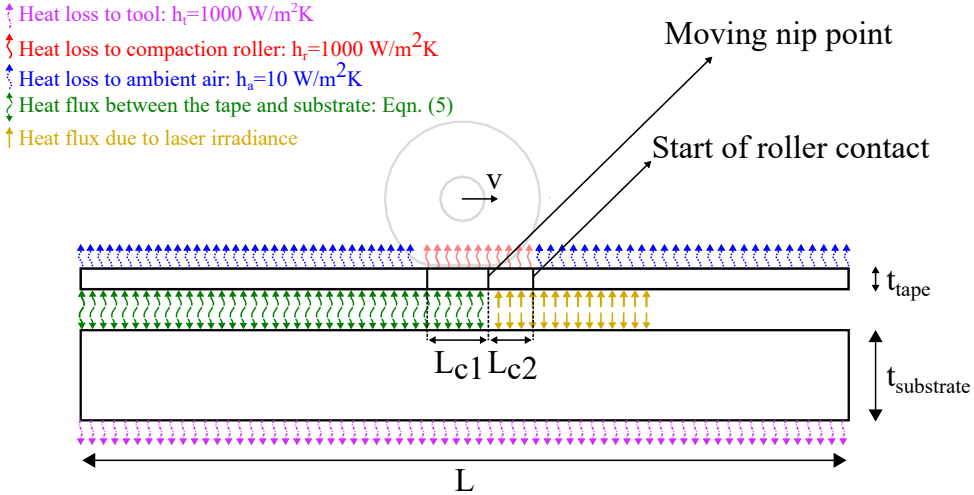


Figure 6.8. Modeling space and moving boundary conditions of the FE model. h represents the applied convection coefficient. For the other parameters, please refer to Table 6.3.

The energy equation was solved to find the transient temperature distribution $T(t)$ within the incoming tape and substrate, with the assumption of negligible internal heat generation:

$$\rho C_p \frac{\partial T}{\partial t} = \nabla(k \nabla T) \quad (6.3)$$

where ρ is the density, C_p is the specific heat and k is the anisotropic thermal conductivity of the material.

The following boundary conditions were applied referring to Figure 6.8. The initial temperatures of the incoming tape and substrate were defined as 20 °C. The laser irradiance, compaction roller and the nip point moved in the placement direction with the placement speed v . Until the nip point, the bottom surface of the tape and the top surface of the substrate were heated with the laser irradiance obtained from the ray tracing model proposed in [34]. This model accounts for the non-specular reflection of the laser light between the tape and substrate using a bidirectional reflectance distribution function (BRDF)-based micro-model. As schematically described in Figure 6.9, several geometric parameters for the laser source, incoming tape, substrate and compaction roller are required as an input for the model. These parameters were determined from on-site measurements and Computer Aided Design (CAD) drawings of the placement head. A summary of the parameters used in the optical model is given in Table 6.2.

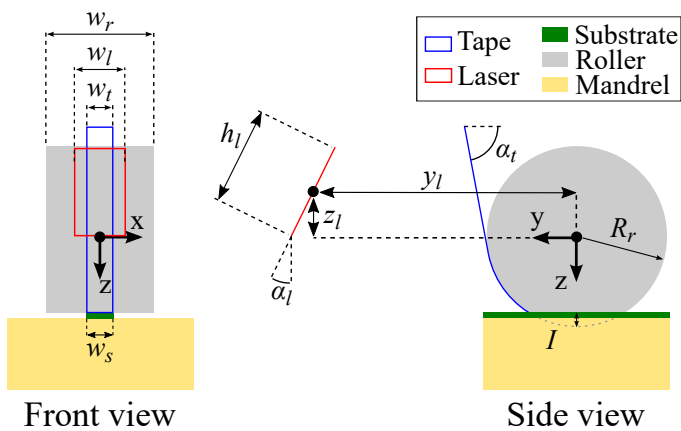


Figure 6.9. Description of the optical model geometry.

Table 6.2. Geometrical parameters used in the optical model.

Parameter	Description	Value
w_r	Roller width	60 mm
R_r	Roller radius	35 mm
I	Roller indentation	0.41, 0.9 and 1.47 mm (at 100, 500 and 1000 N, respectively)
w_l	Laser spot width	56 mm
h_l	Laser spot height	28 mm
y_l	Laser y-position relative to the roller center	265.3 mm
z_l	Laser z-position relative to the roller center	49.1 mm
α_l	Laser angle	18°
w_t	Tape width	6.35 mm
α_t	Tape feed angle	45°
w_s	Substrate width	6.35 mm

Prior to the nip point and during the compaction process (L_{c2} and L_{c1} in Figure 6.8, respectively), the top surface of the tape cools down due to the contact with the compaction roller. Before and after the contact with the roller, the ambient air cools down the top surface of the tape. The heat loss to the compaction roller and the ambient air were formulated as a moving convection boundary condition:

$$k\nabla T = -h(T - T_a) \quad (6.4)$$

where h is the convection coefficient and T_a is the ambient temperature at the corresponding boundary. Equation (6.4) was also used to express the heat loss at the bottom surface of the substrate due to the contact with the aluminum tool.

The convection coefficient (h_a) and T_a for the air were taken as $10 \text{ W/m}^2\text{K}$ [35] and 20°C , respectively. The roller and tool convection coefficients (h_r and h_t , respectively) were determined by iteratively comparing the numerical results with the temperature measurements from the top surface of the newly placed tape. This was done for the sample manufactured with a laser power of 1750 W and a compaction force of 1000 N , since the least amount of inter-laminar voids were observed in this specimen due to the high temperature and pressure. This procedure resulted in $1000 \text{ W/m}^2\text{K}$ for both h_r and h_t . These values are in agreement with the values reported in the literature [31, 36]. T_a was 160 , 180 and 200°C for the roller at the power levels 1300 , 1500 and 1750 W , respectively (measured from the thermal images) and 20°C for the tool.

At the tape-substrate interface, the heat transfer was modeled with a thermal contact [37]:

$$q = C(T_{\text{tape}} - T_{\text{substrate}}) \quad (6.5)$$

where q is the heat flux between the tape and the substrate and C is the thermal contact conductance. The value of C was updated based on the location of the moving nip point. At the regions in front of the nip point, no heat transfer was possible between the tape and the substrate. To impose this condition without creating numerical problems, the thermal contact conductance was set to a very low value, namely $10^{-5} \text{ W/m}^2\text{K}$. Past the nip point, the thermal contact conductance was set to the reciprocal of the value obtained from the TCR calculations explained in Section 6.3.1 to represent the imperfect thermal contact due to incomplete intimate contact development. A constant C was assumed immediately after the nip point. For comparison purposes, a set of simulations which represent the case of perfect intimate contact were also run by setting the thermal contact conductance to a very high value, namely $10^6 \text{ W/m}^2\text{K}$.

The process settings and geometric parameters used in the model are summarized in Table 6.3. Thermal material properties provided in Table 6.4 were used for the composite material. The coordinates of the laser irradiation, area with heat loss to the compaction roller and thermal contact conductance were updated with the user subroutines DFLUX, FILM and GAPCON, respectively.

DC3D8 linear hexahedral heat transfer elements were used to mesh the tape and the tool. The tape was meshed with 10, 120 and 6 uniform elements in the thickness, length and width directions, respectively. The substrate was meshed with 120 and 6 uniform elements in the length and width directions, respectively and with 15 biased elements in the thickness direction (thickness ranging between 0.012 mm and 0.12 mm , finer near the top surface).

Table 6.3. The process settings and geometric parameters used in the heat transfer model

Parameter	Symbol	Value	Unit
Placement speed	v	100	mm/s
Roller contact length in the compaction zone	L_{c1}	10.6, 15.7, 20.1 (at 100, 500 and 1000 N, respectively)	mm
Roller contact length prior to the nip point	L_{c2}	17	mm
Domain length	L	100	mm
Tape thickness	t_{tape}	0.15	mm
Tape width		6.35	mm
Substrate thickness	$t_{\text{substrate}}$	0.75	mm
Substrate width		6.35	mm

Table 6.4. Temperature dependent material properties of CF/PEEK [35]

Temperature (°C)	Density (kg/m ³)	Specific Heat (J/kg°C)	Thermal conductivity (W/m°C)	
			Longitudinal	Transverse
0	1601	800	3.5	0.42
50	1598	930	4.6	0.52
100	1593	1040	5.1	0.6
150	1586	1260	5.9	0.7
200	1575	1300	5.9	0.7
250	1563	1400	6.1	0.7
300	1551	1550	6.7	0.75
350	1537	1650	6.8	0.68
400	1524	1700	7	0.65

6.4 Results

6.4.1 Experimental Process Temperature

The measured tape inlet temperatures at different laser power and compaction force values are shown in Figure 6.10a. Local temperature variations during LAFP have been previously observed and attributed to material inhomogeneity [38, 39]. Due to differences in local fiber volume fraction, varying amounts of laser power can be absorbed at different sections of the material. The standard deviation in Figure 6.10a is most likely a result of that. As the laser power increased, the tape temperature increased for all compaction force levels at an average rate of $\sim 0.3^\circ\text{C}/\text{W}$. A notable observation is that the inlet temperature was above the melting temperature of the CF/PEEK material (343°C [24]) for the laser powers of 1500 and 1750 W, whereas it was slightly below the melting temperature for the laser power of 1300 W, as intended. A clear relation between the compaction force and the tape inlet temperature, however, was not observed. This was also reflected in the results of the ANOVA; the effect of the laser power was statistically significant ($p=0.0002$) in contrast to the effect of the compaction force ($p=0.2372$). Recent studies proposed that the roller deformation due to increasing compaction force has an influence on the tape temperature during the LAFP process [27]. The results in Figure 6.10 show that the roller deformation did not influence the tape inlet temperature more than the experimental scatter for the experimental setup and process parameters in this study.

Figure 6.10b shows the effect of laser power and compaction force on the substrate temperature. Similar to the tape, material inhomogeneity results in variation in temperature and the standard deviation for each measurement is shown. For every experiment, the average substrate temperature was below the melting temperature of PEEK. As the laser power increased, the substrate temperature increased for all compaction force levels at an average rate of $\sim 0.16^\circ\text{C}/\text{W}$. As the compaction force was increased from 100 N to 1000 N, the substrate temperature increased by 28, 23 and 15°C for the laser powers of 1750, 1500 and 1300 W, respectively. Unlike the tape inlet temperature, a steady increase was observed for increasing compaction force levels. This result is in-line with the literature in the sense that the effect of roller deformation on the substrate temperature is more pronounced than the tape temperature [28]. The results of ANOVA shows that for the substrate temperature, the effects of both the compaction force ($p=0.0079$) and the laser power ($p=0.0001$) are statistically significant.

The measured temperature histories in the cooling region at the rear side of the roller are shown in Figure 6.11 with solid lines. The data was measured as a function of the distance from the roller exit line; however, it also represents the temperature history of an arbitrary location on the top surface of the tape after the roller passes over it since the placement speed is known (100 mm/s). The corresponding time is also shown in the figures. The shaded zones around the solid lines indicate the standard deviation of the 100 temperature profiles extracted with the methodology described in Section 6.2.2. The compaction force had an influence on the roller exit temperature for all laser power levels. An increase in the compaction force resulted in a decrease in the temperature at the roller exit. The difference between the maximum and minimum temperatures due to the various compaction forces at the roller exit was as high as 30°C . When the compaction

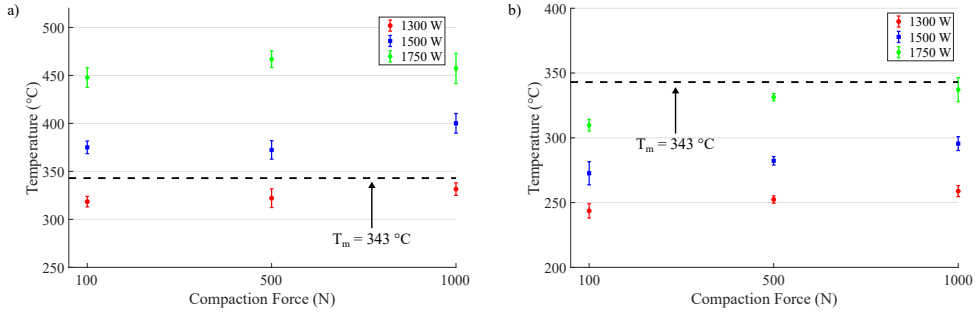


Figure 6.10. a) Tape inlet and b) substrate temperatures for the fifth tow at each laser power and compaction force. Error bars represent the standard deviation. The melting temperature of PEEK is marked.

force was decreased to 100 N, a significant increase in temperature was observed at the roller exit compared to 500 N case ($\sim 20^\circ\text{C}$), even though the tape inlet temperature was not higher and substrate temperature was even lower (Figure 6.10). However, the roller exit temperature difference between the 500 N and 1000 N cases was lower ($\sim 10^\circ\text{C}$). When the effect of the laser power is examined, it can be seen that the roller exit temperature increased with increasing laser power with an average rate of $\sim 0.1^\circ\text{C}/\text{W}$. The effect of the laser power on the exit temperature was lower than its effect on the tape inlet temperature. The effects of both the laser power ($p=0.0000$) and the compaction force ($p=0.0001$) on the roller exit temperature were statistically significant, as shown by ANOVA.

6.4.2 Intimate Contact

Representative cross-sectional micrographs of the topmost interface of the specimens manufactured with the same laser power (1750 W) but different compaction forces (100 N and 1000 N) are shown in Figure 6.12. In Figure 6.12a, inter-laminar voids due to the low compaction force (100 N) can be observed. These voids are expected to reduce the through thickness heat transfer as demonstrated in Figure 6.2. In contrast, high compaction force (1000 N) resulted in an almost void-free interface. The void content in the inter-laminar region was very low as shown in Figure 6.12b.

The measured degree of intimate contact at the topmost interface for each parameter combination is shown in Figure 6.13. The ANOVA method was used to quantify the effects of the laser power and the compaction force. The analysis showed that the laser power had a statistically insignificant effect ($p=0.3026$) on the final degree of intimate contact whereas the effect of the compaction force was statistically significant ($p=0.0000$). This is an interesting result since the temperature history is expected to affect intimate contact development significantly by determining the resin viscosity. Yet, the compaction force seems to drive the resulting degree of intimate contact independently of the temperature levels.

A compaction force of 100 N resulted in the lowest degree of intimate contact for all

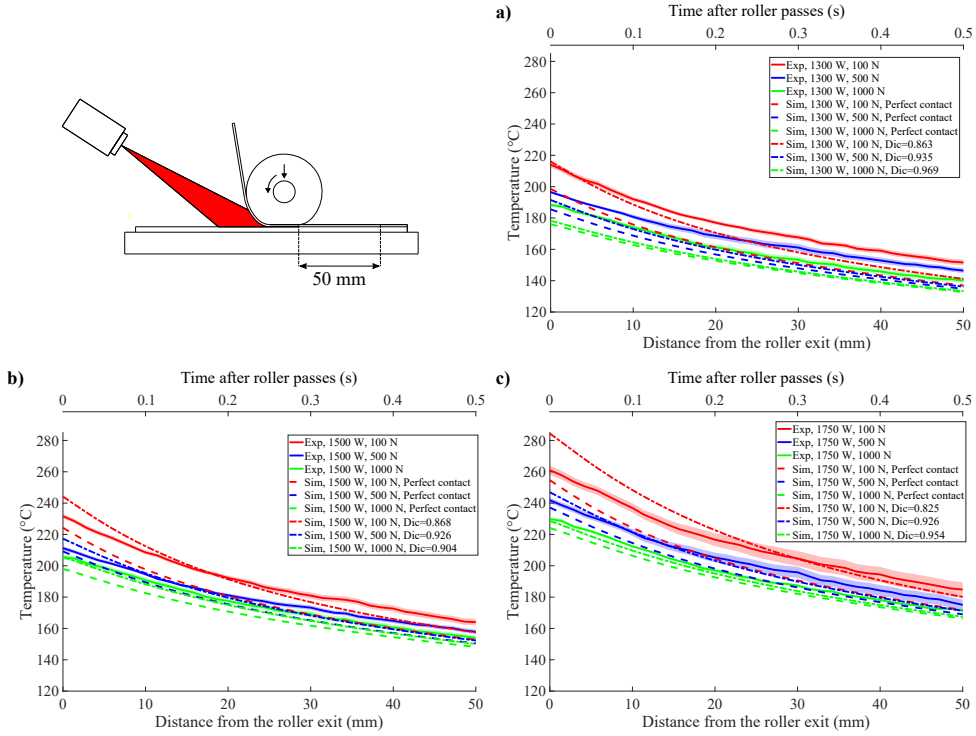


Figure 6.11. Tape temperatures at the roller exit on the top surface of the fifth tow for different compaction forces and laser powers of a) 1300 W, b) 1500 W, c) 1750 W



Figure 6.12. Examples of cross-sectional micrographs of the topmost interface. a) low intimate contact (80.3 %, at 1750 W and 100 N) b) high intimate contact (95.6 %, at 1750 W and 1000 N).

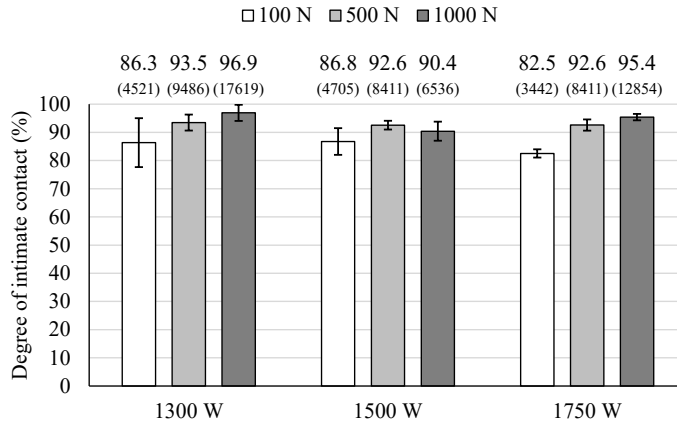


Figure 6.13. Degree of intimate contact for each specimen. The horizontal axis shows the laser power and the color of each bar indicates the compaction force. The first row on top of the bars shows the average degrees of intimate contact. Error bars represent the standard deviation. Values in the parantheses show the corresponding thermal contact conductance in W/m^2K calculated using Equation (6.1).

6

laser power levels. The degree of intimate contact increased as the compaction force was increased. The difference between the 500 N and 1000 N was smaller than the difference between the 100 N and 500 N. The reason for that can be the nonlinear relationship between the applied force and the resulting pressure under the compaction roller. As the roller is deformed further, the contact area increases and limits the pressure [10]. The standard deviation increased at low compaction force for 1300 W and 1500 W. This might be a result of material scatter which could not be eliminated with the amount of pressure applied.

6.4.3 Calculated Temperature History

Calculated temperature at the cooling phase

Calculated temperature histories up to 50 mm from the roller exit for each laser power and compaction force are shown in Figure 6.11 with two types of dashed lines. The dash-dot lines (— · —) show the temperature histories calculated with the TCR values given in Figure 6.13, which were obtained from Equation (6.1) for each process parameter, were used. These temperature values will be mentioned as calculated temperature with imperfect contact (CTIC) in the upcoming discussions. In addition to those, the dashed lines (— —) present the temperature histories calculated with a very small TCR (perfect interface assumption). These will be denoted as calculated temperature with perfect contact (CTPC). As expected, CTPC resulted in a lower temperature than CTIC at any distance from the roller exit for all laser power and compaction force levels. As TCR decreased, the heat transfer from the tape to the substrate during the compaction and cooling periods became greater.

When CTIC is compared with the experimental data, it can be observed that an excellent agreement is present at the highest compaction force (1000 N) for laser powers of 1500 and 1750 W (Figure 6.11b and Figure 6.11c). It should be noted that the convection coefficient between the roller and the top surface of the tape was determined for the case of 1750 W and 1000 N and it was assumed that this value does not change with decreasing force. Only the change in the contact length was considered. As the compaction force was decreased at these laser power levels, the temperature calculations overshoot the experimental results at the region immediately following the roller exit (approximately the first 7 mm and 20 mm for 500 N and 100 N, respectively). After this initial behavior, the calculated temperature equaled the experimental one but cooled down faster until both curves had a similar cooling trend at around 40 mm. For the lowest laser power (1300 W), the trends slightly differed as shown in Figure 6.11a. For every compaction force, the temperature was underestimated with a calculated TCR for the whole distance range from the roller exit. The only exception was the temperature at the roller exit for the compaction force of 100 N, which was equal to the experimental temperature. However, CTIC cooled down faster than the experimental temperature initially as well, similar to the other laser power levels. While CTIC yielded temperature predictions comparable with the experimental data, CTPC underestimated the temperature at any distance from the roller exit for any case.

Calculated temperature at the compaction phase

To understand the difference between CTIC and CTPC further, calculated tape and substrate temperatures during the compaction phase of the process are presented in Figure 6.14. The results are reported only for the laser power of 1750 W and compaction force of 100 N for the sake of clarity, as the combination of these parameters resulted in the least degree of intimate contact (Figure 6.13) and the highest difference between CTIC and CTPC (Figure 6.11). The trends did not differ for the other process parameters. The first difference can be observed at the nip point, where the bottom surface of the tape and the top surface of the substrate contact each other. As expected, CTPC led to similar temperatures at the bottom surface of the tape (300 °C) and the top surface of the substrate (294 °C), which quickly equalized in the subsequent time steps. CTIC, however, resulted in a significant difference between the temperatures at the same locations of the tape (359 °C) and the substrate (233 °C). This demonstrates the effect of TCR on the heat transfer between the tape and substrate; for CTIC, cooling of the tape and heating of the substrate at the nip point were slower than CTPC. The second difference can be observed at the end of the compaction phase. The temperatures of both the bottom surface of the tape and the top surface of the substrate were 246 °C for CTPC. In the case of CTIC, these temperatures were 276 °C and 230 °C for the tape and substrate, respectively. The final difference is at the temperature of the top surface of the tape. CTIC resulted in higher temperatures at the top surface of the tape (366 °C at the nip point, 284 °C at the end of the compaction phase) than CTPC (357 °C at the nip point, 255 °C at the end of the compaction phase).

A temperature plateau can be observed at the end of the compaction zone on the top surface of the tape. The reason for that is the heat accumulation at the center of the tape in the thickness direction. During the compaction phase, a temperature gra-

dient occurred in the thickness direction of the tape due to contact with the roller and the substrate on the opposing surfaces. As a result, in the thickness direction, the center of the tape became warmer than the surfaces. Once the roller passed, heat flowed towards the tape surfaces due to conduction within the tape. This slightly increased the temperature of the top surface momentarily, as the low convection coefficient between the ambient air and the top surface ($10 \text{ W/m}^2\text{K}$) resulted in an almost insulated boundary. The bottom surface of the tape was not significantly affected since the main driver of cooling was the contact with the substrate with a comparatively large thermal contact conductance ($>3442 \text{ W/m}^2\text{K}$, as shown in Figure 6.13).

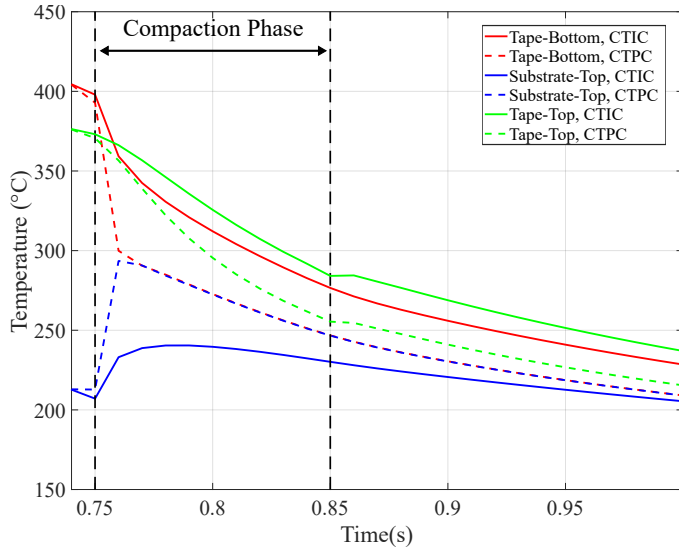


Figure 6.14. Calculated temperatures for the tape and substrate during the compaction phase for the laser power of 1750 W and compaction force of 100 N.

6.5 Discussion

6.5.1 Effect of compaction force on cooling behavior

The temperature measurements from the rear side of the compaction roller (Figure 6.11) show that the compaction force has a significant influence on the temperature of the newly placed thermoplastic tape in the cooling phase of LAFP. As demonstrated in Figure 6.15, it has such an importance that aft the roller exit, a tape placed with a laser power of 1300 W and a compaction force of 100 N cooled down similarly to a tape placed with a laser power of 1500 W and a compaction force of 1000 N despite the difference in energy input at the heating phase. A similar relationship holds for the laser powers of 1500 W and 1750 W as well. Since no compaction pressure is present in the cooling phase, a variation in the temperature might affect the final void content and residual

stresses. In addition, the variation in the temperature due to altering compaction force has potential implications for the final degree of crystallinity of the structure, as the maximum crystallization rate of PEEK was observed between 200–280 °C [40]. Compaction force should, therefore, be considered as an integral part of any LAFP process design to control not only ply adhesion or mechanical defects such as gaps/overlaps but also the temperature history.

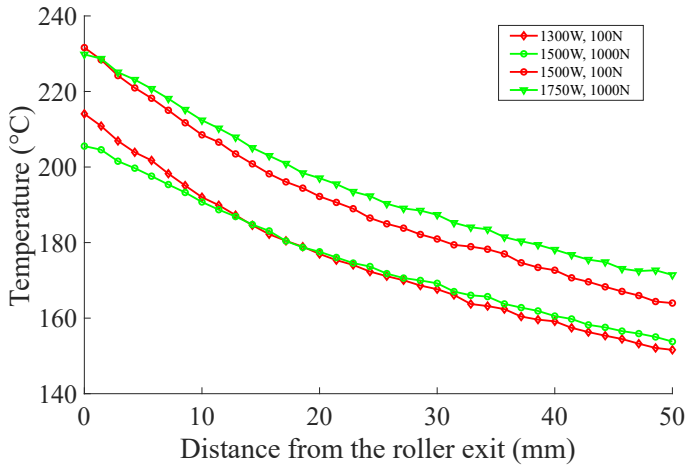


Figure 6.15. Experimental temperature histories showing the effect of the compaction force on the cooling behavior observed at different power levels as a result of varying compaction force.

6.5.2 The role of TCR on temperature calculations

Thanks to the thermal model presented in Section 6.3, the effects of TCR could be separated from the other possible effects of the roller deformation induced by varying compaction force on the temperature history. When a perfect thermal contact was assumed at the interface, the model underestimated the temperature at the roller exit and the subsequent cooling period, as shown in Figure 6.11. Also, numerical results presented in Figure 6.14 showed that the temperature at contacting surfaces of the tape and substrate were influenced significantly during the compaction phase of the process. Therefore, in this study, it was found that TCR has a significant role in the resulting temperature history. This observation contradicts the claim that the effect of TCR is negligible for thermal analysis of LAFP [20]. Possibly, a laminate with a high degree of intimate contact was investigated in that study, reducing the influence of TCR on temperature history predictions. Such an effect was observed in this study as well, as demonstrated in Figure 6.16. This figure shows the temperature difference between CTIC and CTPC in Figure 6.11 for each experiment and the degree of intimate contact (Dic) for each curve is presented in the figure legend. The temperature difference between CTIC and CTPC was less than 10 °C at the roller exit when the degree of intimate contact was more than 90 %.

However, a final degree of intimate contact below 85 % was reported in several works [27, 41, 42], meaning that TCR can not be neglected for all LAFP systems and process parameters. Moreover, as LAFP technology with in-situ consolidation matures, research in the field has expanded to more complex parts such as a fuselage panel [43], variable-stiffness wingbox [44] and a pressure vessel [45]. Complex tool shapes introduce convex or concave surfaces which result in a non-uniform pressure distribution under the compaction roller [46, 47], as well as transient heat flux distribution [45]. This may result in areas with insufficient intimate contact. Also, it should be noted that the results presented in this work are limited to unidirectional laminates. In a laminate consisting of layers with different orientations, intimate contact development might be lower due to the lack of fiber nesting. For such cases, the effect of TCR can be even more important.

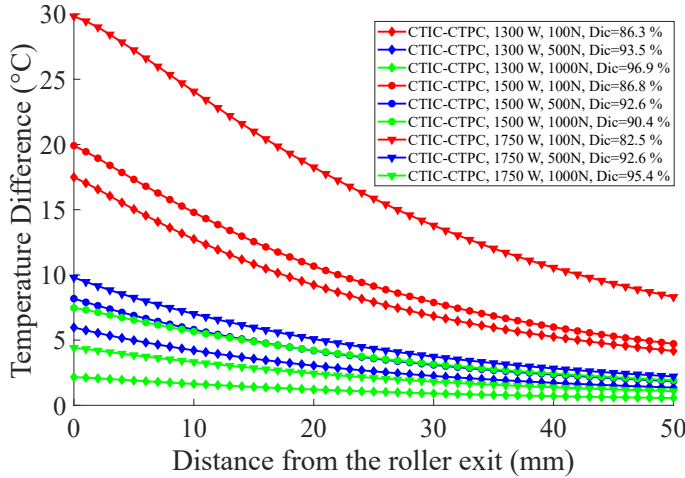


Figure 6.16. The difference between the computed temperature histories using the TCR from Equation (6.1) (CTIC) and a very small TCR (CTPC).

TCR has an influence on the temperature history during the compaction and cooling phases; however, the experimental temperatures from the cooling phase were predicted with a limited accuracy when TCR was calculated with Equation (6.1) using a *constant* degree of intimate contact. The numerical results initially overshoot and later underestimated the experimental results as demonstrated in Figure 6.11. Such a trend suggests that TCR was not constant during the cooling phase. This behavior can be linked to void expansion after the compaction pressure was released. So far, this mechanism has been considered only for intra-laminar voids in the literature [48]. However, Figure 6.12 shows that the final void content of the laminates manufactured in this study was present mostly between the topmost layer and the substrate. Based on this information, TCR evolution during the cooling phase of LAFP can be described as follows. The degree of intimate contact reached its maximum at the roller exit, causing the experimental heat flux between the tape and the substrate to be more than the calculations. Increasing heat flux caused the experimental tape temperature to be lower than the calculated temperature initially because the tape was warmer than the substrate in the experiments (shown

in Figure 6.10). As soon as the compaction pressure was released, the inter-laminar voids expanded and the degree of intimate contact decreased until the equilibrium between the pressure within the voids and the atmospheric pressure was reached. During the expansion of voids, the heat flux between the tape and substrate decreased and the cooling rate of the experimental temperature became lower than the calculated temperature. As a result, calculated temperatures underestimated the experimental temperatures further away from the roller exit. Additionally, in the experiments, TCR evolves during the compaction phase. It can be expected that at the nip point, the experimental TCR was higher than the numerical one, as the degree of intimate contact was low. This would result in a larger difference between the temperatures of the tape and substrate. However, as hypothesized above, the maximum degree of intimate contact was probably reached during the compaction phase. Therefore, in the experiments, the heat transfer between the tape and substrate was larger than the one calculated with the model for some duration under the compaction roller. This duration is material-specific, as the evolution of TCR is highly dependent on the surface morphology and the resin rheology [16]. Considering these phenomena, the evolution of the degree of intimate contact in the compaction and cooling phases of the process should be investigated further for a more accurate analysis of the process.

Another possible improvement to the temperature calculations is the consideration of the evolving contact between the compaction roller and the top surface of the tape. As the compaction force was increased, the contact conductance between the roller and the tape might have increased due to increasing degree of intimate contact. In this research, the effect of compaction force was implemented as a change in the contact length but the convection coefficient between the roller and the top surface of the tape was kept constant. Further research on the evolution of the thermal contact between the tape and the roller is recommended.

6.5.3 Origins of TCR development during LAFP

The measured degrees of intimate contact presented in Figure 6.13 lead to additional interesting observations on intimate contact development, which is the source of TCR, during LAFP. Firstly, the samples manufactured with a laser power of 1300 W, which results in a tape inlet temperature ($\sim 325^\circ\text{C}$ as shown in Figure 6.10) lower than the melting temperature T_m (343°C), had the same level of degree of intimate contact as the ones manufactured with higher laser powers. This result is counter-intuitive as the semi-crystalline structure of PEEK has been considered not to allow significant softening of the polymer below T_m . In the past, several semi-crystalline polymers such as high density polyethylene (PE), polypropylene (PP), polyoxymethylene (POM), and poly(vinylidene fluoride) (PVF) were shown to be malleable between the reversible crystallization temperature T_c and T_m [49]. At T_c , crystal subunits are capable of moving within larger crystal units [50]. Between T_c and T_m , the mechanism for deformation was proposed to be lamellar slip and extended chain crystal formation [51]. Such a mechanism can explain intimate contact development below T_m for high performance thermoplastic composites. Recently, it was shown that CF/PEEK laminates can be thermoformed between 165 – 325°C [52] and intimate contact can develop below T_m for CF/PEKK laminates during

out-of-autoclave consolidation with low pressure [53]. The results in Figure 6.13 confirm this point of view and show that polymer flow can take place between the T_g and T_m . Intimate contact development below T_m should be further investigated considering the reversible crystalline transition phenomenon.

Another noteworthy result is that the laser power and hence the tape inlet temperature did not have a statistically significant influence on the final degree of intimate contact, even above the melting temperature. A similar behavior was also observed for CF/PEKK tapes placed on an aluminum tool in a previous study [10]. This is unexpected since the polymer viscosity drops with increasing temperature. A possible explanation is that the interaction between the fibers in the polymer melt plays a more dominant role for intimate contact development under LAFP specific conditions such as heating without pressure, very short compaction duration and rapid cooling. It has already been shown that during the intimate contact development process, dry fibers need to be compacted [10] and this process is not primarily affected by resin viscosity. Moreover, it has been reported that the friction between the fibers has a significant part in the overall viscosity of the CF/PEEK melt and because of that an increase in temperature up to 20 °C would have little effect [54]. This study showed that intimate contact development might be insensitive to even higher temperature differences during LAFP, as the difference between the inlet temperatures was as high as 140 °C (Figure 6.10).

6

6.5.4 Potential use of TCR for process inspection

In addition to understanding the influence of TCR and the mechanisms behind it for a more realistic description of the temperature history, one can exploit the phenomenon for in-situ inspection of intimate contact development. With a reverse approach, the degree of intimate contact can be predicted from the measurements of the cooling behavior of the newly placed tape. This can be achieved with the optical-thermal model presented in Section 6.3 for flat laminates, provided that an offline database of cooling behavior is created at given LAFP process parameters for varying degrees of intimate contact (and the resulting TCR). During placement, the in-situ collected data can be compared to the previously computed cooling data. The degree of intimate contact which yields the least difference between the in-situ and computed data can be used as an indication of the bonding quality.

6.6 Conclusion

This study demonstrates the effect of the thermal contact resistance between the tape and substrate on the temperature history during the cooling phase of LAFP through dedicated experiments and numerical calculations. A novel experimental methodology was designed to understand the effect with a non-contact temperature measurement method, as contact temperature measurement methods directly influence the degree of intimate contact in their surroundings. A three-dimensional combined optical-thermal model including the thermal contact resistance between the tape and substrate was developed to assess the accuracy of the commonly preferred assumption of a perfect thermal contact in thermal analysis of the LAFP process.

Experimental results indicated that, for the same tape inlet temperature, a change in the compaction force resulted in a different temperature at the roller exit, which is in correlation with the final degree of intimate contact. As the degree of intimate contact increased, the heat transfer from the tape to substrate increased. Therefore, the tape was colder during the cooling phase. It was also observed that intimate contact can develop at temperatures below the melting temperature of the polymer.

Numerical results confirmed that neglecting thermal contact resistance at the interface causes significant underestimation of the temperature history, especially for specimens with a degree of intimate contact below 90 %. Moreover, comparison between the calculated and measured temperature history led to a new hypothesis on intimate contact development during the cooling phase of LAFP. It was suggested that the expansion of voids after the pressure application should be considered not only for intra-laminar voids as is commonly done in the literature but also for the inter-laminar voids.

Further research is recommended on the evolution of intimate contact (inter-laminar void expansion) during the cooling phase of LAFP. Implementation of the corresponding TCR evolution to thermal models is another path for future studies. Finally, intimate contact development below the melting temperature should be investigated for a more accurate analysis of the LAFP process.

References

- [1] Airbus, . Press Release. 2020.
- [2] Airbus, . Global Market Forecast: Cities, Airports & Aircraft 2019-2038. 2019.
- [3] Lukaszewicz, D.H., Ward, C., Potter, K.D.. The engineering aspects of automated prepreg layup: History, present and future. *Composites Part B: Engineering* 2012;43(3):997–1009.
- [4] Kozaczuk, K.. Automated Fiber Placement Systems Overview. *Transactions of the Institute of Aviation* 2016;245(4):52–59.
- [5] Grouve, W.J.B., Warnet, L.L., Rietman, B., Visser, H.A., Akkerman, R.. Optimization of the tape placement process parameters for carbon-PPS composites. *Composites Part A: Applied Science and Manufacturing* 2013;50:44–53.
- [6] Maurer, D., Mitschang, P.. Laser-powered tape placement process – simulation and optimization. *Advanced Manufacturing: Polymer & Composites Science* 2015;1(3):129–137.
- [7] Stokes-Griffin, C.M., Compston, P.. The effect of processing temperature and placement rate on the short beam strength of carbon fibre-PEEK manufactured using a laser tape placement process. *Composites Part A: Applied Science and Manufacturing* 2015;78:274–283.
- [8] Schaefer, P.M., Gierszewski, D., Kollmannsberger, A., Zaremba, S., Drechsler, K.. Analysis and improved process response prediction of laser- assisted automated tape placement with PA-6/carbon tapes using Design of Experiments and

- numerical simulations. *Composites Part A: Applied Science and Manufacturing* 2017;96:137–146.
- [9] Weiler, T., Emonts, M., Wollenburg, L., Janssen, H.. Transient thermal analysis of laser-assisted thermoplastic tape placement at high process speeds by use of analytical solutions. *Journal of Thermoplastic Composite Materials* 2018;31(3):311–338.
 - [10] Çelik, O., Peeters, D., Dransfeld, C., Teuwen, J.. Intimate contact development during laser assisted fiber placement: Microstructure and effect of process parameters. *Composites Part A: Applied Science and Manufacturing* 2020;134.
 - [11] Levy, A., Tierney, J., Heider, D., Gillespie, J.W., Lefebure, P., Lang, D.. Modeling of inter-layer thermal contact resistance during thermoplastic tape placement. *Tech. Rep.*; 2012.
 - [12] Hörmann, P., Stelzl, D., Lichtinger, R., Van Nieuwenhove, S., Mazón Carro, G., Drechsler, K.. On the numerical prediction of radiative heat transfer for thermoset automated fiber placement. *Composites Part A: Applied Science and Manufacturing* 2014;67:282–288.
 - [13] Stokes-Griffin, C.M., Compston, P. A combined optical-thermal model for near-infrared laser heating of thermoplastic composites in an automated tape placement process. *Composites Part A: Applied Science and Manufacturing* 2015;75:104–115.
 - [14] Barasinski, A., Leygue, A., Soccarr, E., Poitou, A.. Identification of non uniform thermal contact resistance in automated tape placement process. *International Journal of Material Forming* 2014;7(4):479–486.
 - [15] Levy, A., Heider, D., Tierney, J., Gillespie, J.W.. Inter-layer thermal contact resistance evolution with the degree of intimate contact in the processing of thermoplastic composite laminates. *Journal of Composite Materials* 2014;48(4):491–503.
 - [16] Leon, A., Barasinski, A., Chinesta, F. Microstructural analysis of pre-impregnated tapes consolidation. *International Journal of Material Forming* 2017;10(3):369–378.
 - [17] Yang, E., Pitchumani, R.. A fractal Cantor set based description of interlaminar contact evolution during thermoplastic composites processing. *Journal of Materials Science* 2001;36(19):4661–4671.
 - [18] Chinesta, F., Leygue, A., Bogner, B., Ghatias, C., Poulhaon, F., Bordeu, F., et al. First Steps Towards an Advanced Simulation of Composites Manufacturing by Automated Tape Placement. *International Journal of Material Forming* 2014;7(1):81–92.
 - [19] Lichtinger, R., Hörmann, P., Stelzl, D., Hinterhölzl, R.. The effects of heat input on adjacent paths during Automated Fibre Placement. *Composites Part A: Applied Science and Manufacturing* 2015;68:387–397.

- [20] Kollmannsberger, A., Lichtinger, R., Hohenester, F., Ebel, C., Drechsler, K.. Numerical analysis of the temperature profile during the laser-assisted automated fiber placement of CFRP tapes with thermoplastic matrix. *Journal of Thermoplastic Composite Materials* 2018;31(12):1563–1586.
- [21] Denkena, B., Schmidt, C., Völtzer, K., Hocke, T.. Thermographic online monitoring system for Automated Fiber Placement processes. *Composites Part B: Engineering* 2016;97:239–243.
- [22] Juarez, P.D., Gregory, E.D.. In situ thermal inspection of automated fiber placement manufacturing. *AIP Conference Proceedings* 2019;2102:120002.
- [23] Di Francesco, M., Valverde, M.A., Ward, C., Giddings, P.F., Dell' Anno, G., Potter, K.. Influence of Layup Speed on the Quality of Thermoplastic Preforms Manufactured By Laser- Assisted Automated Fibre Placement. *ECCM17 - 17th European Conference on Composite Materials* 2016;(June):26–30.
- [24] Composites, T.A.. TenCate Cetex® TC1200 PEEK Resin System Product Data Sheet 2017;.
- [25] Otsu, N.. A Threshold Selection Method from Gray-Level Histograms. *IEEE Transactions on Systems, Man and Cybernetics* 1979;9(1):62–66.
- [26] The MathWorks Inc, . MATLAB and Statistics Toolbox Release 2017b. 2017.
- [27] Kok, T.. On the consolidation quality in laser assisted fiber placement: the role of the heating phase. Phd thesis; University of Twente; 2018.
- [28] Hosseini, S.M.A., Baran, I., van Drongelen, M., Akkerman, R.. On the temperature evolution during continuous laser-assisted tape winding of multiple C/PEEK layers: The effect of roller deformation. *International Journal of Material Forming* 2020;;1–19.
- [29] Lee, W.I., Springer, G.S.. A Model of the Manufacturing Process of Thermoplastic Matrix Composites. *Journal of Composite Materials* 1987;21(11):1017–1055.
- [30] Tierney, J., Gillespie, J.W.. Modeling of In Situ Strength Development for the Thermoplastic Composite Tow Placement Process. *Journal of Composite Materials* 2006;40(16):1487–1506.
- [31] Ghasemi Nejhad, M.N., Cope, R., Güceri, S.I.. Thermal Analysis of in-situ Thermoplastic Composite Tape Laying. *Journal of Thermoplastic Composite Materials* 1991;4(1):20–45.
- [32] Ageorges, C., Ye, L., Mai, Y.W., Hou, M.. Characteristics of resistance welding of lap shear coupons. Part I: Heat transfer. *Composites Part A: Applied Science and Manufacturing* 1998;29(8):899–909.
- [33] Çelik, O., Shroff, S., Teuwen, J.J.E., Bergsma, O.K., Benedictus, R.. A 3-D Finite Element Model for Thermal Analysis of Laser Assisted Fiber Placement. In: *SAMPE Europe*. Southampton; 2018,.

- [34] Reichardt, J., Baran, I., Akkerman, R.. New analytical and numerical optical model for the laser assisted tape winding process. *Composites Part A: Applied Science and Manufacturing* 2018;107:647–656.
- [35] Cogswell, F.N.. *Thermoplastic aromatic polymer composites: a study of the structure, processing, and properties of carbon fibre reinforced polyetheretherketone and related materials*. Butterworth-Heinemann; 1992.
- [36] Kim, H.J., Kim, S.K., Lee, W.I.. A study on heat transfer during thermoplastic composite tape lay-up process. *Experimental Thermal and Fluid Science* 1996;13(4):408–418.
- [37] Dassault Systèmes, . *ABAQUS 2017 Documentation*. 2017.
- [38] Zaami, A., Schäkel, M., Baran, I., Bor, T.C., Janssen, H., Akkerman, R.. Temperature variation during continuous laser-assisted adjacent hoop winding of type-IV pressure vessels: An experimental analysis. *Journal of Composite Materials* 2019;.
- [39] Stokes-Griffin, C.M., Kollmannsberger, A., Compston, P., Drechsler, K.. The effect of processing temperature on wedge peel strength of CF/PA 6 laminates manufactured in a laser tape placement process. *Composites Part A: Applied Science and Manufacturing* 2019;121:84–91.
- [40] Tardif, X., Pignon, B., Boyard, N., Schmelzer, J.W., Sobotka, V., Delaunay, D., et al. Experimental study of crystallization of PolyEtherEtherKetone (PEEK) over a large temperature range using a nano-calorimeter. *Polymer Testing* 2014;36:10–19.
- [41] Stokes-Griffin, C.M., Compston, P. Investigation of sub-melt temperature bonding of carbon-fibre/PEEK in an automated laser tape placement process. *Composites Part A: Applied Science and Manufacturing* 2016;84:17–25.
- [42] Di Francesco, M., Giddings, P.F., Scott, M., Goodman, E., Dell’Anno, G., Potter, K.. Influence of laser power density on the meso-structure of thermoplastic composite preforms manufactured by Automated Fibre Placement. In: *SAMPE Long Beach 2016*; vol. 53. ISBN 9788578110796; 2016, p. 1689–1699. arXiv:arXiv:1011.1669v3.
- [43] Rodriguez-Lence, F., Martin, M.I., Fernandez Horcajo, K.. In-situ consolidation of integrated thermoplastic fuselage panels: The future in structural comercial aerocomposites. In: *ECCM 2018 - 18th European Conference on Composite Materials*. ISBN 9781510896932; 2018,.
- [44] Oliveri, V., Zucco, G., Peeters, D., Clancy, G., Telford, R., Rouhi, M., et al. Design, manufacture and test of an in-situ consolidated thermoplastic variable-stiffness wingbox. *AIAA Journal* 2019;57(4):1671–1683.
- [45] Hosseini, S.M.A., Schäkel, M., Baran, I., Janssen, H., van Drongelen, M., Akkerman, R.. A new global kinematic-optical-thermal process model for laser-assisted tape winding with an application to helical-wound pressure vessel. *Materials & Design* 2020;193:108854.

- [46] Lichtinger, R., Lacalle, J., Hinterhölzl, R., Beier, U., Drechsler, K.. Simulation and experimental validation of gaps and bridging in the automated fiber placement process. *Science and Engineering of Composite Materials* 2015;22(2):131–148.
- [47] Peeters, D., Clancy, G., Oliveri, V., O'Higgins, R., Jones, D., Weaver, P.M.. Concurrent design and manufacture of a thermoplastic composite stiffener. *Composite Structures* 2019;212:271–280.
- [48] Pitchumani, R., Ranganathan, S., Don, R.C., Gillespie, J.W., Lamontia, M.A.. Analysis of Transport Phenomena Governing Interfacial Bonding and Void Dynamics During Thermoplastic Tow-placement. *International Journal of Heat and Mass Transfer* 1996;39(9):1883–1897.
- [49] Aharoni, S.M., Sibilía, J.P. Crystalline transitions and the solid-state extrusion of polymers. *Journal of Applied Polymer Science* 1979;23(1):133–140.
- [50] Aharoni, S.M., Sibilía, J.P. Extrudability of Crystalline Polymers. *Polymer Engineering and Science* 1979;19(6):450–455.
- [51] Bigg, D.M.. Mechanical property enhancement of semicrystalline polymers—A review. *Polymer Engineering & Science* 1988;28(13):830–841.
- [52] Zheng, B., Gao, X., Li, M., Deng, T., Huang, Z., Zhou, H., et al. Formability and failure mechanisms of woven CF/PEEK composite sheet in solid-state thermoforming. *Polymers* 2019;11(6).
- [53] Saffar, F., Sonnenfeld, C., Beauchêne, P., Park, C.H.. In-situ Monitoring of the Out-Of-Autoclave Consolidation of Carbon / Poly-Ether-Ketone-Ketone Prepreg Laminate. *Frontiers in Materials* 2020;7(June):1–12.
- [54] Deignan, A., Stanley, W.F., McCarthy, M.A.. Insights into wide variations in carbon fibre/polyetheretherketone rheology data under automated tape placement processing conditions. *Journal of Composite Materials* 2017;.

Chapter 7

Concluding Remarks and Future Outlook

This chapter highlights the main novelties and insights generated in the previous chapters of this work. Future outlook is also provided to shed light onto possible research paths in the future.

7.1 Summary and Conclusions

This thesis aims to improve the understanding on the consolidation process during laser-assisted fiber placement (LAFP) with in-situ consolidation. This manufacturing method differs from conventional composite manufacturing methods such as autoclave processing or press molding in a number of ways such as localized rapid laser heating without pressure application, very short compaction times and cooling at ambient pressure. Due to these differences, compaction during LAFP cannot be completely described by existing theories, which were developed for conventional manufacturing techniques such as press molding. The following research questions were proposed to cover the consolidation process in all three phases of LAFP (heating, compaction and cooling):

- How do the laser heater parameters such as heated length and heating time affect the structure of the thermoplastic tapes during rapid laser heating?
- How does intimate contact develop under LAFP-specific thermal and mechanical conditions?
- What is the effect of laser-induced deconsolidation on the compaction process of the thermoplastic tapes?
- How does consolidation quality affect the temperature history during the cooling phase of LAFP?

In Chapters 3 to 6, experiments and numerical methods were used to answer each research question. Based on the results, the following conclusions were derived for each phase of the process.

In the heating phase:

- Rapid laser heating without pressure application causes significant changes on the micro- and meso-structure of the tape. These changes are in the form of increased waviness, surface roughness, thickness and void content. Currently, process models for LAFP do not consider these effects. They should be considered for a more accurate description of the heat transfer and consolidation mechanisms during the process.
- Heated length is a significant factor for waviness formation, arc-length width and surface roughness. Therefore, its effects should be considered for heating strategies where the heated length is adjusted to optimize the heat soak in the tape. Laser-induced deconsolidation might limit the effectiveness of such a strategy at large heated lengths.
- During laser heating, the shape of the tape surface and the temperature distribution show resemblance to each other. This is thought to be initiated by the reduced distance between the laser source and the decompacted fibers at the surface above the glass transition temperature and exacerbated as a result of the differing incidence angle between the laser beams and the tape surface at the peaks and valleys of the surface profile. This interesting relationship can open up possibilities for

novel in-situ inspection concepts such as determining the shape of the incoming tape during the heating phase using the infra-red cameras already built-in most of the LAFP systems. By using such a concept, one can potentially determine the waviness of the tape prior to nip point without a separate sensor.

In the compaction phase:

- As demonstrated in Chapter 4, complete mechanical contact of the tape and substrate at the micro-scale might not contribute to elimination of inter-laminar voids or bond strength development due to the presence of dry fibers at the tape surface prior to compaction. Only the regions with resin content at the interface should be accepted as a measure of intimate contact at the interface. In order to quantify the amount of flattened resin content at the surface at the micro-scale, the concept of *effective intimate contact* was proposed and a methodology to obtain the degree of effective intimate contact from surface micrographs was presented.
- Effective intimate contact develops with squeeze flow at the resin- rich portions of the surface; however, through-thickness and in-plane percolation flow is required to impregnate the regions with compressed dry fibers. Due to the percolation flow mechanism playing a role, the through-thickness temperature distribution of the tape should be considered for effective intimate contact development during the LAFP process.
- Despite the requirement of resin flow towards the tape-substrate interface at resin-poor locations, in Chapter 6, it was observed that intimate contact can develop significantly between the tape and substrate below the melting temperature of the polymer. Such a result indicated that in addition to effective intimate contact development, mechanisms which play a role below the melting temperature of the resin should be considered for intimate contact development during LAFP.
- In Chapter 5, it was shown that waviness induced by laser-deconsolidation vanishes when the material is heated above the glass transition temperature even at a very low compaction pressure. This shows that the tape is malleable at the meso-scale even if the resin is not in a molten state.
- Unlike waviness; increased thickness, void content and surface roughness due to laser-deconsolidation were not eliminated between the glass transition and melting temperatures. Also, effective intimate contact did not develop for samples which were subjected to a maximum temperature of 200 °C (above the glass transition temperature). Considering that only meso-scale features were significantly reduced and effective intimate contact is not established at the micro-scale between the glass transition and melting temperatures, it is thought that intimate contact development can be explained as a combination of both meso- and micro-scale mechanisms in general.
- The amount of applied pressure plays a significant role for reducing the effects of deconsolidation for the final structure of the compacted tapes. The thickness at the glass transition temperature and the final surface roughness increased, and

degree of effective intimate contact decreased as a result of increasing degree of laser-deconsolidation when a compaction pressure less than 300 kPa was applied. This amount of pressure is easily reachable on flat molds with current LAFP equipment; however, on curved molds, pressure might drop between the contact points of concave surfaces or at the corners due to the compaction roller not conforming with the complete tow. The effects of laser-deconsolidation should be especially considered for such applications.

In the cooling phase:

- Compaction force affects not only ply adhesion or mechanical defects but also the temperature history during LAFP. For the same inlet temperature of the tape, an increasing compaction force results in a higher degree of intimate contact and lower temperature at the roller exit. This is an important consideration as the tape may not cool down sufficiently at low compaction pressures.
- Inter-layer thermal contact resistance has a significant influence for the calculation of temperature. When it was not included in a thermal simulation, the calculated temperature at the top surface of the newly placed tape underestimated the experimental measurements.
- Using a constant thermal contact resistance was not sufficient to exactly match the experimental temperature with the thermal model. It is thought that the evolution of intimate contact during the compaction and cooling phases of the LAFP process influences the instantaneous thermal contact resistance.

7

7.2 Recommendations for future research

Following the investigations in this thesis, several research paths can be recommended for future studies:

- The effect of tape tension on laser-induced deconsolidation should be investigated. For that purpose, the heating experiments in Chapter 3 can be performed under different controlled tape tension values. Such a research might reveal the role of the tape tension in controlling the effects of deconsolidation during the LAFP process. Currently, LAFP systems work on low tape tension [1, 2]; however, research in this area might lead to optimization of tape tension to minimize deconsolidation under specified heating parameters.
- Modelling the effects of laser-induced deconsolidation such as fiber decomposition, void growth and waviness formation on a constitutive level and implementation to process models is recommended. It is expected that these effects would have consequences for heat transfer, tape deformation, void compaction and bonding models and increase their accuracy for the LAFP process.
- A multi-scale model which considers both the meso-scale tape flattening between the glass transition and melting temperature and micro-scale effective intimate

contact development involving the combination of squeeze flow and percolation flow is recommended. Currently, intimate contact development below the melting temperature and at locations with dry fibers cannot be explained with the existing theories.

- The effect of compaction force on intimate contact development and temperature history should be investigated for curved surfaces. These surfaces are becoming a focal point for research as demonstrated by recent publications [3–5]. These publications mostly investigated the laser–composite interaction and the temperature profile on curved surfaces; however, the pressure might also vary under the compaction roller. The pressure profile under the compaction roller would be an input to the multi-scale intimate contact model suggested above and would affect the temperature profile indirectly via inter-laminar thermal contact resistance.
- Further research should focus on capturing the evolution of intimate contact (and the accompanying thermal contact resistance) during the cooling phase of LAFP experimentally. The phenomenon was hypothesized based on thermal simulations but experimental confirmation is still required. It is expected that the phenomenon is significant for tapes which do not cool down below the glass transition temperature at the roller exit.
- As an alternative to physics-based modeling, phenomenological models can be developed for intimate contact development to observe the effects of different degrees of laser-deconsolidation of the same material or different material systems. Such models can be generated by performing experiments similar to the compaction experiments presented in Chapter 5 at relevant temperature, pressure and time intervals to any given manufacturing process. Phenomenological equations can be fit to the experimental results and the fitting parameters can be used for comparison.

References

- [1] Lukaszewicz, D.H., Ward, C., Potter, K.D.. The engineering aspects of automated prepreg layup: History, present and future. *Composites Part B: Engineering* 2012;43(3):997–1009.
- [2] Frketic, J., Dickens, T., Ramakrishnan, S.. Automated manufacturing and processing of fiber-reinforced polymer (FRP) composites: An additive review of contemporary and modern techniques for advanced materials manufacturing. *Additive Manufacturing* 2017;14:69–86.
- [3] Kollmannsberger, A.. Heating characteristics of fixed focus laser assisted Thermoplastic-Automated Fiber Placement of 2D and 3D parts. Ph.D. thesis; Technical University of Munich; 2019.
- [4] Hosseini, S.M.A.. TOWARDS AN ACCURATE PROCESS DESIGN TOOL FOR LASER-ASSISTED TAPE WINDING. Phd thesis; University of Twente; 2021.

- [5] Zaami, A.. Development of Fast Local Analysis Tool for Optimized Laser Assisted Tape Winding. Ph.D. thesis; University of Twente; Enschede, The Netherlands; 2021.

Acknowledgments

What a journey it has been! The last four and a half years were full of ups and downs and would be very difficult to go through without the people around me. Their help, support, encouragement and love kept me going and should be properly acknowledged.

To begin with, Julie, thank you for offering your supervision in the second year of my PhD project. Your constant help, support and guidance brought me the energy to continue doing research. Our discussions taught me a lot about critical thinking and expressing my ideas in a structured way. You were always there when I had problems and thought along with me to find solutions. Also, the jokes during the meetings and at the lunch table were the icing on the cake. I feel grateful for having had the chance to work with you.

Then comes Clemens, who became my promotor almost halfway through my PhD. Your caring attitude, inspiring ideas and constructive feedback really helped me to write this thesis. Moreover, your sense of humor made the process pretty enjoyable. Thank you for believing in me and supporting my project.

Daniël, when we first met in the Fellowship in February 2018, I could never guess that we would work together. I am glad that you joined our faculty several months later and shared your expertise on LAFP with me. From the moment you became my second supervisor, you were always deeply involved in my project. I greatly appreciate your help in setting up the laser experiments and the valuable feedback you provided on every aspect of my research. Your company during the lunches and other occasions (including a trip to Canada) was also really fun.

Rinze, I would like to thank you for giving me the initial opportunity to pursue a PhD degree in the department of Aerospace Structures and Materials.

I am a lucky person for having worked with not one, not two, but three wonderful management assistants at different stages of my PhD. I would like to thank Marianne, Gemma and Laura from the depths of my heart. These ladies made my life much easier by handling the paperwork and providing support whenever needed.

I would also like to thank the former and current staff members and technicians of the ASM lab for their support. Among them, I had the chance to work with Durga, Ed, Frans, Gertjan, Johan, Kees, Marlies, Misja, Rob and Victor. Your help is much appreciated. Special thanks go to Berthil, whose help was crucial for setting up the laser equipment and performing experiments with it.

I spent five months in University of Twente and TPRC as a visiting researcher. For creating that opportunity and making the necessary arrangements, I am grateful to İsmet,

Remko, Wouter, Sebastiaan and Martina. I especially thank Amin H. for his assistance with the LAFP machine and optical model. Our fruitful collaboration resulted in a conference paper and a journal article.

Special thanks to Chris and Michiel from Royal NLR for their great help in planning and conducting fiber placement experiments.

I am grateful to the colleagues from the AMT, SI&C and ASCM departments for making the working environment an interesting and enjoyable one: Agnes, Bram, Calvin, Camila, Chirag, Chizoba, Darwin, Davide, Deniz, Edgars, Fardin, Giacomo, Hongwei, Ines, Irene, Javi, Jesse, John-Alan, Jos, Julian, Julien, Jurij, Kunal, Leila, Lucas, Marta, Megan, Mohamed, Nan, Nick, Niels R., Niels v. H., Nikos, Nitesh, Paul, Pedro, Pratik, Roger, Romina, Sergio, Shichen, Silvia, Sofia, Tutu, Ujala, Wandong, Xi, Yannis and Yuzhe. Abhas and Tom, thank you for your hard work during your Master's projects. It was a pleasure to supervise you and discuss different approaches to the problems you faced.

Nakash, broer, I really enjoyed the dinners we had together (even though we could not find a proper Turkish restaurant) and the talks we made about all kinds of stuff. Nicolas, it was always nice to see you in the office (which did not usually happen in the mornings). Good luck with your alternative career in streaming! Luigi, my Italian friend, you brought a lot of cheer with yourself. Never forget "one minute" and Turkish Pavarotti. Chantal, Lubin and Eirini, thank you for being such nice office mates.

Also, thanks to Amin Z., Bharath, Iqbal, Jagadeesh, Jamal, Logen, Nick, Onur, Vanessa, Waqas and Yash for the nice conversations we had during my time at University of Twente.

Ercan and Özge, thank you for being my second family and providing endless support and love during the long years we have known each other for. Your door has always been open to me and I enjoyed walking through it every time. Ozi, it was great that our paths met again in the Netherlands after the years in the university. I appreciate having you as a close friend, colleague and neighbor. Merve, our friendship is beyond the borders. Thank you and Burak for hosting me in Canada and our fun trip. Meltem, you left us too soon, I will miss and remember you forever. Ranko, it was such a pleasure to hit all the high notes in the bass score shoulder to shoulder, thank you for being an amazing friend. Hazan and Emre, I appreciate your sincerity and friendliness. Pelin, our encounter in Enschede after all those years was a big surprise to me. I hope that we have many more trips with you and Yiğitcan. Sila and Erkan, thank you for your nice friendship. My "Samimi" friends, I wish we could see each other more often, thank you for all the love and joy we shared during our online/offline gatherings.

I would like to thank my parents, Nilgün and Ahmet, and my parents-in-law, Sadiye and Kadir, for their constant love, encouragement and faith in me. My sister-in-law, Gizem, and Oğuz, it is a privilege to have a part of my family nearby. I am grateful for your love, support and all the fun we had together. Başta annem ve babam olmak üzere bütün ailem, bana olan sonsuz sevginiz ve desteğiniz için sizlere minnettarım.

Finally, I would like to express my gratitude to Senem, my dear wife and partner in everything. Thank you million times for your unconditional support and love through thick and thin. You did everything for me during all the difficult times, and you did it while dealing with your own PhD! With you by my side, this journey has been much

more meaningful and beautiful. This thesis might mark the end of a chapter in my life but many more await to be written in our story, and I can't wait to see them. I love you.

Curriculum Vitæ

Ozan ÇELİK

The author was born on 29 May 1991 in Ankara, the capital city of Turkey. He went to a local primary school and Atatürk Anatolian High School. In September 2008, he started his Bachelor's studies in the Mechanical Engineering department at Middle East Technical University. In September 2012, he spent a semester in Prague, Czechia during his Erasmus exchange in Czech Technical University. After obtaining his BSc. degree in June 2013 and a nice holiday with family and friends, he started working in Turkish Aerospace Industries (TAI) in September 2013. He worked as a design engineer in the first indigeneous helicopter project of Turkey (GÖKBİY) and performed the structural analysis of the rotor blades under static and fatigue loads. Within the same month, he started his MSc. studies in the department of Mechanical Engineering at Middle East Technical University. He completed his Master's thesis on the tensile behavior of tapered composite laminates in September 2016.

In January 2017, he moved to Delft to pursue a PhD degree in the Aerospace Structures and Materials Department at Delft University of Technology on the topic of consolidation mechanisms during laser assisted fiber placement. Between November 2019 and April 2020, he worked as a visiting researcher in the Chair of Production Technology at University of Twente.

Although his PhD comes to an end, he is still interested in working on automated manufacturing solutions for composite structures and improving them using artificial intelligence concepts.

List of Publications

Journal Articles

1. **Çelik, O.**, Peeters, D., Dransfeld, C., Teuwen, J., Intimate contact development during laser-assisted fiber placement: Microstructure and effect of process parameters. *Composites Part A: Applied Science and Manufacturing*, 105888, Volume 134, 2020.
2. **Çelik, O.**, Hosseini, S.M.A., Baran, I., Grouve, W.J.B., Akkerman, R., Peeters, D.M.J., Teuwen, J.J.E., Dransfeld, C.A., The influence of inter-laminar thermal contact resistance on the cooling of material during laser assisted fiber placement. *Composites Part A: Applied Science and Manufacturing*, 106367, Volume 145, 2021.
3. **Çelik, O.**, Choudhary, A., Peeters, D., Teuwen, J., Dransfeld, C., Deconsolidation of thermoplastic prepreg tapes during rapid laser heating. *Composites Part A: Applied Science and Manufacturing*, 106575, Volume 149, 2021.
4. **Çelik, O.**, Bussink, T., Peeters, D., Teuwen, J., Dransfeld, C., The effect of laser-induced deconsolidation on the compaction behavior of thermoplastic composite tapes. *Composites Part A: Applied Science and Manufacturing*, 106670, Volume 151, 2021.

Conference Proceedings

1. **Çelik, O.**, Shroff, S., Teuwen, J.J.E., Bergsma O.K., Benedictus, R., A 3-D finite element model for thermal analysis of laser assisted fiber placement. In *Proceedings of SAMPE Europe Conference*, Southampton (United Kingdom), 2018.
2. **Çelik, O.**, Teuwen, J.J.E., Effects of process parameters on intimate contact development in laser assisted fiber placement. In S.V. Hoa (Ed.), *Proceedings of 4th Automated Composites Manufacturing (ACM4)*, Montreal (Canada), 2019.
3. **Çelik, O.**, Hosseini, S.M.A., Baran, I., Grouve, W.J.B., Akkerman, R., Peeters, D.M.J., Teuwen, J.J.E., Dransfeld, C.A., The influence of thermal contact resistance on the thermal history in laser assisted fiber placement. In *Proceedings of SAMPE Europe Conference*, Amsterdam (The Netherlands), 2020.